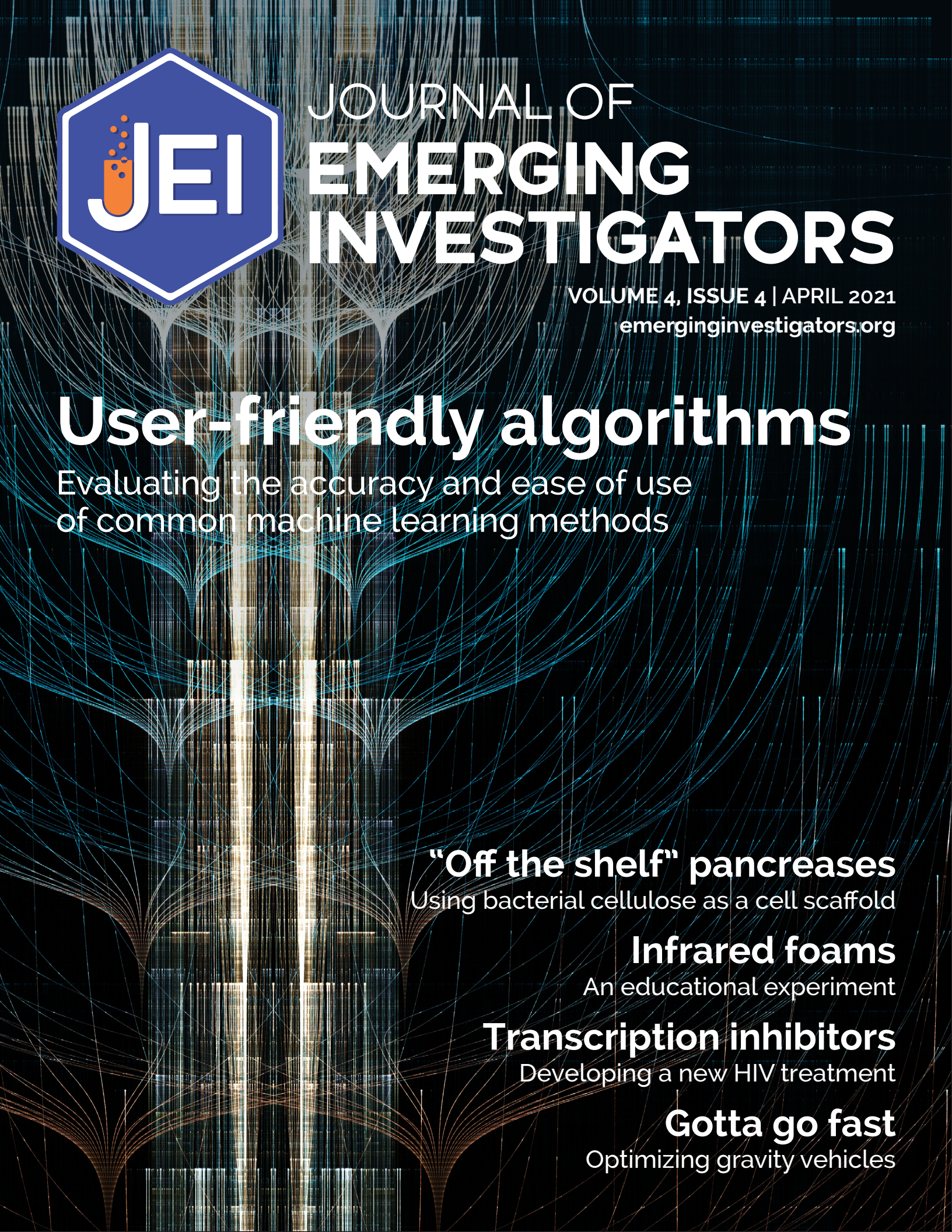

JOURNAL OF
EMERGING INVESTIGATORS

VOLUME 4, ISSUE 4 | APRIL 2021
emerginginvestigators.org

User-friendly algorithms
Evaluating the accuracy and ease of use of common machine learning methods

"Off the shelf" pancreases
Using bacterial cellulose as a cell scaffold

Infrared foams
An educational experiment

Transcription inhibitors
Developing a new HIV treatment

Gotta go fast
Optimizing gravity vehicles

JOURNAL OF EMERGING INVESTIGATORS

The Journal of Emerging Investigators is an open-access journal that publishes original research in the biological and physical sciences that is written by middle and high school students. JEI provides students, under the guidance of a teacher or advisor, the opportunity to submit and gain feedback on original research and to publish their findings in a peer-reviewed scientific journal. Because grade-school students often lack access to formal research institutions, we expect that the work submitted by students may come from classroom-based projects, science fair projects, or other forms of mentor-supervised research.

JEI is a non-profit group run and operated by graduate students, postdoctoral fellows, and professors across the United States.

Contents

VOLUME 4, ISSUE 4 | APRIL 2021

Jeslyn Wu, Charissa Luk, Catherine Zhou, Aashi Shah, Aishwarya Yuvaraj, and Edward Njoo
Mission San Jose High School, Fremont, CA
Bishop O'Dowd High School, Oakland, CA
Lynbrook High School, San Jose, CA
Amador Valley High School, Pleasanton, CA
American High School, Fremont, CA,

JOURNAL OF
EMERGING INVESTIGATORS

Article

Developing "Off the Shelf" Pancreases for Diabetic Patients Using Bacterial and Kombucha Tea Waste

Angelin Mathew[1], Leya Joykutty[1]
[1] American Heritage School, Plantation, Florida

SUMMARY

The advent of tissue and organ engineering provides long-term treatment for conditions previously considered chronic and untreatable. Through advances in the field of tissue engineering, patients have the potential to receive synthetic replacements of damaged tissues and cellular grafts. Scaffolds, based in either synthetic or natural polymers, are fundamental to tissue engineering approaches because they provide a structure that mimics the native environment which facilitates cellular differentiation, organization, and functionality. However, current protocols for creating scaffolds remain complex and difficult to translate to the clinic. Our investigation aimed to provide potential solutions to fundamental issues associated with islet cell transplantation, a possible cure for type 1 diabetes. In this study, we used bacterial cellulose as the polymer to create scaffolds. We modulated the structural characteristics of the bacterial cellulose to aid cellular infiltration. After processing, scanning electron micrographs of the scaffolds showed that a favorable blood vessel morphology was maintained and an open pore geometry was obtained. We effectively manipulated the porosity of the scaffold by altering agarose concentrations. The 0.5% agarose-cellulose composite group had an average pore area of 20,000 μm², which permitted the establishment of regionalized cells islands. Notably, the popular fermented tea drink, kombucha, produces bacterial cellulose as a waste product. Kombucha is made using a symbiotic culture of bacteria and yeast (SCOBY). Normally, SCOBYs are simply discarded after the fermentation process is complete, but could have untapped potential as a platform for tissue engineering and transplantation procedures. To verify that bacterial cellulose can be used as a biomimetic platform, INS-1 cells (an insulin-secreting beta cell-derived line) were seeded in the bacterial cellulose scaffold. We observed morphological changes, such as cytoplasmic extensions and clustering, suggesting reestablishment of functional cell islands. Hence, the results of our experiments suggested that bacterial cellulose is a cost-effective scaffolding platform that can be used to house islet cells as a promising tool in islet cell transplantation, a possible cure for diabetes.

INTRODUCTION

Utilizing artificially engineered tissues has the potential to provide holistic and long-term treatment for a wide range of diseases by offering large scale replacement of damaged organs and tissues. However, the clinical success of tissue engineering is currently confined to low-metabolism, acellular, prevascularized, and thin tissues (1). This investigation sought to use techniques from tissue engineering for islet cell transplantation, a promising cure for type 1 diabetes. Type 1 diabetes is a lifelong autoimmune disorder which results in the destruction of islets, the clusters of different cell types found within the pancreas. One of the cell types present, the beta cell, is responsible for insulin production. By receiving islet cell transplants as a replacement, patients can eliminate their dependence on external sources of insulin (2). However, one of the primary factors limiting the progression of tissue engineering and islet cell transplantation is failure to recreate the physical and chemical microenvironment the cells would naturally be found in (3).

Transplantation of islets requires a high cell density equivalent to that of 2-3 donors for each procedure. Within the context of the current organ shortage, where 1.2 million people are in need of an organ for transplantation, it is not likely that islet transplantation can be translated into a cure for type 1 diabetes (3). This high cell density required is partially attributable to the perishing of 60% of newly transplanted islets during the first 48 hours of implantation (4). In the initial steps of transplantation, islets are often irreversibly damaged through standard isolation protocols that involve chemical digestion by proteolytic enzymes, intense mechanical stress, and subsequent purification techniques. Without a support structure, islets are subsequently unable to reestablish their native clustered microenvironment. As a result, functionality is hindered, hypoxic injuries are induced, and effective maintenance of normal levels of blood sugar is prevented (5).

Scaffolds are gaining attention within the scientific community as a 3D framework for cell attachment and proliferation. An ideal scaffolding would be biocompatible, biodegradable, and cost-effective (6). The findings of this study suggest that bacterial cellulose, the most abundant biopolymer, is a cost-effective, sustainable, and easily tunable platform that can fulfill these requirements.

As a natural polysaccharide-based polymer, bacterial cellulose shares several chemical similarities to the native extracellular matrix which is rich in glycosaminoglycans, glycoproteins, and glycolipids (7). The ability of cellulose to generate biological cues has been linked to its glycan unit (7). Although bacterial cellulose is chemically similar to plant cellulose, bacterial cellulose does not require intense processing for the removal of intermediates such as lignin and hemicelluloses (8). *Gluconacetobacter xylinus* is a bacterial species known to secrete polymer chains that assemble as a cellulose membrane at the air-liquid interface (8). Amongst easily obtainable sources of *G. xylinus*, the fermented tea

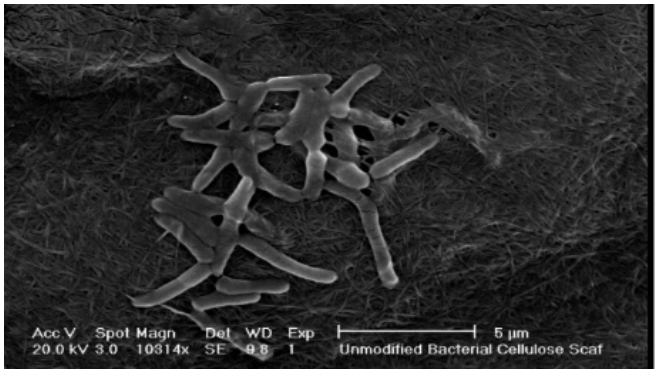

Figure 1: Scanning electron micrograph showing the process of bacteria secreting cellulose that forms membranes with interwoven nanofibrous structures.

drink kombucha has symbiotic cultures of acetic acid bacteria (*Gluconoacetobacter* and *Komagataibacter* species), lactic acid bacteria (*Lactobacillus* and *Lactococcus* species), and yeast (*Saccharomyces cerevisiae*). Previous research has demonstrated that the microbial agents within kombucha tea can also create tightly interwoven nanofibrous cellulose structures (9).There has been limited research on the use of bacterial cellulose as a scaffold platform for islet cell transplantation. Therefore, we also sought to study the potential of kombucha cellulose-based scaffolds for islet cell transplantation.

A potential challenge in using unmodified bacterial cellulose membranes as scaffolds is that they lack the macropores necessary for cell attachment, infiltration, and vascularization (10). While techniques ranging from particulate leaching, solvent casting, gas-foaming, microsphere sintering, and electrospinning have been used to create pores, reports of cell toxicity from residues have been noted (11). These techniques also require expensive infrastructure, materials, and equipment (11). Alternatively, agarose is a promising compound capable of creating pores that has been investigated in the context of creating composite scaffolds for bone tissue engineering (12).

In Phase 1 of our investigation, we utilized a range of agarose concentrations to create macroporous scaffolds and manipulate the porosity of the bacterial cellulose scaffolds. We hypothesized that a greater amount of agarose would result in a greater pore size. In Phase 2 of our investigation, we hypothesized that both the bacterial cellulose derived from pristine cultures of *G. xylinus*, and the cellulose derived from symbiotic yeast and bacterial cultures in Kombucha tea would serve as a platform compatible for INS-1 cell attachment.

Bacterial cellulose and agarose composites with macroporous structures were developed as a scaffold platform. Furthermore, preliminary cell seeding studies corroborate the potential applicability of bacterial cellulose for islet cell transplantation scaffolds. The approach we took in this study to provide a platform mimicking the microenvironment is not only cost-effective but also sustainable.

RESULTS

Agarose Allows for the Creation of Macroporous Bacterial Cellulose Scaffolds

In Phase 1 of our investigation, we hypothesized that altering agarose concentrations would enable creation of *G. xylinus* (pristine, single culture) cellulose-based scaffolds with different pore morphologies. We ranged the concentrations from 0.5% to 1%. Specifically, we hypothesized that 1% agarose-bacterial cellulose (BCA) would have the greatest average pore area. To characterize the morphology of the scaffolds' fibers and pores, we used scanning electron microscopy to measure the area of each pore.

The fiber morphology naturally produced by *G. xylinus* is analogous to the pancreas' blood vessel morphology and fiber arrangements achieved by the process of electrospinning (**Figure 1**). Electrospinning is a synthetic fabrication technique which creates organized nanofiber structures in polymers. We processed the cellulose membranes by homogenizing with an immersion blender and adding agarose increased the surface area of the 1.5 cm diameter scaffold while maintaining the intrinsic nanofibrous structures unique to cellulose **(Figure 2)**. Specifically, physical interconnections between the fibers were intact, and pores, defined as circular cross sections of 2D spaces, were present in processed agarose-cellulose composites.

The cellulose-agarose composite scaffolds displayed an open pore geometry while the control scaffolds, unmodified bacterial cellulose, displayed no pores on their surfaces (**Figure 2**). The average pore areas were 20,000 µm, 6,000 µm, and 2,000 µm for the 0.5%, 0.75%, and 1% bacterial cellulose agarose composites, respectively **(Figure 3,** $p < 0.05$**).** The statistical significance of these results was analyzed by using a one-tail t-test and comparing the pore areas of the bacterial-cellulose agarose composite groups to those of the unprocessed bacterial cellulose scaffolds with a

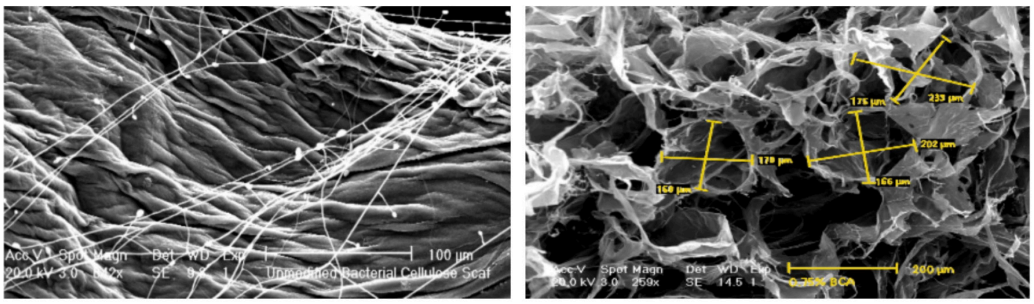

A: Unmodified Bacterial Cellulose Scaffold B: Composite Bacterial Cellulose-Agarose Scaffold

Figure 2: Scanning electron microscopy of composite scaffolds showed macropores formed through the addition of agarose. A) Scanning electron micrograph of an unmodified bacterial cellulose scaffold containing no pores. B) Scanning electron micrograph of a 0.75% bacterial cellulose-agarose scaffold with pores indicated by yellow outline.

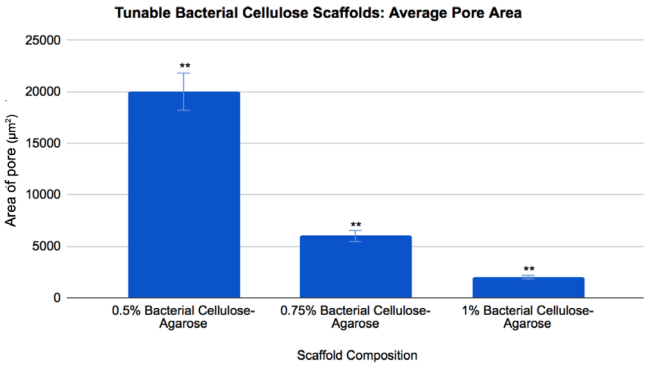

Figure 3: The average pore size areas (μm²) were calculated for each scaffold group through scanning electron microscopy. Three samples from each scaffold group were characterized and four randomized images of each scaffold were taken (total of 12 images for each group). The error bars indicate the standard deviation from the average pore size of each respective scaffold group. Asterisks are included on groups with $p < 0.05$ from a one-tailed t-test suggesting statistical significance.

threshold of significance of $p < 0.05$. Our initial hypothesis was not supported as the opposite effect was noted; processing with greater amounts of agarose led to a significantly smaller pore area (up to three times less with $p < 0.05$). Although changes in overall porosity were not predicted, processing with larger quantities of agarose decreased the number of pores.

The bacterial cellulose scaffolds show a remarkable ability to absorb fluids and maintain structural integrity. This feature is important to characterize in scaffolds because it determines the structure's ability to retain cell and fluid without dissolving. The lyophilized bacterial cellulose scaffolds could hold 400 μL of phosphate buffered saline while the lyophilized bacterial cellulose-agarose could hold 800 μL of phosphate buffered saline prior to losing structural integrity and dissolving **(Figure 4).** When normalized to weight, this meant that the lyophilized bacterial cellulose scaffolds had an average swelling ratio of 36 times their initial mass while lyophilized bacterial cellulose-agarose scaffolds had an average swelling ratio of 38 times their initial mass **(Figure 4).** The difference in swelling ratios is likely due to differences in porosity as detailed above.

INS-1 cells are compatible with Pristine Bacterial Cellulose and Kombucha-Based Bacterial Cellulose Scaffolds are Compatible with INS-1 Cells

In Phase 2 of this investigation, we aimed to assess the feasibility of using bacteria-derived cellulose as a platform for cell attachment. We hypothesized that bacterial cellulose-based scaffolds derived from *G. xylinus* and symbiotic cultures would aid in restoring native islet morphology. Kombucha-derived cellulose was utilized to analyze the potential tissue engineering applications of a widespread alternative to single culture-derived bacterial cellulose.

Pictures taken after seeding INS-1 cells in the well plates (coated with kombucha derived cellulose or containing no cellulose coating) and overnight incubation displayed morphological changes that indicate cell attachment onto the scaffolds. Cells seeded in the well plate coated with kombucha-derived cellulose had visible cytoplasmic extensions and congregated in native island-like clusters **(Figure 5D, Figure 5F)**. The INS-1 cells seeded in wells coated with kombucha derived cellulose displayed similar morphologies to INS-1 cells seeded in tissue culture coated wells, the positive control **(Figure 5D, Figure 5B)**. Due to material and time limitations, further quantification of the cells' viability could not be performed.

DISCUSSION

This study aimed to address primary challenges in islet cell transplantation by investigating agarose-bacterial cellulose as a macroporous scaffold platform on which insulin secreting islet cells could be seeded and transplanted with. The findings of this investigation can also be applied to the larger fields of tissue and organ engineering because of the simplicity of the technique utilized. For example a challenge in cardiac tissue engineering is that myocytes require recreation of unique intracellular junctions to produce mechanical contractions that pump blood forward (13). The scaffold described in this study supports the cell-to-cell contact necessary for optimal functionality of islet cells. Other fields such as neural tissue and kidney tissue engineering which culture cells with highly specialized functions could also benefit. The electric

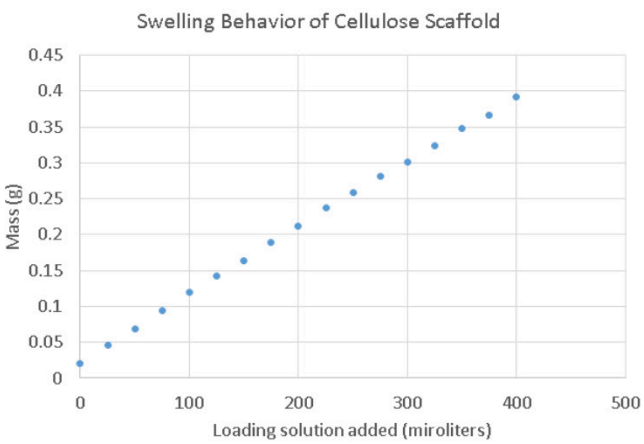

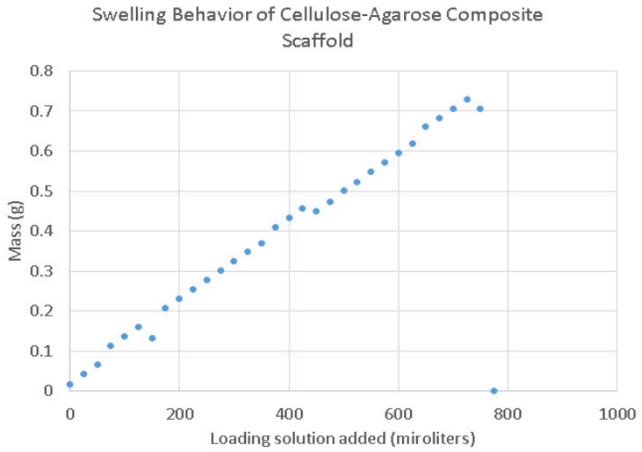

Figure 4: Swelling capacities of the lyophilized bacterial cellulose and bacterial cellulose- agarose composite scaffolds were assessed by determining the amount of phosphate buffered saline which the samples could retain. The endpoint was determined once structural integrity was lost. The unmodified scaffold had an average swelling capacity of 36 times original weight while the composite scaffolds had a swelling capacity of 38 times original weight.

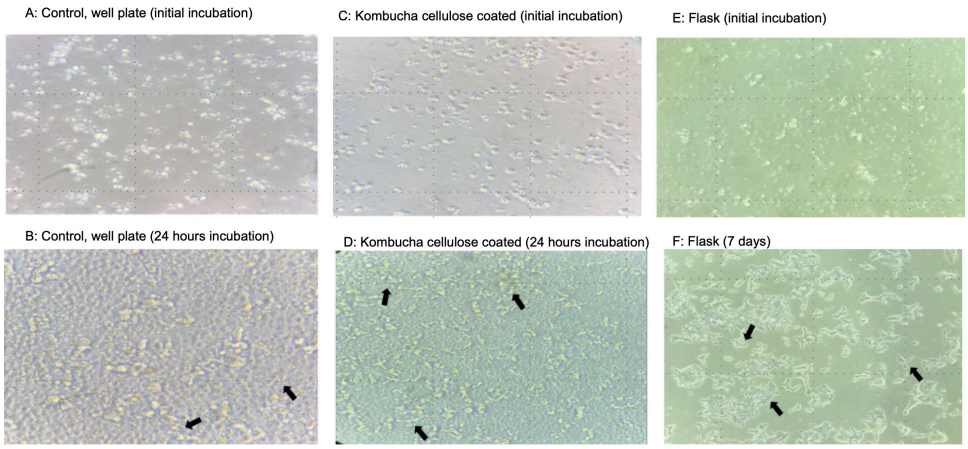

Figure 5: Images showing morphologies of the INS-1 cells seeded on control (A) and kombucha-derived cellulose (C). The first row shows INS-1 morphology after the cells were initially seeded (A, C). The second row depicts INS-1 cell morphological changes following 24 hours of incubation (B, D). Native islet cell morphology after 2 hours of seeding (E) and culturing for a week in a flask is (F). The arrows point to the clustering and island-like morphology and cytoplasmic extensions which are characteristic of INS-1 cells.

stimulation of neurons and filtration performed by nephrons are dependent upon cell-to-cell contact and the physical properties of their natural environments (14,15).

As a scaffolding platform, bacterial cellulose is different from synthetic and oil-based polymers as it is easier to obtain, environmentally friendly, and can be cultivated from a renewable source. The intrinsic nanofibrillar structure of bacterial cellulose is similar to the pancreatic blood vessel morphology previously well characterized in the literature (16). In Phase 1 of experimentation in which we aimed to create porous scaffolds with dimensions suitable for islet cell culture, the data supported our hypothesis that processing *G. xylinus*-based bacterial cellulose with agarose could create pores with dimensions suitable for islet cell culture. However, the second portion of our hypothesis was not supported. A greater concentration of porogen did not correspond to larger average pore areas. We postulate that this trend was observed because the greater concentrations of agarose had a "clogging" effect between the fibers. This addition of agarose as a one-step modulation to alter the entire structure of the scaffold offers an efficient methodology which enhances porosity. Hence, the need for additional procedures and equipment such as electrospinning, particulate leaching, gas infusion, and phase separation can be eliminated.

In the Phase 2 of experimentation, we performed cell-seeding studies to observe the morphological changes in islet cells when cultured on substrates coated with bacterial cellulose derived from pristine cultures and symbiotic cultures of kombucha. We demonstrated that bacterial cellulose facilitates favorable islet cell morphology changes such as cytoplasmic extensions and cell clustering. The two component system of the bacterial cellulose, derived from pristine bacterial culture and kombucha cellulose scaffold, and INS-1 cells demonstrated the first step towards using this biomaterial as a platform to support INS-1 cells and regulate cell morphology without added adhesion promoters. Although additional viability and metabolic assays could not be performed (such as the MTT assay), the results of this preliminary cell study suggest that bacterial cellulose based scaffolds have the potential to serve as a platform for INS-1 cell attachment and proliferation.

Future research should be done to better elucidate chemical and physical differences between bacterial cellulose produced by the symbiotic colonies of kombucha and the single strain of *G. xylinus*. Although kombucha waste-based bacterial cellulose could be an untapped high-value biomaterial, batch to batch variability should be considered and further studied. The variations in strains of symbiotic bacteria and yeast cultures, supplements added to recipes while brewing, carbohydrate source, pH, and temperature between each factory and distributor can potentially result in alteration to fiber architecture and orientation.

Prior to the clinical translation of the bacterial cellulose-agarose scaffolds proposed in this investigation, several additional material characterizations and cell studies are necessary to verify the biocompatibility of the scaffold. Immune responses to scaffold implants are the leading cause of failure of tissue engineering products (17). Cytokine and chemokine release levels can be used as indicators for inflammatory responses.The chemical properties and constituents of kombucha and pristine bacterial cellulose scaffolds can be profiled for factors known to contribute to inflammatory and immune rejection responses (17). Such chemical analysis can be useful in the process of optimizing alternate purification techniques (e.g. alternatives to the sodium hydroxide incubation) as kombucha tea SCOBYs typically have higher sugar residues on the cellulose membrane when compared to cellulose membranes synthesized by a monoculture of *G. xylinus*.

Furthermore, studies to quantify INS-1 cell proliferation and insulin release while seeded on the bacterial cellulose scaffolds should be performed. Since nuclear factor-κB and poly(ADP-ribose) polymerase (PARP) are proteins involved in major pathways associated with necrosis of islet cells, assays can be performed to characterize up/down regulation of these pathways over an extended period of time in cells seeded onto the bacterial cellulose scaffolds for viability (16). We also recommend that when the aforementioned studies are performed, cell culture conditions should mimic stress induced by islet isolation (18).

Existing literature suggests that the reduced bioactivity of synthetic scaffolds results in lower rates of cell adhesion

and implant fibrosis; however, comparison of the bacterial cellulose scaffolds proposed in this study to existing synthetic and natural polymer-based scaffolds will be better informed by the aforementioned studies. Additionally, there are numerous avenues to tailor the bacterial cellulose scaffold designed in this study. Testing different compositions of the cellulose-agarose composites can allow for the creation of macroporous and microporous bacterial cellulose scaffolds to suit other cell types. Modifications to the nanofibrous structure such as alignment, interconnectivity, width and the role of all these factors in vascularization and insulin release could also be studied.

Overall, the results of this study are promising, as scaffolds can be developed sustainably and processed cost-effectively by using bacterial cellulose and agarose. The kombucha and *G. xylinus*-derived bacterial cellulose macroporous scaffolds have the potential to be used as a platform technology in tissue engineering and can be functionalized (the addition of therapeutics/growth factor like compounds) in the future.

MATERIALS AND METHODS

Cultivating and Harvesting Cellulose from *G. xylinus*

We prepared media for bacterial growth using the following reagents purchased from Millipore Sigma: 5.0 grams of yeast extract, 3.0 g of peptone, and 25.0 g of mannitol dissolved in 1 L of distilled water and autoclaved overnight. In Phase 1, bacterial cellulose-based scaffolds were prepared by culturing *G. xylinus* bacteria (ATCC) in mannitol-based broth for two weeks. The cellulose membranes were aseptically removed and washed with distilled water to achieve a neutral pH of 7. The membranes were then sterilized by incubating in a 0.25 M sodium hydroxide solution for seven days.

Preparing Composite Cellulose- Agarose Scaffolds

To prepare cellulose-agarose composites, cellulose membranes were homogenized using an immersion blender. We added 0.5%, 0.75%, and 1% weight by weight of agarose to the cellulose homogenate. The composite solutions were autoclaved overnight and transferred into 24-well plates (2 g per well). The composites were frozen at -86 °C and then lyophilized.

Characterizing Physical Properties of Bacterial Cellulose Scaffolds

Scanning electron microscopy was performed on three samples for each composite group after sputter coating with palladium. Four pictures of randomly selected areas were taken for each scaffold sample. ImageJ›s near-distance plug-in was used to standardize pore selection and to measure the area of the 2D circular cross section of the pores in the scaffold samples. Averages and distribution of pore areas were analyzed for the three composite groups followed by statistical analysis using a one-tailed t-test (Excel).

To measure the swelling ratios and rates of the unmodified and cellulose-agarose composite scaffolds, the initial masses of eight scaffolds (four cellulose-agarose composites and four unmodified scaffolds) were noted. Scaffolds were loaded with 15 µL increments of phosphate buffered saline. The masses of the scaffolds were recorded until scaffold integrity was lost. The swelling ratios of scaffolds were calculated by comparing the averages of final swollen mass and initial dry mass of the four unmodified and four composite scaffold samples.

Cell Seeding Studies

Preliminary cell studies were conducted to validate bacterial cellulose as an islet cell compatible platform. A rat insulinoma-derived islet cell line, INS-1, was provided by AddexBio and used as the model. Kombucha-derived bacterial cellulose was obtained by cultivating a SCOBY (symbotic yeast and bacterial culture) from Kombucha Kamp in a tea medium containing Lipton's "America's Favorite" tea bag, one cup of sugar, and the starter culture liquid provided. The cellulose membranes were sterilized by using the same method as described for sterilizing cellulose membranes synthesized by *G. xylinus*. Slurries of pristine bacterial cellulose and kombucha-derived cellulose were created by adding a 1:1 weight/weight ratio of cellulose and sterile, deionized water. The bottoms of sterile well plates were coated with 100 µL of the suspension and further sterilized using ultraviolet radiation in the cell culture hood for 16 hours. INS-1 cell suspensions were stained with Trypan Blue to count cell viability. The INS-1 cells were then seeded at a density of 300,000 cells per well. Images were taken after 2 hours of incubation and at the endpoint of 24 hours following incubation by randomly selecting 4 areas in each well. Morphological changes such as cytoplasmic extensions and settlement in colonies were documented and compared to morphologies of cells seeded on standard, tissue culture coated wells.

Received: May 18, 2019
Accepted: January 12, 2021
Published: March 8, 2021

ACKNOWLEDGEMENTS

I would like to thank American Heritage School for allowing me to conduct my investigation in the BSL-2 Lab facility. I would also like to thank Dr. Scott for her assistance in navigating the facilities available at the University of Miami, Dr. Parab for his assistance with lyophilizing samples, and Dr. Balckwelder for enabling me to characterize the scaffold samples through scanning electron microscopy.

REFERENCES

1. Chang, William, *et al*. "A Short Discourse on Vascular Tissue Engineering." *Npj Regenerative Medicine*, vol. 2, no. 1, 2017, doi:10.1038/s41536-017-0011-6.
2. Bottino, Rita, *et al*. "The Future of Islet Transplantation Is Now." *Frontiers in Medicine*, vol. 5, 2018, pp 202 13 Jul. 2018 doi:10.3389/fmed.2018.00202.
3. Solez, K *et al*. "The bridge between transplantation and regenerative medicine: Beginning a new Banff classification of tissue engineering pathology." *American journal of transplantation : official journal of the American Society of Transplantation and the American Society of Transplant Surgeons* vol. 18,2 (2018): 321-327. doi:10.1111/ajt.14610
4. Ellis, Cara, *et al*. "Regenerative Medicine and Cell-Based Approaches to Restore Pancreatic Function." *Nature Reviews Gastroenterology & Hepatology*, vol. 14, no. 10, 2017, pp. 612–628., doi:10.1038/nrgastro.2017.93.
5. Komatsu, Hirotake *et al*. "Impact of Oxygen on Pancreatic Islet Survival." *Pancreas* vol. 47,5 (2018): 533-543. doi:10.1097/MPA.0000000000001050
6. Jalili, Reza, *et al*. "Biocompatible Scaffolds: An Effective

Means for Improving Islet Cells Viability and Function." *International Journal of Diabetes and Clinical Research*, vol. 4, no. 2, 2017, doi:10.23937/2377-3634/1410076.3
7. Tiwari, Sanjay, *et al*. "Polysaccharide Based Scaffolds for Soft Tissue Engineering Applications." *Polymers*, vol. 11, no. 1, 2018, p. 1., doi:10.3390/polym11010001.
8. Esa, Faezah, *et al*. "Overview of Bacterial Cellulose Production and Application." *Agriculture and Agricultural Science Procedia*, vol. 2, 2014, pp. 113–119., doi:10.1016/j.aaspro.2014.11.017.
9. Dima, Stefan-Ovidiu, *et al*. "Bacterial Nanocellulose from Side-Streams of Kombucha Beverages Production: Preparation and Physical-Chemical Properties." *Polymers*, vol. 9, no. 12, 2017, p. 374., doi:10.3390/polym9080374.
10. Nagashima, Aya, *et al*. "A Uniaxially Oriented Nanofibrous Cellulose Scaffold from Pellicles Produced by G. xylinus in Dissolved Oxygen Culture." *Carbohydrate Polymers*, vol. 135, 2016, pp. 215–224., doi:10.1016/j.carbpol.2015.08.077.
11. Chocholata, Petra, *et al*. "Fabrication of Scaffolds for Bone-Tissue Regeneration." *Materials*, vol. 12, no. 4, 2019, p. 568., doi:10.3390/ma12040568.
12. Torgbo, S., *et al*. "Bacterial cellulose-based scaffold materials for bone tissue engineering". *Science Direct,* vol. 11, p 34-39, doi.org/10.1016/j.apmt.2018.01.004
13. Lv, Xiangguo, *et al*. "Bacterial Cellulose-Based Biomimetic Nanofibrous Scaffold with Muscle Cells for Hollow Organ Tissue Engineering." *ACS Biomaterials Science & Engineering,* vol. 2, no. 1, Mar. 2015, pp. 19–29., doi:10.1021/acsbiomaterials.5b00259.
14. Dumanli, Ahu Gumrah. "Nanocellulose and Its Composites for Biomedical Applications." *Current Medicinal Chemistry,* vol. 24, no. 5, 2017, pp. 512–528., doi:10.2174/092986732366616101412400 8.
15. Loh, Qiu *et al*. "Three-Dimensional Scaffolds for Tissue Engineering Applications: Role of Porosity and Pore Size." *Tissue Engineering Part B: Reviews*, vol. 19, no. 6, 2013, pp. 485–502., doi:10.1089/ten.teb.2012.0437.
16. Takahashi, Hiromi, *et al*. "Scanning Electron Microscopy of the Rat Exocrine Pancreas." *Arch.histol. jap.*, Vol. 47, No. 4 (1984) p. 387-404., doi: 10.1679/aohc.47.387
17. Crupi, Annunziata, *et al*. "Inflammation in Tissue Engineering: The Janus between Engraftment and Rejection." *European Journal of Immunology,* vol. 45, no. 12, 2015, pp. 3222–3236., doi:10.1002/eji.201545818.
18. Bottino, Rita, *et al*. «Response of human islets to isolation stress and the effect of antioxidant treatment.» *Diabetes* 53.10 (2004): 2559-2568.

JOURNAL OF
EMERGING INVESTIGATORS

Article

Effect of mass and center of gravity on vehicle speed and braking performance

Jack Tian[1] and Clifford Whitfield[2]

[1] Troy High School, Fullerton, CA

[2] Department of Mechanical and Aerospace Engineering, The Ohio State University, Columbus, OH

SUMMARY

The center of gravity (CG) of a vehicle is a key parameter that helps determine vehicle stability, braking efficiency, and safety. In a gravity vehicle, the mass of the vehicle is also an important factor in vehicle performance because it provides the sole force of propulsion. We hypothesized that if a vehicle was constructed according to mathematically-derived optimal mass and CG location, then a fast and accurate vehicle would result. To test this hypothesis, we constructed a gravity vehicle, which is a vehicle powered by its own gravity on a ramp. Mathematical calculations were used to rationalize this hypothesis. Shifting the CG rearward increased the vehicle's effective launching height on the ramp and corresponding gravitational potential energy, resulting in greater kinetic energy and speed. However, the accuracy (m^{-1}), defined as the reciprocal of braking distance from the target, increased initially, peaked, and then decreased as the vehicle mass increased. We performed experiments with five mass parameters and three load locations, using an unloaded vehicle as control. Speed and accuracy were then measured for 16 sets of data. Compared to front and centrally-loaded vehicles, the rear-loaded vehicles displayed the best results. As the mass increased to a medium value, both the speed and accuracy reached a maximum. The experimental results supported the hypothesis that the optimal CG position is 22 ± 1 cm rear of the front axle and the ideal mass is 867 ± 50 grams. This study highlights the significance of CG position in vehicle design.

INTRODUCTION

The center of gravity (CG) is a critical parameter that impacts vehicle handling, since the CG position in each spatial axis affects the vehicle's stability, ride comfort and safety. Accordingly, it is crucial for calculations of vehicle performance parameters. In this study, we developed a model to determine the optimal vehicle mass and CG location for a fast gravity vehicle with high braking accuracy. We drew on previously reported methods including algorithms, software-based model simulations, real-time estimates and more, to determine the optimal CG location. Previous studies reported that moving the battery pack along the electric vehicle significantly impacted the mass distribution (1). A model-based simulation using MATLAB SIMULINK was presented to demonstrate the effect of changing CG position on vehicle stability (1). Albeit with different purpose, this study formed the basis of our hypothesis. Other vehicle parameters were also informed by previous studies. For example, a study on vehicle load found that an increase in CG height results in a decrease in maximum driving speed since stability decreases as CG height increases (2). Therefore, in order to minimize the adverse impact of the height of CG on vehicle stability, the vehicle was designed to move as closely as possible to the ground. Skrucany *et al*. investigated the influence of cargo weight and its position on brakes. They demonstrated that loads should be as close to the ground and rear axle as possible to reduce the braking distance (3, 4). These considerations were also taken into account in the design of the vehicle. We drew on models developed by Mehmet *et al*. (5) in order to optimize the height, horizontal position, and lateral position of the CG of a vehicle. We designed the vehicle braking system for optimal braking accuracy. Lee *et al*. proposed a practical algorithm for estimating a vehicle's longitudinal CG location in real time, and its viability was verified through simulations and experiments using a test vehicle equipped with electro-mechanical brakes on the rear wheels (6). The braking concept in this report helped in designing an efficient braking system.

From these studies, we gained insight into how to construct a fit-for-purpose gravity vehicle. We chose smaller wheels to lower the height of the CG, and we used a lightweight, symmetric, and even basswood board as the chassis so that the lateral CG was located on the center line. However, the most important takeaway from the previous studies was that a rearward shift in CG could significantly increase braking accuracy.

During vehicle construction, it became apparent that the vehicle's mass and CG position would impact the vehicle's speed and accuracy. With a vehicle in hand, we asked two questions: What was the optimal mass and where was the best CG location? In the ready-to-launch position, the vehicle was hung vertically on the bolt of the trigger. Accordingly, a rearward CG would theoretically result in a greater starting height and potential energy, which is converted to higher departure speed at the bottom of the ramp. Previous studies showed that a CG location as close as possible to the rear axle not only increased vehicle stability, but also significantly reduced braking distance (3, 4). Based on these conclusions, we predicted that the best CG location would be close to the vehicle's rear axle. On the other hand, when the vehicle reaches the desired speeds through manipulation of the CG towards the rear, the vehicle mass becomes a crucial factor in its accuracy. With greater mass, there is greater momentum, which could exceed braking endurance and cause vehicle

Figure 1: Gravity Vehicle with Different Mass Loading. (A) The front load was located behind the front axle due to the dowel in front of the axle. (B) The load was located at the middle point of the vehicle length, and the load behind the rear axle. All three load configurations were located on the center line and secured with duct tape to prevent movement during the run.

skidding. We therefore hypothesized that a medium-mass vehicle might display the best braking accuracy. To rationalize the two hypotheses, we built physics models for the analysis of energy conversion and braking forces. From the model studies, we concluded that a medium-mass vehicle with the rearward CG would have high speed and accuracy. We performed trials with five mass parameters and three location variables, along with the unloaded vehicle as a control. We graphed the resulting data to determine how CG position and vehicle mass impact the accuracy and speed.

RESULTS

We conducted the experiments that obtained the optimal mass and CG location with a gravity vehicle device, which uses the vehicle's gravitational potential energy on a ramp as the sole means of propulsion to arrive at a target as quickly and accurately as possible. We built a ramp with a height of no more than 100.0 centimeters and a 50.0 cm x 50.0 cm base, as well as a vehicle with a mass of no more than 2.000 kilograms (7). The target was arranged between 9.00 to 12.00 meters away from the bottom of the ramp. Both the run time and braking distance were measured to evaluate vehicle performance. The vehicle speed was calculated as the distance traveled by the vehicle divided by the time measured from the launch to the end of the vehicle's run. A round wooden dowel was attached to the front of the vehicle. The braking distance was measured from the dowel's front bottom edge to the center of the target. To facilitate comparison of braking performance, the concept of accuracy (m^{-1}) was introduced by dividing 100 by the braking distance (m). The shorter the braking distance, the higher the vehicle accuracy.

With an unloaded vehicle (507 grams) as a control, 120 grams of load (mass + tape) were added on three positions on the vehicle: the front, middle and rear (**Figure 1**), to investigate their impact on vehicle behavior. The rear loadings yielded the best results compared with corresponding middle and rear loadings of the same mass (**Table 1**). We observed a trend where both accuracy and speed are independent of the vehicle's mass, increasing as the CG position was moved rearward (**Figure 2A & 2B**). On the other hand, as the vehicle mass was increased from 507 to 867 grams, both accuracy and speed increased for all masses of vehicle. However, further increases of the vehicle mass from 867 to 1107 grams resulted in a decrease in accuracy while the speed remained unchanged. The CG was shifted away from the front axle as the mass load was moved from the front to the middle to the rear location (**Table 1**). Increasing the mass in the rear from 627 to 1107 grams strengthened the rearward trend of the CG.

Plotting the accuracy against vehicle mass (**Figure 3A**) resulted in an approximately normal distribution. When the mass load of 360 grams was placed onto the rear part of the vehicle, the greatest accuracy was achieved (**Table 1**). Meanwhile, graphing the speed against vehicle mass (**Figure 3B**) produced an *S*-shape curve with a peak, indicating that when the mass was beyond 867 grams, the speed had reached its maximum. Compared to the unloaded control, the vehicle with a mass of 867 grams and rear loading displayed an 89% increase in accuracy and a 26% increase in speed. These experimental results support the hypothesis that the

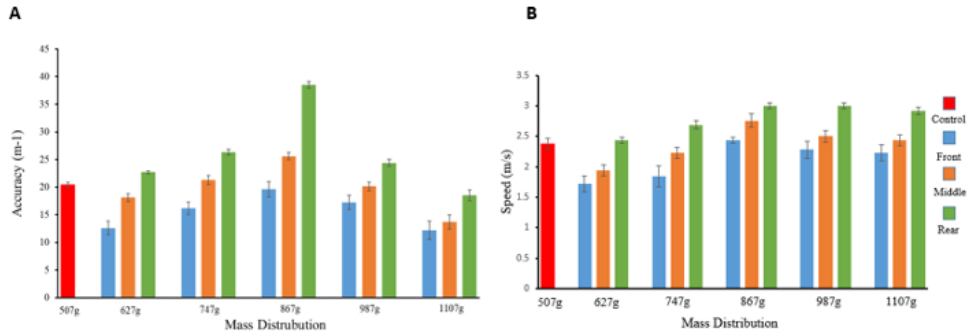

Figure 2: Effect of CG Location on Accuracy and Speed. The average (A) accuracy (m^{-1}) and (B) speed (m/s) of (specify) was measured for 6 different weights of a gravity vehicle (507, 627, 747, 867, 987, and 1107 g) as the load was moved from the front (blue), middle (orange), and rear (green) of the vehicle. Measurements were compared to an unloaded vehicle as a control (red) (n = 3). Error bars represent two standard deviations.

Vehicle Mass (grams)	Loading Mass Location	CG Distance from Front Axle (cm)	Results			
			Average Distance (cm)	Accuracy (m^{-1})	Average Time (s)	Speed (m/s)
507	None	14.0	4.9	20.4	4.4	2.39
627	F	11.9	7.9	12.6	6.1	1.72
	M	14.2	5.5	18.1	5.4	1.94
	R	17.6	4.4	22.7	4.3	2.44
747	F	10.5	6.2	16.1	5.6	1.85
	M	14.3	4.7	21.3	4.7	2.23
	R	20.1	3.8	26.3	3.9	2.69
867	F	9.5	5.1	19.6	4.4	2.39
	M	14.3	3.9	25.6	3.8	2.76
	R	21.9	2.6	38.5	3.5	3.00
987	F	8.7	5.8	17.2	4.6	2.28
	M	14.4	5.0	20.0	4.2	2.50
	R	23.2	4.1	24.4	3.5	3.00
1107	F	8.1	8.2	12.2	4.7	2.23
	M	14.4	7.3	13.7	4.3	2.44
	R	24.3	5.4	18.5	3.6	2.92

Table 1: Vehicle's Mass and CG Location Effects on Accuracy and Speed. Accuracy (m^{-1}) was calculated by dividing 100 by average distance (m) from target while speed (m/s) was calculated as 10.5 m/average runtime (s). *F* represents the front location, *M* the middle location, and *R* the rear location. Every data value was obtained as an average from 3 trials.

vehicle with medium mass and CG position as close as possible to the rear axle would have the best performance.

DISCUSSION

Besides low friction, there are two main considerations with the ramp design: fast vehicle descent and efficient direction change. The vehicle gains speed from gravity and changes its direction of movement from downwards at the top of the ramp top to forward at the bottom of the ramp. A Brachistochrone curve meets these requirements, providing the theoretical shortest time in rolling from the top to the bottom of the ramp (8). The descent time has an integration relationship with the curve function y(x) as shown in Equation (1):

$$T = \int_o^x \sqrt{\frac{1+y'^2}{2gy}}\,dx \qquad (1)$$

where y' is the derivative of x and g represents the acceleration of gravity. To compromise short descent time and seamless connection between the ramp and floor, the ramp surface was made in the shape of a modified Brachistochrone curve.

As the gravity vehicle rolls down the ramp, gravitational potential energy is converted into translational and rotational kinetic energy. The vehicle moves on the track until it brakes at the target. During the braking process, the kinetic energy of the vehicle is converted into elastic potential energy stored in the torsion spring. The torsion spring functions as an energy storage by generating negative torque to oppose the motion of the vehicle (9). After each run, the energy stored in the spring is released manually so that another run can start. Each run of the vehicle involves the Law of Energy Conservation. If energy loss is negligible, gravitational potential energy of the vehicle is fully converted into the elastic potential energy stored in the torsion spring (**Figure 4**). The vehicle that starts from the rest at the top of the ramp and stops at the target functions as an energy carrier. After each experiment, the energy stored in the spring is released manually so that another experiment can start.

Analysis of the vehicle's energy conversion provides theoretical evidence for the optimal vehicle mass range. When the trigger is pressed and the gravity vehicle rolls down the ramp, it undergoes changes in its energy state. Based on the Law of Energy Conservation, the vehicle's gravitational potential energy is converted into kinetic energy since the energy loss from air resistance is negligible. The energy conservation equation is shown as:

$$K_i + U_i = K_f + U_f \qquad (2)$$

In this equation, the initial kinetic energy $K_i = 0$ and the final potential energy $U_f = 0$ of the bottom of the ramp are chosen as the references. Replacing U_i with MgH and K_f with translational ($^1/_2Mv^2$) and rotational ($^1/_2I\omega^2$) kinetic energy,

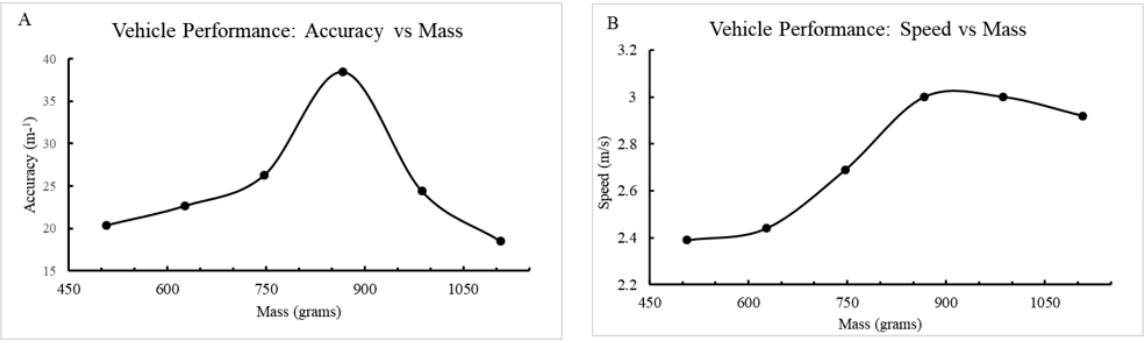

Figure 3: Vehicle Mass Effect on Accuracy and Speed. (A) The average (A) accuracy (m^{-1}) and (B) speed (m/s) of (specify) was measured for 6 different weights of a gravity vehicle (507, 627, 747, 867, 987, and 1107 g).

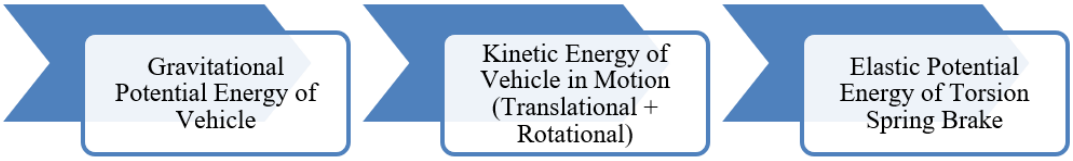

Figure 4: Energy Conversion of Gravity Vehicle. In each experiment, the gravity vehicle converts its own gravitational potential energy at the ramp top to kinetic energy in motion to elastic potential energy stored in the torsion spring.

where M is the vehicle mass, H is the launching height of the vehicle, v is the translational speed, I is the moment of inertia, and ω is the rotational speed. Equation (2) can be simplified as:

$$MgH = {}^1/_2Mv^2 + {}^1/_2I\omega^2 \quad \textbf{(3)}$$

Equation (3) shows that the vehicle's gravitational potential energy is converted into its translational speed (v) and rotational speed (ω). ω is proportional to v, in which R is the wheel radius. Since the body of the vehicle is not rotating, only the mass (m) of the wheels, axles and shafts contribute to the moment of inertia of the vehicle. Introducing , Equation (3) can be written as:

$$MgH = {}^1/_2Mv^2 + {}^1/_2({}^1/_2mR^2)({}^v/_R)^2 \quad \textbf{(4)}$$

and solved for velocity:

$$v = \sqrt{\frac{MgH}{\frac{1}{2}M+\frac{1}{4}m}} = \sqrt{\frac{gH}{\frac{1}{2}+\frac{m}{4M}}} \quad \textbf{(5)}$$

From Equation (5), assuming the friction is negligible when the vehicle slides down the ramp (m = 0), it will get the maximum speed: $v = \sqrt{2gH}$.

In contrast, when the nonrotating body mass is very small compared to rotating mass ($m \approx M$), the vehicle gets minimum speed $v = \sqrt{\frac{4gH}{3}}$.

In any case, we can conclude that a greater starting height (H) will increase the translational speed (v). Equation (5) also shows that as the total mass (M) increases, the vehicle speed increases when it arrived at the ramp bottom. However, this is the opposite to the vehicle moving on the track since the friction force (μMg) which decelerates the vehicle is proportional to the mass. A medium mass (M) achieves the best balance between these two opposing forces and yields the maximum speed. In addition, the greater the total mass (M) of the vehicle, the greater the momentum of the vehicle (p), as related by the equation:

$$p = Mv \quad \textbf{(6)}$$

A heavier vehicle has greater momentum, thus making it harder to brake. Based on Equations (5) and (6), we hypothesized that a medium-mass vehicle would give the best results because the mass must be decreased to reduce momentum without sacrificing speed. As the vehicle stops at the target, its kinetic energy is converted into elastic potential energy stored in the torsion spring. The conversion obeys the following energy

$${}^1/_2Mv^2 + {}^1/_2I\omega^2 = {}^1/_2k\theta^2 \quad \textbf{(7)}$$

where v is the speed when the vehicle starts braking, k is the spring constant, and θ is the twisting angle of the torsion spring. From Equation (7), greater vehicle speed (v) and mass (M) result in a larger twisting angle of the torsion spring. This conclusion is further supported by an analysis of the change of momentum (ΔP) and impulse (ΔJ) during the braking period. Since the final speed (vf) of the vehicle equals zero, the following equations may be derived as:

$$\Delta P = M\Delta v = Mv_f - Mv_i = -Mv \quad \textbf{(8)}$$
$$\Delta J = F\Delta t = -Mv \quad \textbf{(9)}$$

where F is the average deformation force with which the wingnut twists the spring during the braking period and Δt is the duration for which the spring is twisted. Equation (9) shows that to reduce the deformation force while maintaining high speed, the vehicle mass must be reduced since the braking period (Δt) keeps constant when the same spring is used.

The CG distance from the front axle can be calculated by center of mass equation:

$$X_{CM} = \frac{\sum m_i x_i}{M} = \frac{507(14)+m_{load}(D)}{507+m_{load}} \quad \textbf{(10)}$$

Where, m_{load} is 120, 240, 360, 480, and 600 grams and D is the distance (cm) from the front axle, 3.1 (front), 14.8 (middle) and 33 (rear) (**Table 1**).

This study shows that a vehicle with a rearward center of gravity and a medium mass result in greatest speed and braking accuracy. The results of this study can be applied to the future design of gravity vehicles with consideration of their centers of gravity and mass. Further investigation will be needed in order to translate the results of this study to large scale automobiles.

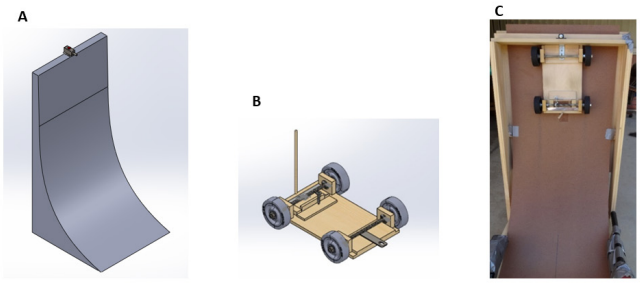

Figure 5: Gravity Vehicle Device. (A) CAD model of ramp created by SOLIDWORKS. The ramp fits within a rectangular box with a 50.0 cm x 50.0 cm base and a height of 100.0 cm. (B) CAD model of vehicle created with SOLIDWORKS. The vehicle has a dowel in the front for timing by photogate and a U-bolt plate in the rear for hanging on the trigger. (C) Ready-to-launch gravity vehicle. The gravity vehicle is hung at the top of the ramp. When the trigger button is pressed, the vehicle accelerates down the ramp due to its own gravity. The vehicle achieves maximum speed at the bottom.

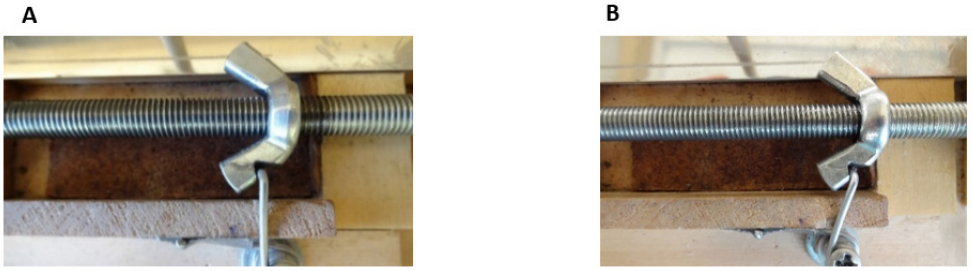

Figure 6: Braking System Composed of Wingnut Geared with Torsion Spring at a Specific Point. (A) The vehicle decelerates when the wingnut starts to gear with the torsion spring. (B) The vehicle stops moving when a static equilibrium between the rotational torque of the wingnut and the twisting torque of the torsion spring is established.

MATERIALS & METHODS

Materials and Construction of Gravity Vehicle

Figures 5A and 5B are sketches of the ramp and vehicle drawn with SOLIDWORKS 3D CAD Software (10), in which a trigger was installed at the top of the ramp. A Gravity Vehicle device was built to meet the requirements, in which a ramp has a 49.5 cm x 49.5 cm base and a height of 99.8 cm, and a vehicle has a length of 36 cm and a width of 24 cm (**Figure 5C**). The ramp was built with fiberboard, pine and poplar wood boards bound by wood glue and nails. All ramp materials were purchased from Home Depot. The vehicle was built with 4 Banebots wheels, a basswood chassis, a braking system, a dowel, wood mounts, and other parts. A wingnut, Teflon and rubber washers, a U-bolt plate, threaded axles, and compression springs were purchased from Ace Hardware. Wheels and shafts were purchased from BaneBots LLC. Miniature ball bearings were purchased from NationSkander California Corporation. Torsion springs were purchased from Grainger Industry Supply. A digital balance and stopwatch timer were purchased from Walmart. A push button spring latch used as the trigger mechanism was bought on Amazon and installed at the top of the ramp. The braking system was built with a wingnut and torsion spring. The wingnut moved along the threaded axle from left to right for a predetermined length based on the target distance. The torsion spring was installed with its coils concentric to a metal pin situated adjacent to the front axle so that a leg of the spring could gear with the wingnut at a specific point. The vehicle decelerated when the wingnut started to press the torsion spring (**Figure 6A**) and came to a full stop when a static equilibrium between the translational force of the wingnut and the deflection force of the spring was established (**Figure 6B**). If the elastic limit of the spring was exceeded, the spring was replaced with a stronger one.

Experimental Procedure

The target was set at 10.50 meters, halfway between 9.00 and 12.00 meters, in all experiments. To reduce systematic errors, each run was performed on the same wood floor. The vehicle rolls down from the top of the ramp and then across on the wood floor until the vehicle brakes at the target. The running time was measured by stopwatch from the launch to the vehicle stop. The average running time and braking distance were calculated by running three trials under the same conditions. The mass load was located on the center line and secured with duct tape to prevent movement during the run. In front loading, the distance between the center of the mass load and front axle was measured as 3.1 cm, 14.8 cm in the middle loading, and 33.0 cm in the rear loading.

Center of Gravity Modelling

Recent research by Patel *et al*. proposed a fast and practical method to determine the three-dimensional CG of any symmetric or asymmetric vehicle. By using force restoration technology and flexure pivots, all three axes of CG could be measured in a single setup with the accuracy up to 10 millimeters (11). Their method helped us develop the CG measuring practices in this study.

For the gravity vehicle, a simplified model for determining the CG location was constructed **(Figure 7)**. Due to its symmetric and low-height design, only CG locations along the longitudinal direction were considered for calculation. As the load was moved rearwards, the CG also shifted rearwards. If the two front wheels were placed on a balance while the two rear wheels were supported in the same horizontal plane, the normal force F_A exerted by the balance could be measured (**Figure 7A**). Switching the balance to the two rear wheels could yield the normal force F_B (**Figure 7B**). After measuring the two parameters F_A and F_B, the CG location could be calculated based on static equilibrium and Newton's second law. Once the CG position was determined, the height with which the vehicle was launched could also be obtained. Using this value, the approximate speed was calculated by the Law of Energy Conservation. Insight was thus gained on the effect

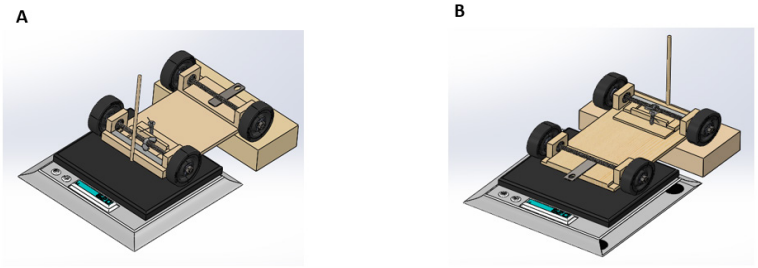

Figure 7: Simplified Vehicle Model for Determining the CG location. (A) The balance measures the normal force F_A on the front wheels. (B) The balance measures the normal force F_B on the rear wheels.

Figure 8: Diagram of Force Analysis. (A) The mass load (F_C) is located between the two fulcrums. F_A is the normal force from the front wheels, F_B the normal force from the rear wheels, and F_{CG} is the gravitational force at the CG. a is the distance of F_{CG} from the fulcrum A, b is the distance of F_{CG} from the fulcrum B, and c is the distance of F_C from the fulcrum B. (B) The mass load (F_C) is located behind the fulcrum B. All symbols are same as those of (A).

of the optimal CG position on speed and accuracy.

When the load is placed onto the vehicle, there are two scenarios: the load is located between two fulcrums A and B corresponding to front and middle loadings or the mass load is outside fulcrum B (**Figure 8**). In either case, the force equilibrium leads to the following equations based on Newton's second law:

$$F_{CG} + F_C = F_A + F_B \quad \textbf{(11)}$$
$$F_{CG} = F_A + F_B - F_C \quad \textbf{(12)}$$

Here, F_c is the gravity force from the mass load and F_A and F_B are measured by the balance. F_{CG} can be calculated from Equation (12). When the mass is located between the two fulcrums A and B, in terms of the torque equilibrium, two equations can be deduced as:

$$\text{For fulcrum B: } (a + b)F_A = bF_{CG} + cF_C \quad \textbf{(13)}$$
$$\text{For fulcrum A: } aF_{CG} + F_C(a + b - c) = F_B(a + b) \quad \textbf{(14)}$$

When the mass load is located outside fulcrum B, the two equations can be expressed as:

$$\text{For fulcrum B: } F_A(a + b) + cF_C = bF_{CG} \quad \textbf{(15)}$$
$$\text{For fulcrum A: } F_C(a + b + c) + aF_{CG} = F_B(a + b) \quad \textbf{(16)}$$

In either case, the distance *a* of the CG position from the dowel can be calculated from the combination of Equations (13) and (14) or Equations (15) and (16), since there are only two unknowns, *a* and *b*. The symbol *c* is the measured distance between the center of the mass load and fulcrum B.

Numerical Analysis

The optimal mass (867 grams) of the vehicle with a load outside of fulcrum B was taken as an example. From the measurements of F_A (1.92 N), F_B (10.18 N), and F_C (3.53 N), F_{CG} was calculated as:

$$F_{CG} = F_A + F_B - F_C = 8.57 \quad \textbf{(17)}$$

Introducing F_A (1.92 N), F_B (10.18 N), F_C (3.53 N), F_{CG} (8.57 N), and *c* (2.4 cm) into Equations (14) and (15), they were simplified as:

$$a + b = 29.6 \quad \textbf{(18)}$$
$$a - 3.46b = -4.41 \quad \textbf{(19)}$$

Solving the two-variable equations yielded *a* as 22.3 cm. The standard deviation was 22 ± 1 cm from the front axle.

The unloaded vehicle (507 grams) was taken as an example. From the measurements of F_A (2.65 N) and F_B (2.32 N), F_{CG} was calculated as 4.97 N from equation (12) since F_C was zero. Introducing F_A (2.65 N), F_B (2.32 N) and F_{CG} (4.97 N), as well as $F_C = 0$ and $c = 0$ into Equations (13) and (14), the distance *a* was calculated as 14.0 cm. After rear loading, the CG position was shifted rearward to 11 cm, which led to a greater than 20% speed increase (**Table 1**).

The height of the unloaded vehicle was 73 cm, so the height of the rear-loaded vehicle was 81 cm. Since *m* is approximately equal to *M* in Equation (5), the speed was approximated as 3.12 m/s for the unloaded vehicle by introducing the height of 73 cm. Similarly, the approximate speed of rear-loaded vehicle was found to be 3.25 m/s by introducing the height of 81 cm. Compared to the theoretical calculations, the experimental data, 2.39 m/s (unloaded) and 3.00 m/s (867 grams, rear loading) are smaller due to energy loss (**Table 1**). The larger speed difference between 2.39 m/s and 3.00 m/s and accuracy difference between 20.4 m-1 and 38.5 m^{-1} exemplified that the rearward shift of the CG position greatly improved the vehicle's performance.

ACKNOWLEDGEMENTS

We would like to express our heartfelt gratitude to Mr. Donald Terek, a retired engineer, for his help during the construction of the gravity vehicle device. We would also like to thank Mr. Mike Farrell, who allowed us to use the gym facilities at California State University, Fullerton for experimental studies.

Received: October 5, 2020
Accepted: December 11, 2020
Published: March 16, 2021

REFERENCES

1. Mazumder, H., *et al*. "Performance Analysis of EV for Different Mass Distributions to Ensure Safe Handling." Energy Procedia, vol. 14, Dec. 2012, pp. 949-954., doi:10.1016/j.egypro.2011.12.1038.
2. Rievaj, V., *et al*. "The Effects of Vehicle Load on Driving Characteristics." Advances in Science and Technology Research Journal, vol. 12, no. 1, Mar. 2018, pp. 142-149. doi: 10.12913/22998624/80896.
3. Skrucany, T., *et al*. "Impact of Cargo Distribution on the Vehicle Flatback on Braking Distance in Road Freight Transport." MATEC Web of Conferences, 18th International Scientific Conference-LOGI, vol. 134, 2017, pp. 54. doi: 10.1051/matecconf/201713400054.

4. Skrucany, T., *et al*. "The Influence of the Cargo weight and its Position on the Braking Characteristics of Light Commercial Vehicles." Open Engineering. vol. 10, no. 1, Feb. 2020, pp. 154-165., doi: 10.515/eng-2020-0024.
5. Mehmet, A., *et al*. "Method for Determining the Centre of Gravity for an Automotive Vehicle." WO 2007/098891A1. https://patents.google.com/patent/WO2007098891A1/en.
6. Lee, J. H., *et al*. "Real-time Longitudinal Location Estimation of Vehicle Center of Gravity." International Journal of Automotive Technology, vol. 19, no. 4, Jun. 2018, pp. 651-658.
7. Science Olympiad Division C Rules Manual. Gravity Vehicle, 2020, pp. 30-32. http://api-static.ctlglobalsolutions.com/science/Science_Olympiad_Div_C_2020_Rules_Manual_Web.pdf.
8. Yutaka Nishiyama "The Brachistochrone Curve: The Problem of Quickest Descent." International Journal of Pure and Applied Mathematics, vol. 82, no. 3, Sep. 2013, pp. 409-419. https://ijpam.eu/contents/2013-82-3/8/8.pdf
9. Krishna, K. R., *et al*. "Kinetic Energy Storage and Recovery System using Torsion Spring." International Journal of Engineering Research & Technology, vol 3, no. 22, 2015, pp. 1-4, Special Issue. www.ijert.org/research/kinetic-energy-storage-and-recovery-system-using-torsion-spring-IJERTCONV3IS22029.pdf.
10. 3D CAD Design Software, Dassault Systems Solidworks Student Edition, 2019.
11. Patel, S. G., *et al*. "Measuring a Centre of Gravity of an Object using 4 Load Transducer Method." International Journal for Innovative Research in Science & Technology, vol. 6, no. 1, Jan. 2017, pp. 210-214., doi:10.17577/IJERTV6IS010100.

JOURNAL OF
EMERGING INVESTIGATORS

Article

The effect of the consumption of the probiotic *B. infantis* on ethanol withdrawal symptoms in planaria (*Dugesia dorotocephala*)

Marissa McCandless and Janine Cupo
Seaford High School, Seaford, New York

SUMMARY

Alcohol use disorder is a chronic, relapsing disease that affects millions of Americans every day. There are limited treatment options for alcohol dependence and alcohol withdrawal symptoms, including depression and anxiety. Previous studies have shown that probiotics can decrease depression in rodents during maternal separation and anxiety in humans. Therefore, we hypothesized that the ethanol-withdrawn planaria who consumed probiotics would have decreased withdrawal symptoms as measured by increased motility compared to the ethanol-withdrawn planaria that were not fed probiotics. The ethanol-withdrawn planaria had a statistically significant decrease in motility compared to the control group, while the planaria that consumed probiotics had no statistically significant change in motility compared to the control group. We determined that there was a statistically significant difference between the ethanol and probiotics-treated group and the control group. Additionally, there was a statistically significant difference between the ethanol and probiotics-treated group and the ethanol-withdrawn group, confirming our hypothesis. Although the results indicated that the consumption of probiotics were unable to significantly counteract the effects of ethanol withdrawal symptoms in planaria, the probiotics significantly increased the ethanol-withdrawn planaria's motility as compared to the ethanol-withdrawn group that was not given probiotics. Given these results, probiotics have the potential to reduce the symptoms of alcohol withdrawal in humans.

INTRODUCTION

Alcohol use disorder (AUD), a chronic, relapsing disease characterized by compulsive alcohol consumption, is an unceasing issue that affects many Americans. About 19.7 million American adults lived with a substance use disorder in 2017, with 74% of these adults living specifically with alcohol use disorder (1). Treatment for AUD is difficult because of the lengthy withdrawal process. Withdrawal is defined as behavior that occurs when ceasing to use an addictive substance. Due to the symptoms that can coincide with alcohol withdrawal, such as depression and anxiety, people often relapse and return to abusing alcohol. Depression and anxiety are disorders that result from an imbalance of neurotransmitters in the brain such as serotonin, dopamine and norepinephrine (2). These neurotransmitters are responsible for initiating nerve impulses through the brain, promoting feelings such as happiness and pleasure. Severe depression and anxiety are often caused by a failure in the neurotransmitter system and are commonly treated with an antidepressant drug. However, if a person is addicted to or withdrawing from alcohol, taking an antidepressant could be dangerous for both their mental and physical state because alcohol can worsen the side effects of an antidepressant, and the antidepressant can exacerbate the effects of alcohol consumption (3). In order to reduce the prevalence of AUD, new treatments must be developed to treat alcohol withdrawal symptoms.

A potential solution is utilizing probiotics as a treatment for the symptoms of depression and anxiety. Probiotics are microorganisms that are introduced into the body to aid in the function of the gut microbiome. The gut microbiome is the community of beneficial microorganisms living in the intestines that help with daily bodily functions (4). The Food and Agriculture Organization and the World Health Organization have defined probiotics as live bacterium that are beneficial for supplementing the body's gut microbiome and its functions (5). Probiotics may serve as a viable treatment for alcohol withdrawal due to the interaction between the gut microbiome and the brain, known as the gut-brain axis (Figure 1). The central nervous system (CNS) and the enteric nervous system (ENS) are communication systems that make up the gut-brain axis (6). The gut-brain axis accounts for how the bacterial communities in the gut microbiome affect mental processes in the brain and vice versa (6). Therefore, the connection between probiotics and ethanol withdrawal symptoms can be made based on previous research that indicated there is a connection between the gut microbiome, where probiotics are found, and the brain, where the symptoms depression and anxiety stem from (6).

Like humans, planaria have a gut microbiome that affects many of their bodily functions. Planaria are free-living flatworms that can be found in either spring or saltwater ponds and rivers. Planaria are ideal organisms to experiment with because they present little ethical concerns and are known to experience the effects of a drug similar to the experience of humans (7, 8). Multiple studies have been conducted showing that planaria who consume drugs such as ethanol, nicotine and sucrose develop withdrawal symptoms (7, 8, 9). Additionally, planaria have simple nervous and digestive

systems that are relatively easy to analyze. The planaria nervous system is organized with axons and dendrites and contains multipolar nerve cells, which are similar to the organization of a human's nervous system (10). Not only do they have a similar structure, but planaria also have many of the same neurotransmitters as humans, such as serotonin and norepinephrine (10, 11). These neurotransmitters impact human depression and anxiety and may affect planaria in a similar way. Furthermore, planaria have a digestive system that is analogous to the human digestive system; the planaria's gut microbiome is comprised of multiple bacteria populations that are also found in a human's gut microbiome (12). These similarities make the drug effects that planaria experience comparable to the effects that humans experience.

The goal of this study was to asses a connection between relief from alcohol withdrawal symptoms and the consumption of probiotics. If probiotics were found to be effective in reducing anxiety and depression in planaria, they could be further studied as an aid for people experiencing the ethanol withdrawal process. Therefore, we asked whether the consumption of *Bifidobacterium infantis* will reduce the symptoms of ethanol withdrawal in planaria (*Dugesia dorotocephala*). The specific bacterial strain, *Bifidobacterium infantis*, was utilized since previous studies have shown its effectiveness in reducing depression and anxiety (6, 13). Ethanol, the alcohol found in alcoholic beverages, is frequently used for experiments involving planaria addiction and withdrawal. Therefore, we placed planaria in ethanol for 24 hours and then removed them and placed them immediately in spring water (7, 14). To study symptoms of depression and anxiety in planaria, we used a line crossing

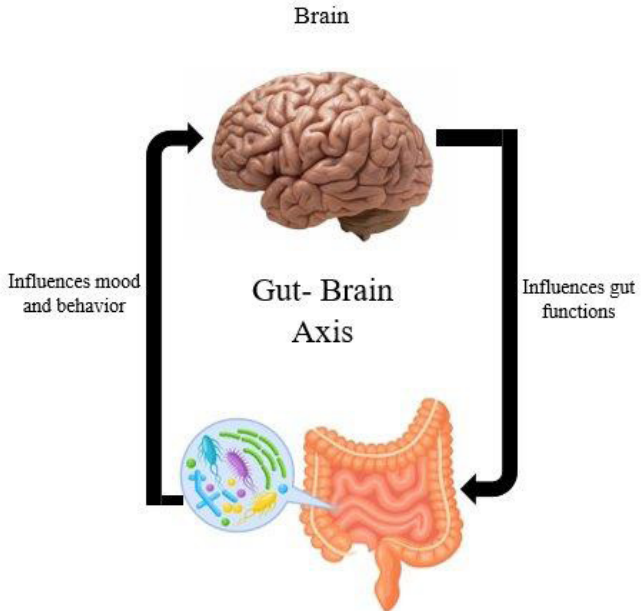

Figure 1: Gut-Brain Axis. The interaction between the gut microbiome and the brain demonstrating the influence of the gut microbiome on mood and behavior.

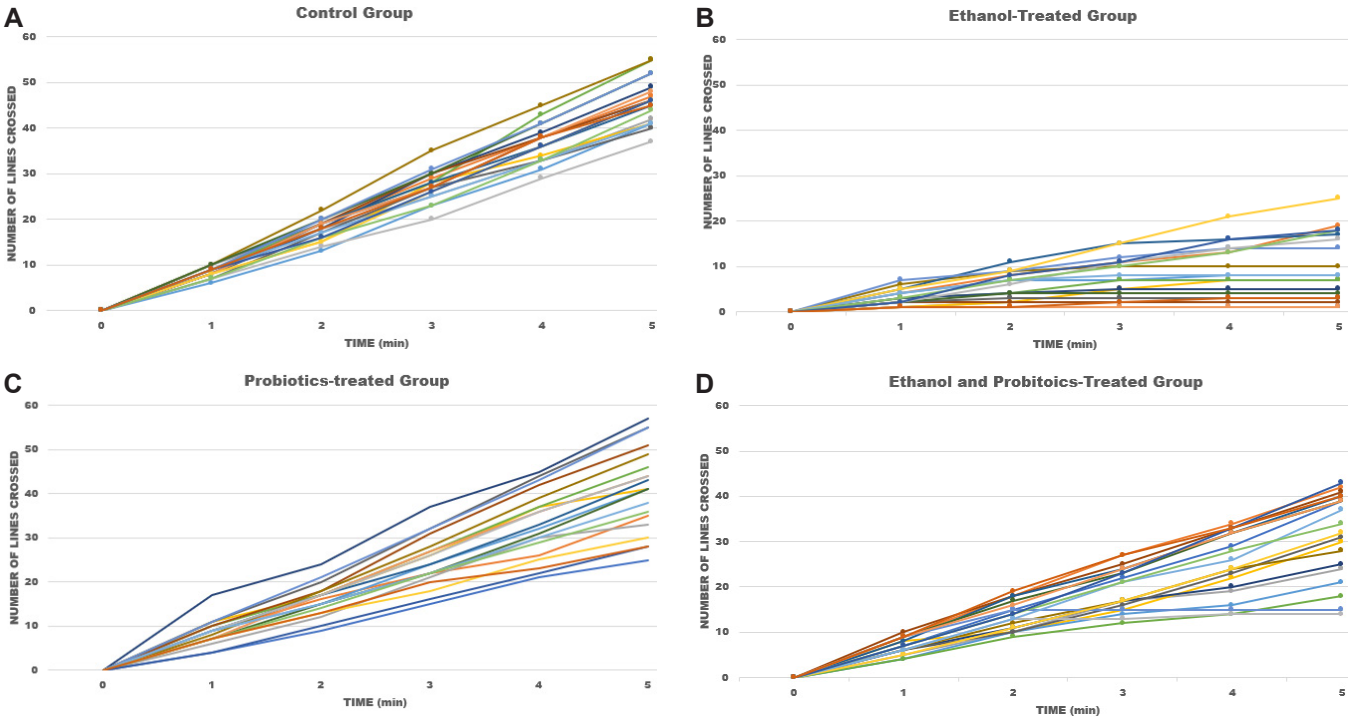

Figure 2: Cumulative number of lines crossed for each individual trial under four different conditions. A: Number of lines crossed per planaria across a five minute period for control group. B: Number of lines crossed per planaria across a five minute period for ethanol-treated group, C: Number of lines crossed per planaria across a five minute period for probiotics-treated group, D: Number of lines crossed per planaria across a five minute period for ethanol and probiotics-treated group (each line of the graph represent a planaria)

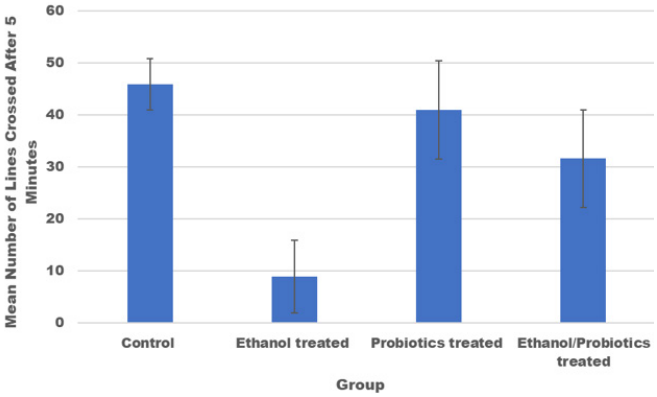

Figure 3. Mean number of lines crossed in five minutes during line crossing assay to determine motility. Error bars represent the standard deviation.

assay, that measures motility in planaria and has been validated by previous research (7, 14). We hypothesized that the ethanol-withdrawn planaria who consumed probiotics would have decreased withdrawal symptoms as measured by increased motility compared to the ethanol-withdrawn planaria that were not fed probiotics. We found that probiotic consumption was effective in diminishing ethanol withdrawal symptoms in the planaria. However, probiotics did not restore the planaria to their normal behavior.

RESULTS

To determine whether consumption of probiotics would be successful in reducing the effects of ethanol withdrawal, planaria were treated with ethanol for 24 hours after being fed probiotics in their food. Then, line crossing assays were conducted to quantify planaria motility as measured by the number of lines crossed by the planaria in five consecutive minutes (7, 9). Reduced planaria motility is reflective of depression and anxiety induced by ethanol withdrawal in planaria and has been demonstrated as an effective way to measure planaria withdrawal from a substance (7, 14, 15).
During the five minutes of each line crossing assay, the cumulative number of lines crossed were recorded for each individual trial (Figure 2). Then, the means and standard deviations were determined (Figure 3). The average number of lines crossed by the control group was 45.9, by the ethanol-treated group was 8.9, by the probiotics-treated group was 41 and by the ethanol and probiotics-treated group was 31.6 (Figure 3). The R^2-value (correlation coefficient), which represents the linear relationship amongst the data, was found for each group (Table 1).

We performed a one-way ANOVA (Table 2) {F(3,76)=85.95, p=2.33E-24}. These ANOVA results suggest that there was a statistically significant difference among the data from each treatment group. We conducted a Tukey HSD post-hoc test following the ANOVA to see where the differences within the data lie. The p-values for comparing the control and ethanol-treated group (p=0.001), the control group and the experimental group (p=0.001), and the ethanol-treated group and the experimental group (p=0.001) were all less than 0.01, indicating that there was a statistically significant difference among the data from those groups. The p-value (p=0.213) between the control group and the probiotics-treated group was greater than 0.01, indicating no statistically significant difference among the data in those groups.

	R^2-Values			
Planaria Number	Control	Ethanol-treated	Probiotics-treated	Ethanol/Probiotics-treated
1	0.999	0.429	0.996	0.997
2	0.999	0.984	0.988	0.998
3	0.998	0.690	0.987	0.987
4	0.990	0.946	0.989	0.975
5	0.993	0.783	0.998	0.985
6	0.991	0.864	0.998	0.985
7	0.998	0.757	0.989	0.992
8	0.996	0.428	0.997	0.998
9	0.993	0.631	0.998	0.989
10	0.998	0.713	0.998	0.997
11	0.998	0.911	0.997	0.997
12	0.999	0.690	0.996	0.998
13	0.999	0.881	0.999	0.659
14	0.998	0.429	0.998	0.999
15	0.997	0.983	0.999	0.760
16	0.995	0.996	0.998	0.994
17	0.999	0.760	0.998	0.991
18	0.994	0.994	0.100	0.999
19	0.997	0.983	0.997	0.993
20	0.998	0.943	0.986	0.992
Mean	0.997	0.790	0.995	0.964

Table 1: R^2 values for Line Crossing Assays.

DISCUSSION

The R^2-values in Table 1 indicated that there was a linear relationship between the number of lines crossed and time. Planaria have been shown to exhibit exploratory behavior when placed in a novel environment. Since they are mainly nocturnal, once removed from their preferred environment and placed in a new petri dish in a well-lit area, their nearly linear behavior may be due to the planaria's inherent exploratory behavior. The R^2-values indicated that all groups continued to exhibit relatively constant exploratory behavior, thereby allowing motility to be observed and assayed. It is possible that, given more time, the curves would have flattened as the planaria eventually acclimated to their environment.

The results from the ANOVA test {F(3,76)=85.95, p=2.33E-24} indicated that there was a statistically significant difference amongst the data. The Tukey HSD post-hoc test provided p-values and determinations for the differences among the groups. The statistically significant p-value (p=0.001) for the control group and ethanol-withdrawn group signified that the number of lines crossed in the ethanol-

ANOVA						
Source of Variation	SS	df	MS	F	p-value	F crit
Between Groups	16157.8	3	5385.933	85.95056	2.33E-24	2.724944
Within Groups	4762.4	76	62.66316			
Total	20920.2	79				

Table 2. One-Way ANOVA Results.

Treatment Pair	Tukey HSD p-value	Tukey HSD inference
Control vs. Ethanol-treated	0.001	**p<0.01
Control vs. Probiotics-treated	0.213	Not significant
Control vs. Ethanol/ Probiotics-treated	0.001	**p<0.01
Ethanol-treated vs. Ethanol/Probiotics-treated	0.001	**p<0.01

Table 3. Tukey HSD Post-Hoc Results (** indicates significant difference).

withdrawn group was significantly less than the number of lines crossed in the control group. Thus, the planaria experienced the symptoms of withdrawal, depression and anxiety, from the 0.5% ethanol solution, as decreased motility is indicative of these symptoms. These results agreed with previous studies that demonstrated that planaria can experience withdrawal symptoms from this ethanol concentration (7). The Tukey HSD post-hoc test determined that the p-value (p=0.231) from the control and probiotics-treated groups was statistically insignificant, denoting that there was no statistically significant difference between the number of lines crossed in those groups. As a result, we concluded that the $6.67x10^6$ CFU/mL probiotic solution did not have an impact on planaria motility. The statistically significant p-value of 0.001 between the control group and the ethanol and probiotics-treated group demonstrated a significant difference among those groups, indicating that the probiotics were unable to completely reverse the effects of ethanol withdrawal. However, the p-value (p=0.001) between the ethanol-treated group and the ethanol and probiotics-treated group denoted a statistically significant difference between those groups, indicating that the probiotic was effective in increasing the number of lines crossed by the ethanol withdrawn planaria. The probiotic was therefore effective in reducing the symptoms of depression and anxiety in this study. After coming to these conclusions, we failed to reject the hypothesis that the ethanol-withdrawn planaria who consumed probiotics would have decreased withdrawal symptoms as measured by increased motility compared to the ethanol withdrawn planaria that were not fed probiotics.

The results support our hypothesis and offer a new understanding of the benefits of probiotics. Previous studies have shown that probiotics are useful in enhancing the gut microbiome function, in reducing inflammation, which is linked to decreased anxiety, and in decreasing the effects of depression (6, 13). The results of this experiment suggest that probiotics may be a treatment for the ethanol withdrawal symptoms of depression and anxiety as well.

The implications of this study are plentiful. Since probiotics can potentially aid in the alcohol withdrawal process, they may also diminish the occurrence of AUD. Likewise, since the symptoms of withdrawal include depression and anxiety, probiotics could potentially serve as a treatment for these disorders and as a substitute for antidepressants. There are a multitude of possibilities for probiotics in the future, and if research in this field continues to progress, probiotics may be able to solve many health issues that the world is facing today.

MATERIALS AND METHODS

Dugesia dorotocephala (planaria) were obtained from the Carolina Biological Supply Company. The planaria were cared for in a home jar containing Poland Spring water since their natural habitat is spring ponds and rivers (16). This water was changed three times a week and the planaria were fed chicken liver once a week. Many researchers feed planaria chicken liver as their main source of nutrition due to its protein (16). We made ethanol solutions (0.5%) from 70% ethanol obtained from Carolina Biological Supply. Planaria were treated with powder from probiotic pills of Bifidobacterium infantis 35624 ($1x10^9$ colony forming units), from Alforex. Colony forming units (CFU) is the unit used in the scientific community to measure the viable bacteria in a given sample.

First, the planaria were separated into four groups to distinguish between the variables being tested. Each group had twenty planaria and each planaria was considered one trial, equating to twenty trials per group. All planaria were maintained at the same environmental conditions and fed on the same days at the same time, with the only difference being that the probiotics-treated group and the experimental group were fed probiotic soaked chicken liver. The negative control group contained planaria that represented normal planaria behavior, and the results from this group were compared against the rest of the groups' results. The first positive control group was the planaria that were treated with a 0.5% ethanol solution to demonstrate that the ethanol solution caused withdrawal symptoms in the planaria. In the second positive control group, the planaria were fed the probiotic solution to demonstrate that the probiotics did not have adverse effects on the planaria. Finally, the experimental group contained planaria that were fed the probiotics and then exposed to the ethanol solution, to determine whether the probiotics were successful in diminishing the effects of the ethanol withdrawal symptoms of depression and anxiety. The temperature, humidity and light conditions remained the same for all groups.

The ethanol solution was prepared by calculating the amount of Poland Spring water and ethanol in milliliters that was necessary to create a 0.5% concentration of ethanol by mass. When planaria are removed from this specific concentration of ethanol, previous studies have indicated that they experience withdrawal symptoms (7, 8). Before each trial for the probiotics-treated group and the ethanol and probiotics-treated group, the probiotic solution was created by breaking apart the pill's protein capsule, pouring the

probiotic powder into 150 milliliters of Poland Spring water, and creating a suspended solution by using a magnetic stirrer. The final probiotic solution consisted of $6.67x10^6$ CFU per milliliter of water. The $6.67x10^6$ CFU/mL concentration was the only solution that was found to have no detrimental effects on planaria motility, after testing the planaria with varying concentrations of probiotics. Additionally, before each trial in these groups, a 0.1-gram piece of chicken liver was soaked in the suspended probiotic solution for five minutes and then fed to the planaria for three hours, which is their normal feeding time (17). In using this method, the planaria were treated with the probiotics through ingestion, similar to how humans take probiotics.

Line Crossing Assay

To conduct a line crossing assay, a planaria is placed in a petri dish containing Poland Spring water which was placed on one-inch grid lined paper. The number of lines crossed by the planaria in five consecutive minutes is recorded (9). Decreased motility is characterized when a planaria crossed fewer lines as compared to the control group which indicates depression and anxiety in the planaria.

Control Group

A planaria was randomly selected from the home jar and placed into a petri dish consisting of Poland spring water. The petri dish was then placed back into a dark cabinet for 24 hours since planaria prefer a dark environment. After 24 hours, the planaria was then moved into a different petri dish and a line crossing assay was performed.

Ethanol-withdrawn Group

A planaria was randomly selected from the home jar and placed into a petri dish consisting of the ethanol solution (0.5%) and the petri dish was then placed back into a dark cabinet for 24 hours. After these 24 hours, when the planaria became addicted to the ethanol, the planaria was removed from the ethanol solution, placed in a new petri dish with Poland spring water and the line crossing assay was conducted.

Probiotics-treated Group

First, the probiotic soaked chicken liver was fed to five planaria, randomly selected from the home jar, in a petri dish filled with Poland Spring water. Five planaria were chosen in order to speed up this process as this group had a lengthy procedure. The chicken liver was removed after the standard amount of time the planaria are given to eat (approximately three hours). The planaria were then placed into separate petri dishes containing Poland Spring water and placed in a cabinet for 24 hours. After the 24 hours, the planaria were moved into new petri dishes containing Poland Spring water and the line crossing assay was performed.

Ethanol and Probiotics-treated Group

Five planaria were randomly selected from the home jar and placed into petri dishes containing the probiotic soaked chicken liver. After being allotted the standard amount of time to feed, the planaria were placed in individual petri dishes containing the 0.5% ethanol solution. The planaria were left in a cabinet in the ethanol solution for 24 hours, and then removed and placed into new petri dishes containing Poland Spring water for the line crossing assay.

Data Analysis

Statistical analyses of the line crossing assay data were conducted using Microsoft Excel to determine means, standard deviations, R2-values and p-values. A one-way ANOVA test was performed to determine the F-value, degrees of freedom between groups and within groups, and a p-value for all the group comparisons. A p-value corresponding to an F-statistic lower than 0.05 would suggest that there is a significant difference among one or more of the treatment groups and a post-hoc test would be performed. A Tukey HSD post-hoc test was performed, since the p-value corresponded to the F-statistic, to determine where the differences lie within the data. P-values were determined from this test and if the values were less than 0.05, there was a statistically significant difference between the groups.

ACKNOWLEDGMENTS

We would like to acknowledge and thank Mary Simons and Richard Kurtz for their mentorship and as well as Journal of Emerging Investigators Editors who provided guidance along this process.

REFERENCES

1. American Addiction Centers. Alcohol and Drug Abuse Statistics. 2020.
2. Harvard Health Publishing. What Causes Depression? 2019.
3. Windward Way. Alcohol and Antidepressants: A Dangerous Mix. 2018.
4. Lederberg, J., & McCray, A.T. 'Ome Sweet `Omics--A Genealogical Treasury of Words. The Scientist, 15(7), 2001, 8.
5. Dogan, M., Tekiner, I.H., & DemirkesenBicak, H. Chapter 13- Probiotics From Food Products and Gastrointestinal Health. Dietary Interventions in Gastrointestianal Diseases, 2019, 169-177.
6. Sauliner, D.M., Ringel, Y., Heyman, M.B., Foster, J.A., Bercik, P., Shulman, R.J., Versalovic, J., Verdu, E.F., Dinan, T.G., Hecht, G. & Guarner, F. The intestinal microbiome, probiotics and prebiotics in neurogastroenterology. Gut Microbes, 2013, 1-21.
7. Francis, K.S. Planaria as a model for the effects of the co-use of alcohol and nicotine. 2015.
8. Tallarida C.S., Bires K., Avershal J., Tallarida R.J., Seo, S., & Rawls, S.M. Ethanol and cocaine: environmental place conditioning, stereotypy and synergism in

planarians. Alcohol, 48, 2014, 579-586.
9. Zhang, C., Tallarida, C.S., Raffa, R.B. & Rawls, S.M. Sucrose produces withdrawal and dopamine-sensitive reinforcing effects in planarians. Physiology & Behavior, 112, 2013, 8-13.
10. Sarnat, H.B., & Netsky, M.G. The Brain of the Planaria as the Ancestor of the Human Brain. The Canadian Journal of Nuerological Sciences, 12, 1985, 296-302.
11. Raffa, R.B., Gallo, D.A., Tallarida, C.S., Rawls, S.M., & Tallarida R.J. Isobolographic Method and Invertebrate (Planarian) Model for Evaluating Combinations of Waterways Pollutants. Pharmacology & Pharmacy, 3, 2012, 381-387.
12. Arnold, C.P., Merryman, M.S., Harris-Arnold, A., McKinney, S.A., Seidel, C.W., Loethen, S., Proctor, K.N., Guo, L. & Sanchez-Alvarado, A. Pathogenic shifts in endogenous microbiota impede tissue regeneration via distinct activation of TAK1/MKK/p38. Stem Cells and Regenerative Medicine, Microbiology and Infectious Disease, 2016.
13. Desbonnet, L., Garrett, L., Clarke, G., Kiely, B., Cryan, J.F., & Dinan, T.G. Effects of the probiotic Bifidobacterium infantis in the maternal separation model of depression. Neuroscience, 170, 2010, 1179-1188.
14. Sacavage, S., Patel, H., Zielinski, M., Acker, J., Phillips, A.G., Raffa, R.B., & Rawls, S.M. Withdrawal-like behavior in planarians is dependent on drug exposure duration. Neuoscience Letter, 439, 2008.
15. Raffa, R.D., & Valdez, J.M. Cocaine withdrawal in planaria. European journal of pharmacology, 430, 2001, 143-5.
16. Carolina Biological Supply Company. Living Care Information. 2020.
17. Fujita, A., Sarkar, D., Wu, S., Kennelly E., Shetty K., & Genovese Ines, M. Evaluation of phenolic-linked bioactives of camu-camu (Myrciaria dubia Mc. Vaugh) for anithyperglycemia, antihypertension, antimicrobial properties and cellular rejuvenation. Food Research International, 77, 2015, 194-203.

Article submitted: June 18, 2020
Article accepted: July 27, 2020
Article published: February 20, 2021

JOURNAL OF
EMERGING INVESTIGATORS

Article

Monitoring the formation of polyurethane foams with an infrared camera: Classroom activity

Napat Kerewanmas[1,†], Natthanan Kongchu[1,†], Thanit Pewnim[1], Janjira Maneesan[1*], Ratchapol Jenjob[2*], and Daniel Crespy[2]

[1] Kamnoetvidya Science Academy (KVIS), Rayong 21210, Thailand

[2] Department of Materials Science and Engineering, School of Molecular Science and Engineering, Vidyasirimedhi Institute of Science and Technology (VISTEC), Rayong 21210, Thailand

[†] The authors contributed equally

SUMMARY

Foams prepared with polyurethanes (PU), a polymer with units in the main chain joined by urethane linkages, are commonly used in isolation panels, seals, automative seats, and bedding. The reaction causing the formation of polyurethane foams is a conventional, yet spectacular, way to attract the attention of polymer chemistry students. Infrared cameras are a relatively inexpensive apparatus that allow for semi-quantitatively temperature monitoring at the surface of objects. Because the formation of polyurethane is exothermic, the polymerization reaction and the expansion of the foam can be easily detected by an infrared camera. Information such as volume expansion, maximum temperature, temperature distribution in time and space, and reaction time can be retrieved from short videos. These data can be correlated and discussed in relationship with the reactivity of the components for synthesizing the foam. The primary goal of this activity was to investigate the exothermic reaction of polyurethane foam using an infrared camera which has been successfully used for monitoring the exothermic formation of polyurethane foams. These values can be discussed in term of reactivity of isocyanates (aromatic and aliphatic/cycloaliphatic) for a given formulation of polyols. The highly visual content of such experiments is attractive for children and students. Chemicals for performing the experiments can be donated either individually or as ready sets ("polyols") from the industry. It is anticipated that the investment required for buying the infrared camera can be redeemed by using it for other types of exo- or endothermic reactions and for teaching heat transfer in physics class.

INTRODUCTION

Due to their low density, low thermal conductivity, and mechanical properties, polyurethane (PU) foams have a remarkably broad range of applications including thermal and sound insulation, structural and comfort materials, cushioning, buoyancy, energy absorption (packaging), and aircraft-interior panels (1). PU foams are usually produced by the exothermic addition polymerization between isocyanate groups and polyols that form urethane linkages, called gelling reaction (1). This reaction is carried out at room temperature with catalysts such as tertiary amine and tin compounds (**Figure 1C**). Moreover, water is used as a blowing agent to generate carbon dioxide (CO_2) gas by reacting with molecules containing isocyanate (-N=C=O) groups in a highly exothermic process (**Figure 1D**) (2-3). CO_2 gas forms bubbles inside the reactive mixture, which are stabilized by surfactants (surface active molecules) (4).

The microstructure and morphology of foam depends on many factors, such as the competition between gelling and blowing reactions, mobility of urethane and urea groups, crosslinking density, and specific interactions between polyols and polyurethane segments (5-6). The PU foams are generally classified as rigid, semi-rigid, or flexible, depending on their mechanical properties and core densities (7). Various grades of PU foams can be manufactured by tuning and controlling nature and properties of the starting materials (isocyanates and polyols) (3). The formation of foams is very popular in chemistry teaching classes, despite the toxicity of isocyanates (8), because of the fast and large expansion of foams, which makes the reaction very impressive. Other experiments related to the preparation and measurements of the density of foams were designed for students dealing with their second-year laboratory projects (9). Moreover, polymer foams were produced in at least 1000 secondary schools in Scotland in order to raise the interest of children in chemistry (10). Herein, we combine the preparation of polyurethane foams with another visual detection method to monitor the temperature of the reaction. The advantage of measurements using an infrared camera is that they provide a colourful real-time monitoring of the foaming process while giving quantitative data related to temperatures of the foams.

Generally, temperature is measured by thermometers, thermocouples, thermistors, and resistance temperature detectors that determine the temperature at explicit points and need to be in contact with the measured objects (11). Conversely, infrared thermal imaging (ITI) is a noncontact tool, which maps the temperature distribution of objects with fast response times (12). Thermal imaging technique converts the invisible radiation pattern of an object into visible images. It generates coloured images that represent different temperatures. Originally, ITI was developed for military use, however, over the past two decades, it has become available for non-military purposes (12). ITI can be applied in all applications where temperature differences are required to support diagnosis, evaluation, or analysis of objects. Thus, it has revolutionized the concept of temperature measurement

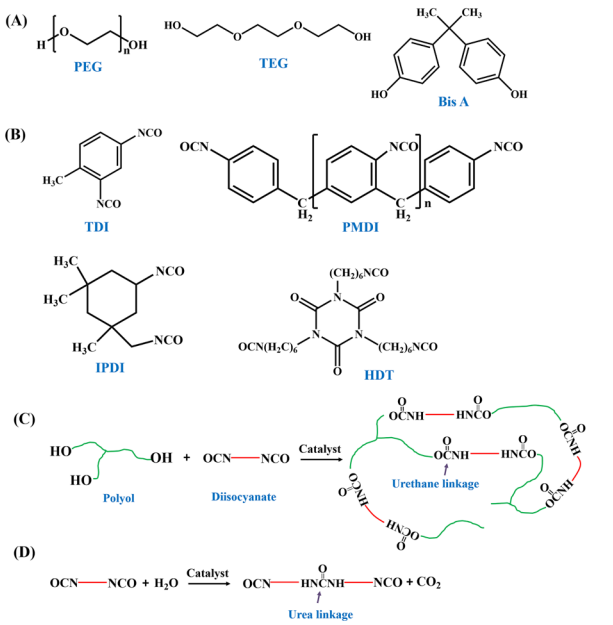

Figure 1: Chemical structures of polyols (A) and isocyanates (B). Polyurethane foams are formed via a gelling reaction between polyols and diisocyanates to obtain urethane linkages (C) and a blowing reaction between diisocyanates and water to yield urea linkages and carbon dioxide (D).

in a wide range of scientific real time problems in industry (13), agriculture (14-15), and medical applications (16-17).

Recently, ITI was applied to measure the temperature produced in chemical reactions (12,18-19). Infrared camera was also used for teaching heat transfer by conduction, convection, and radiation (20-23). Furthermore, it was introduced as tool for teaching first year undergraduates for monitoring heat of solutions, crystallization, and differences of vapor pressure (24). In this study, students monitored the exothermic formation of PU foams with an infrared camera from different types of isocyanates. Polyurethane foams were manufactured by the reaction of polyol mixture (**Figure 1A**) with isocyanates in the presence of catalysts (TEA and DBTDL), surfactant (SDS), and blowing agents (DCM and H_2O). The selected isocyanates were either aromatic (tolylene 2,4-diisocyanate, TDI, or polymeric methylene diphenyl diisocyanate, PMDI) or aliphatic/cycloaliphatic (isophorone diisocyanate, IPDI, or tolonate HDT, HDT) isocyanates. We hypothesized that aromatic isocyanates would show a higher reactivity than aliphatic/cycloaliphatic isocyanates (25) due to their aromatic electron withdrawing substituents (26). Thus, the foam produced by aromatic isocyanates would show larger heat generation, which should be detected by the infrared camera. The reactivity of isocyanates should also influence the volume expansion and morphology of the produced foams. We found that the infrared camera can be used to monitor the exothermic formation of polyurethane foams to detect the differences resulting from the isocyanates used. The findings can be used for teaching chemistry to students.

RESULTS

We fixed the amounts of polyols, crosslinkers, surfactants, catalysts, and blowing agents but calculated the amounts of isocyanates so that molar ratios between isocyanate groups and hydroxyl groups were equal (**Table 2**). Additionally, we used various isocyanates to prepare the PU foams. To observe the evolution of the temperature during the reactions we utilized an infrared camera. Videos recorded with the infrared camera are available in Supporting Information. As shown in **Figure 2A**, the foam prepared with an aromatic isocyanate such as TDI showed larger heat generation and even caused distortion of the plastic container. Note that the distortion of the cup occurs in a non-reproducible manner and therefore impairs the accuracy of the data extracted from this experiment. Moreover, the foaming process was completed within 19 s with a maximum temperature of 124°C (T_{max}) measured by infrared camera (**Table 1**). Noticeably, heat generation from foams formed with TDI was larger than heat prepared with PMDI due to the low viscosity and hence larger mobility of TDI and its reaction rate in the mixture. Conversely, we observed a longer reaction time (**Table 1**) for foams prepared with aliphatic/cycloaliphatic isocyanates (IPDI, HDT, and mixture of HDT and IPDI), suggesting a slower reaction rate compared to aromatic isocyanates. Moreover, the foam prepared with HDT (cycloaliphatic isocyanate) displayed the longest reaction time (~110 s), probably due to the high viscosity of the chemical. After mixing of HDT with IPDI, the reaction time decreased to ~55 s, due to the lower viscosity of the mixture. The dichloromethane:water (DCM:water) ratio was reduced from 8:1 (PU3) to 2:1 (PU6) using IPDI as isocyanate, while the amounts of polyols, surfactant, water (0.1 g) and catalyst were kept constant (**Table 1**). Interestingly, a decreasing amount of DCM affected the heat generation, rate of reaction, and volume expansion of the foam. Whereas time at T_{max} and time to maximum height increased, the

Entry	Isocyanate	T_{max} [°C]	Time at T_{max} [s]	Time to max. height [s]	Volume expansion [fold]
PU1	TDI	124 ± 7	19.0 ± 2.8	2.3 ± 0.5	1.6 ± 0.2
PU2	PMDI	91 ± 5	35.7 ± 9.5	9.7 ± 2.9	2.3 ± 0.1
PU3	IPDI	109 ± 1	71.0 ± 5.7	96.7 ± 2.5	2.9 ± 0.5
PU4	HDT	95 ± 5	110 ± 47	88 ± 26	2.3 ± 0.3
PU5	HDT + IPDI	104 ± 1	55 ± 4	55 ± 3	3.1 ± 0.3
PU6	IPDI	93 ± 10	179 ± 28	189 ± 24	2.5 ± 0.1

Table 1: Maximum temperature T_{max}, time at T_{max}, time to reach maximum height, and volume expansion detected with an infrared camera during the preparation of foams with various isocyanates.

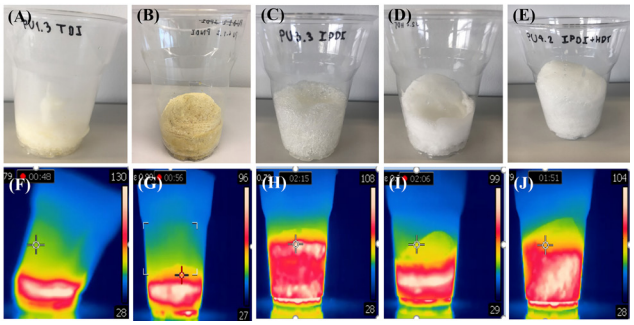

Figure 2: Photographs (A-E) and infrared thermal images (F-J) of PU foams prepared with TDI (A,F), PMDI (B,G), IPDI (C,H), HDT (D,I), and IPDI+HDT (E,J).

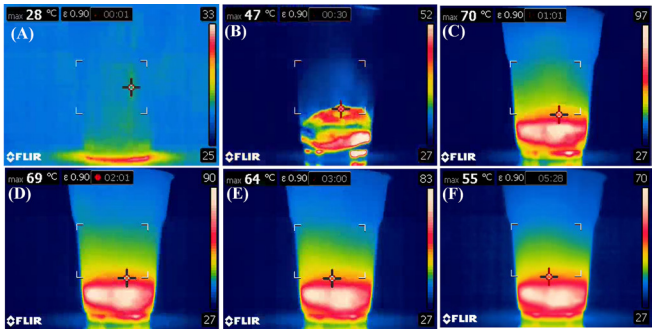

Figure 3: Infrared thermal images of PU foams prepared with IPDI+HDT at various time intervals: 1 s (A), 30 s (B), 60 s (C), 120 s (D), 180 s (E), and 328 s (F).

volume expansion of foam was reduced when less DCM was used in the formulation (see **Table 1**). As the amount of DCM decreased, the vapor pressure decreased, leading to foams with a lower volume expansion.

We easily visualized temperature gradients via a colour gradient from blue (cold) to white (hot) on infrared thermal images (**Figure 2**). Foams produced from aromatic isocyanates (TDI and PMDI, **Figure 2F-G**) showed less volume expansion than foams produced with aliphatic or cycloaliphatic isocyanates (IPDI and HDT, **Figure 2H-I**). The maximum volume expansion (~3.1-fold) was obtained from mixture of IPDI and HDT (**Table 1**).

Due to its large volume expansion, we selected the foam prepared from mixture of IPDI and HDT to study the effect of reaction time on the reaction temperature. The reaction for producing PU foams can be monitored in time as shown in **Figure 3**. The temperature reached almost 100˚C within 1 minute and then decreased until it reached room temperature. The highest temperatures were always located near the bottom of the cup due to the low foaming capability of these formulations.

We also performed scanning electron microscopy (SEM) on cross-sections of the foams to observe the types and sizes of pores produced during the reaction (**Figure 4**). We observed shapeless-cell structures when TDI was used (**Figure 4A**). The structure of foam prepared from HDT showed mostly closed cells (**Figure 4B**), while we detected open cells when the foam was produced by mixture of HDT and IPDI (**Figure 4C**).

DISCUSSION

Foams prepared with aromatic isocyanates such as TDI and methylene diphenyl diisocayante (MDI) makes up 90% of the foams market share. IPDI and HDT are used for producing coatings because they provide more UV resistance, abrasion resistance, and weathering resistance (11). Glycerol, a molecule with three hydroxyl groups, acted as crosslinker for providing foams with sufficient rigidity and reduced shrinkage (27). SDS was used for stabilizing a pore structure during foam process. Aliphatic or cycloaliphatic (HDT and IPDI) and aromatic isocyanates (TDI and PMDI) were used because they have different reactivities (**Figure 1B**). In this work, the polyurethane foam was formed by two main reactions, namely a gelling reaction and a blowing reaction (**Figure 1C-D**). The polyurethane was formed by the exothermic reaction between hydroxyl -OH groups in the polyol with the -NCO isocyanate groups, resulting in urethane linkages. Additionally, the reaction of isocyanates with water resulted in the formation of urea linkage and carbon dioxide (CO_2), which then acted as blowing agent during foaming process (28). The evaporation of a low boiling solvent such as DCM induced an expansion of foams (29).

In our experimental conditions, the reactivity of isocyanates was the main factor controlling the properties of the foams. The foam produced with TDI showed a larger heat generation than with PMDI. Indeed, TDI is more reactive and displays a lower viscosity than PMDI. Compared to the cycloaliphatic/aliphatic isocyanates HDT and IPDI, the aromatic isocyanates TDI and PMDI have higher reactivity (low time at T_{max}) because the more electro-positive character of the C atom in NCO groups. Thus, the foams prepared with TDI or PMDI showed larger heat generation, lower volume expansion, and a shapeless-cell structure. Moreover, we found that the foam prepared with a mixture of HDT and IPDI displayed a faster reaction rate than with HDT alone, probably due to the lower viscosity of the mixture. This suggests that the properties of the foams can be therefore tuned by addition of other

Entry	Isocyanate		
	Abbreviation	Type	Amount (g)
PU1	TDI	Aromatic	10.8
PU2	PMDI	Aromatic	16.4
PU3	IPDI	Aliphatic	13.8
PU4	HDT	Cycloaliphatic	22.0
PU5	IPDI + HDT	Aliphatic + cycloaliphatic	7 + 11.4
PU6	IPDI	Aliphatic	13.8

Table 2: Types and amounts of isocyanates used in the formulation of the foams. The molar ratio between isocyanate and hydroxyl groups was ~1.

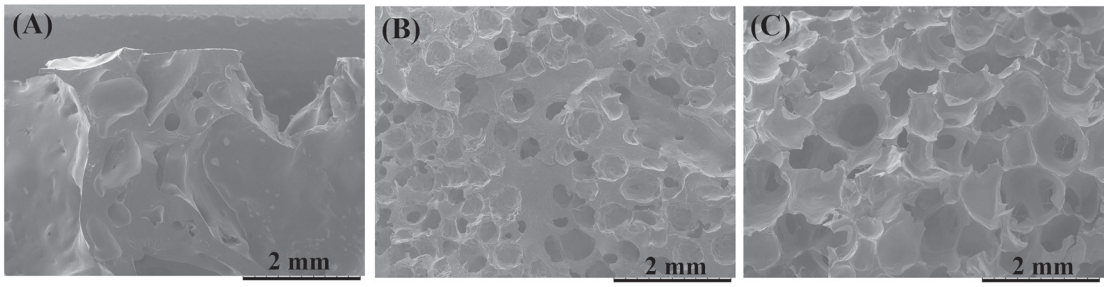

Figure 4: SEM images of PU foams prepared with TDI (A), HDT (B), and IPDI+HDT (C).

isocyanates. Longer reaction time, larger volume expansion, and well-defined morphologies of the foams are caused by a low reaction rate and a high viscosity of isocyanates.

As expected, we detected the highest temperature (white) by the infrared camera in the middle of the foam due to the exothermic nature of the reaction. The foam cells likely elongated quickly and shrunk immediately, resulting from the fast reaction with TDI and the very fast evaporation of DCM blowing agent. It is interesting to note that the heat generated during the reaction was not distributed equally in the foam. This means that the foam prepared in similar experimental conditions are by nature anisotropic, meaning that the properties are different at different locations inside the foams. The students could potentially isolate different portions of the foams and study their density and the morphology and size of the foam cells. The experiments described in the current document were easy to prepare, perform, and interpretate. Quantitative information about the formation of polyurethane foams was retrieved in the form of colourful images. The infrared camera could be further used for monitoring other exothermic reactions in the frame of chemistry classes.

MATERIALS AND METHODS

Safety precautions must be taken prior to and during the experiments. Health effects of isocyanate exposure are occupational asthma, chest tightness, difficult breathing, and irritation of skin, eye, nose, throat, and mucous membranes (26). Isocyanates are classified as potential human carcinogens and known to cause cancer in animals. Dibutyltin dilaurate can cause an allergic skin reaction, damage to organs, severe skin burns, and eye/DNA damage (30). Thus, students are required to wear safety goggles, gloves, mask, and a lab coat during the experiments. The experiment must be set up under a hood.

Materials

Poly(ethylene glycol) 6000 (PEG, 6000 g/mol, Acros Organics), sodium dodecyl sulfate (99% SDS, Acros Organics), tolylene 2,4-diisocyanate (80% TDI, Acros Organics), triethylamine (TEA, Carlo Erba), glycerol (Carlo Erba), dichloromethane (DCM, Honeywell), and dibutyltin dilaurate (95% DBTDL, Sigma) were used as received. Tolonate HDT (HDT) and isophorone diisocyanate (IPDI) were a generous gift from Vencorex, while polymeric methylene diphenyl diisocyanate (PMDI), triethylene glycol (TEG), and bisphenol A (Bis A) were supplied by PTT Global Chemical Company.

Formation of polyurethane foams

The students worked together in pairs. 5 g PEG, 5 g triethylene glycol, and 5 g bisphenol A were mixed with 0.4 g SDS (surfactant) and 0.6 g glycerol (crosslinker) in a plastic cup. The mixture was subsequently incubated at 80°C in an oven for 24 h to be homogenously liquified. In another vial, 0.4 g TEA and 0.5 g DBTDL was mixed with 0.1 g water and 0.8 g dichloromethane (blowing agent). Calculated amounts of isocyanates were added to the mixture of polyols, surfactant, crosslinker, catalyst, and blowing agents (**Table 2**). The mixtures were then stirred for 10 s by vigorous manual stirring.

Observation of foam formation with an infrared camera and foams characteristics

The students observed the temporal evolution of the foam during the reaction with an infrared camera (FLIR T450sc Science/Research Thermal Camera, 60 Hz, w/ 25 Degree Lens, USA). The IR camera was placed in front of a plastic cup at a distance of 32 cm (**Figure 5**). Experimental data such as reaction time, reaction temperature, foam height, and volume expansion could be extracted from the measurements. The students repeated the experiments in triplicate for each formulation. Scanning electron microscopy (SEM, Tabletop Hitachi, 3030Plus) operated at 15 kV was used to observe the cell morphology of PU foams. The foams were placed in liquid nitrogen before being cut prior to SEM imaging.

ACKNOWLEDGEMENTS

The work was supported by the Vidyasirimedhi Institute of Science and Technology (VISTEC) and the Office of the Higher Education Commission of Thailand (OHEC). We acknowledge PTT Global Chemical for supplying triethylene glycol and Vencorex for giving Tolonate HDT and isophorone diisocyanate. R.J. appreciates the Postdoctoral Fellowship of the Vidyasirimedhi Institute of Science and Technology.

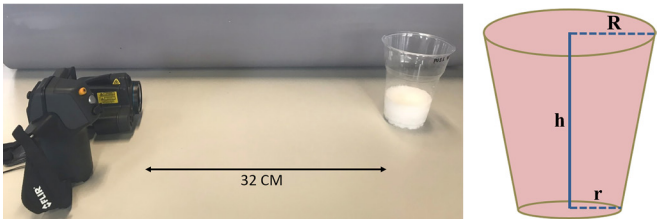

Figure 5: Experimental set-up for monitoring foam formation with an infrared camera (left). Volume expansion was estimated by approximating the geometry of the formed foam with a truncated circular cone and by measuring R, h, and r (right). The obtained volume is then $V = 1/3\ \pi.h.(R^2+r^2+R.r)$.

Received: March 3, 2020
Accepted: Septemer 29, 2020
Published: March 17, 2021

REFERENCES

1. Gama N., Ferreira A., and Barros-Timmons A. "Polyurethane foams: Past, present, and future." *Materials*, vol. 11, 2018, pp. 1-35., doi: 10.3390/ma11101841.
2. Akindoyo J. O., Beg M. D. H., Ghazali S., Islam M., Jeyaratnam N., and Yuvaraj A. R. "Polyurethane types, synthesis and applications-a review." *RSC Adv*ances, vol. 6, 2016, pp. 114453-114482., doi: 10.1039/C6RA14525F.
3. Ekkaphan P., Sooksai S., Chantarasiri N., and Petsom A. "Bio-based polyols from seed oils for water-blown rigid polyurethane foam preparation." *International Journal of Polymer Science*, vol. 2016, 2016, doi. org/10.1155/2016/4909857.
4. Ugarte L., Saralegi A., Fernández R., Martín L., Corcuera M., and Eceiza A. "Flexible polyurethane foams based on 100% renewably sourced polyols." *Industrial Crops and Products*, vol. 62, 2014, pp. 545-551., doi: org/10.1016/j.indcrop.2014.09.028.
5. Li W., Ryan A. J., and Meier I. K. "Effect of chain extenders on the morphology development in flexible polyurethane foam." *Macromolecules*, vol. 35, 2002, pp. 6306-6312., doi. org/10.1021/ma020231l.
6. Heintz A. M., Duffy D. J., Nelson C. M., Hua Y., Hsu S. L., Suen W., and Paul C. W. A. "A spectroscopic analysis of the phase evolution in polyurethane foams." *Macromolecules*, vol. 38, 2005, pp. 9192-9199., doi: org/10.1021/ma051599w.
7. Wang C., Zheng Y., Xie Y., Qiao K., Sun Y., and Yue L. "Synthesis of bio-castor oil polyurethane flexible foams and the influence of biotic component on their performance." *Journal of Polymer Research*, vol. 22, 2015, pp. 145., doi: 10.1007/s10965-015-0782-7.
8. Canham G. R., and Hocking M. B. "Polyurethane foam demonstrations: The unappreciated toxicity of toluene-2, 4-diisocyanate." *Journal of Chemical Education,* vol. 51, 1974, A580., doi: org/10.1021/ed051pA580.1.
9. Pinto M. L. "Formulation, preparation, and characterization of polyurethane foams." *Journal of Chemical Education*, vol. 87, 2010, pp. 212-215., doi: org/10.1021/ed8000599.
10. Cullen J. and Scott F. J., "Preparation of a polymeric foam: an activity designed to increase teachers' awareness of the utility of condensation polymerization." *Journal of Chemical Education*., vol. 95, 2018, pp. 419-422., doi: org/10.1021/acs.jchemed.7b00577.
11. Vadivambal R. and Jayas D. S. "Applications of thermal imaging in agriculture and food industry-a review." *Food and Bioprocess Technology*. vol. 4, 2011, pp. 186-199., doi: 10.1007/s11947-010-0333-5.
12. Barin J. S., Tischer B., Oliveira A. S., Wagner R., Costa A. B., and Flores E. M., "Infrared thermal imaging: A tool for simple, simultaneous, and high-throughput enthalpimetric analysis." *Analytical Chemistry*, vol. 87, 2015, pp. 12065-12070., doi: org/10.1021/acs.analchem.5b02753.
13. Kaplan H. "Infrared thermal imaging applications for manufacturing processes and quality control: an overview." *Proceedings. SPIE*., vol. 2063, 1993, pp. 88-97., doi: org/10.1117/12.164956.
14. Gowen A., Tiwari B., Cullen P., McDonnell K., and O'Donnell C. P. "Applications of thermal imaging in food quality and safety assessment." *Trends in Food Science & Technology*. vol.21, 2010, pp. 190-200., doi: org/10.1016/j.tifs.2009.12.002.
15. Ding L., Dong D., Jiao L., and Zheng W. "Potential using of infrared thermal imaging to detect volatile compounds released from decayed grapes." *PLOS ONE*, vol. 12, 2017, e0180649., doi: 10.1371/journal.pone.0180649.
16. Lahiri B., Bagavathiappan S., Jayakumar T., and Philip J. "Medical applications of infrared thermography: a review." *Infrared Physics & Technology*., vol. 55, 2012, pp. 221-235., doi: org/10.1016/j.infrared.2012.03.007.
17. Chojnowski M. "Infrared thermal imaging in connective tissue diseases." *Reumatologia*, vol. 55, 2017, pp. 38-43., doi: 10.5114/reum.2017.66686.
18. Hany C., Pradere C., Toutain J. and Batsale J.-C. "A millifluidic calorimeter with infrared thermography for the measurement of chemical reaction enthalpy and kinetics." *Quantitative InfraRed Thermography Journal*, vol. 5, 2008, pp. 211-229., doi: org/10.3166/qirt.5.211-229.
19. Loskyll J., Stoewe K., and Maier W. F. "Infrared thermography as a high-throughput tool in catalysis research." *ACS Combinatorial Science*., vol. 14, 2012, pp. 295-303., doi: org/10.1021/co200168s.
20. Cabello R., Navarro-Esbrí J., Llopis R., and Torrella E. "Infrared thermography as a useful tool to improve learning in heat transfer related subjects." *International Journal of Engineering Education*, vol. 22, 2006, pp. 373-380., WOSUID: WOS:000236825500018.
21. Micha D. N., Penello G. M., Kawabata R. M. S., and Camarotti T. ""Seeing the invisible": low cost and ordinary materials experiments." *Revista Brasileira de Ensino de Física.*, vol. 33, 2011, pp. 1501-1506., doi: org/10.1590/S1806-11172011000100015.
22. Haglund J., Jeppsson F., and Schönborn K. J. "Taking on the heat-a narrative account of how infrared cameras invite instant inquiry." *Research in Science Education*, vol. 46, 2016, pp. 685-713., doi: 10.1007/s11165-015-9476-8.
23. Perez de Azpeitia F. I. d. P. "Infrared thermography: an amazing resource for teaching physics and chemistry." *Eureka Magazine Teaching and Dissemination of Sciences*, vol. 13, 2016, pp. 617-627., http://hdl.handle.net/10498/18501.
24. Xie C. "Visualizing chemistry with infrared imaging." *Journal of Chemical Education*, vol. 88, 2011, pp. 881-885., doi: org/10.1021/ed1009656.
25. Jong Y. C., Ting Y. H., Mei F. S., Herre T., and Wim E. H. "Polyurethane-based drug delivery systems." *International Journal of Pharmaceutics*, vol. 450, 2013, pp. 145-162., doi: org/10.1016/j.ijpharm.2013.04.063.
26. Linda B., Mariëlle S., and Anna A. S. "The role of isocyanates in fire toxicity." *Fire Science Reviews*, vol. 5, 2016., doi: 10.1186/s40038-016-0013-2.
27. Baser S. and Khakhar D. "Castor-oil-glycerol blends as polyols for rigid polyurethane foams." *Cellular Polymer*, vol. 12, 1993, pp. 390-401., http://dspace.library.iitb.ac.in/xmlui/handle/10054/11629.

28. Mutsuga M., Yamaguchi M., and Kawamura Y. "Quantification of isocyanates and amines in polyurethane foams and coated products by liquid chromatography-tandem mass spectrometry." *Food Science & Nutrition*, vol. 2, 2014. pp. 156-163., doi: 10.1002/fsn3.88.
29. Choe K. H., Lee D. S., Seo W. J., and Kim W. N. "Properties of rigid polyurethane foams with blowing agents and catalysts." *Polymer Journal*, vol. 36, 2004. pp. 368-373., doi: 10.1295/polymj.36.368.
30. Minghua J., Peilin S., Na L., Xuejun L., and Jiajun C. "A plastic stabilizer dibutyltin dilaurate induces subchronic neurotoxicity in rats." *Neural Regeneration Research*. vol. 7, 2012, pp. 2213-2220., doi: 10.3969/j.issn.1673-5374.2012.028.007.

JOURNAL OF
EMERGING INVESTIGATORS

Article

Phytochemical Analysis of *Amaranthus spinosus* Linn.: An *in vitro* Analysis

Ishir Sharma[1], Pooja Kasture[2], Ankita Umrao[2], Jyothsna Rao[2], Gururaj Rao[2]
[1] The International School Bangalore, NAFL Valley, Whitefield – Sarjapur Road, Bangalore, KA, India, 562125
[2]iCREST-International Stem Cell Services Limited, 9/1, Mission Road, Bangalore

SUMMARY

Mainstream cancer treatments, which include radiotherapy and chemotherapeutic drugs, are known to induce oxidative damage to healthy somatic cells due to the liberation of harmful free radicals. In order to avert this, physiological antioxidants must be complemented with external antioxidants. We performed a preliminary phytochemical screen to identify alkaloids, saponins, flavonoids, polyphenols, and tannins in all parts of the *Amaranthus spinosus* Linn. plant. Based on the hits we obtained, we combined the methanolic extract of the leaves with the acetonic extract of the inflorescence, which resulted in a highly potent formulation which was abundant with the all the desired phytocomponents such as saponins, tannins, polyphenols, flavonoids, alkaloids. We hypothesised that this crude herbal extract, AS20, will exhibit high antioxidant properties. Using the 2,2′-diphenyl-1-picrylhydrazyl radical (DPPH) assay, we found that the half maximal inhibitory concentration (IC50) value of this formulation was 85.27 µg/mL. This paper describes the preparation of this crude extract and assesses its antioxidant properties for potential use in complementary cancer treatment.

INTRODUCTION

Integrative oncology is a rapidly emerging branch of the health sciences which aims to complement the existing course of cancer treatment with other remedies to avert the side effects of mainstream treatment (1). Examples of mainstream cancer treatments include surgery, chemotherapy, and radiotherapy. Oncologists worldwide are recognizing the need to prevent the deleterious side effects that such treatments induce upon patients. In an effort to prevent oxidative damage of cells by harmful free radicals, such as reactive oxygen species (ROS) (2), oncologists have embraced the usage of herbal antioxidants alongside the course of cancer treatment. Hence, by complementing physiological antioxidants with external herbal products, we would theoretically be able to prevent oxidative cell damage to healthy body cells, while retaining the anticarcinogenic properties of the mainstream drug. This would remove the need for alternative methods of treatments, as such methods integrate into pre-existing therapies. Evidently, the scope for research in this field is vast, as researchers search for more methods such as this one to administering cancer drugs more efficiently. In this paper, we will assess the ability of a crude herbal extract of the *Amaranthus spinosus* (AS) plant to exhibit significant antioxidant properties. To create this herbal formulation, we combined extracts of different parts of the plant which had the highest concentration of the desired phytocomponents, based on the preliminary phytochemical analysis of the plant. This paper describes the preparation of a crude extract which is a true representative of the potency of the entire *Amaranthus spinosus* (AS) plant.

The *Amaranthus spinosus* Linn. plant ('Spiny amaranth', 'Prickly amaranth', or 'Spiny pigweed') (3) is a medicinal plant which is found in abundance in India and around the world. This plant is commonly found as a weed in rice agriculture (4). Historically, this plant has been used extensively in Ayurveda (5), the traditional folk medicine of India, to treat diabetes, jaundice (6), and various other ailments. Previous studies have shown this plant to possess several medicinal properties, including anti-inflammatory (7), anti-diabetic (8), anti-diarrheal (9), anti-bacterial (10), anti- microbial (11), and anti-malarial (12) properties. Hence, the medicinal properties of this plant are of keen interest to the scientific community. While previous phytochemical studies have been done on individual parts of this plant, such as the leaves, the properties of the entire plant are relatively unknown to the world of science, and there has been little attempt to prepare pharmaceutical drugs from this plant. The most common way to prepare a pharmaceutical drug is to isolate a specific phytocomponent. However, given our goal to create an herbal crude extract, the total content of the desired secondary metabolites was determined for each part of the plant (leaves, root, stem, inflorescence).

The normal course of treatment for cancer is to employ surgery, chemotherapeutic drugs, or radiotherapy. While the usage of radiation or drugs does kill the cancer cells, it also induces cell stress, which causes an increase of harmful free radicals, such as reactive oxygen species (ROS), which react with various cell parts, including the phospholipid bilayer, amino acids, and DNA, causing severe oxidative damage to all these cell components (13). Furthermore, physiological antioxidant enzymes, such as superoxide dismutase, are inhibited by the activity of anti-cancer drugs. As a result, it becomes a necessity to include an external antioxidant dosage to complement the existing therapies in order to avert the side effects on healthy somatic cells.

Secondary metabolites are organic compounds produced primarily by plants as waste products of their metabolism.

They exhibit significant pharmacological and biological properties and are hence used for medical purposes (14). The secondary metabolite groups considered in this study were alkaloids, saponins, polyphenols, flavonoids, and tannins. The total content of each of these phytochemicals is usually determined by carrying out phytochemical tests (based on colorimetry) for each of these secondary metabolites. Alkaloids are basic compounds with heterocyclic rings. Their most common functional group is the amine group (NH2). The nitrogen acts as a Brønsted base, its lone pair of electrons acting as proton acceptors, and the hydrogen atoms act as proton donors (or a Brønsted acid) for hydrogen bonding. The acid-base properties of the amine group make alkaloids ideal bioactive molecules as they have the ability to bind to different proteins, receptors, and drug targets (15). Alkaloids have been shown to display significant antioxidant properties (16). Saponins are glycosidic compounds whose amphipathic nature gives them the ability to interact with various cell membrane components, such as cholesterol and phospholipids. Saponins are reported to be effective *in vitro* antioxidants (17). Polyphenols are polymers of phenols, which consist of a six membered cyclical ring (phenyl group). Polyphenols are known to have considerable antioxidant properties, which have been extensively studied over the last few decades (18). Their bioactivity comes from their ability to form hydrophobic and ionic bonds with proteins (19). Flavonoids are a type of phenolic compound which also possess antioxidant properties *in vitro* (20). They are abundantly present in tea and other plant-derived beverages. Tannins are water soluble phenols which are known to be proton donors. Their antioxidant properties include free radical scavenging, inhibition of stages of oxidation, and chelation of metal cations (21).Thus, we hypothesised that the crude extract, containing a greater content of these secondary metabolites compared to solvent extractions of individual parts of the plant, would display significant free radical quenching properties, as determined through calculation of the half maximal inhibitory concentration (IC50) value for the crude extract formulation obtained using the 2,2′-diphenyl-1-picrylhydrazyl radical (DPPH) assay.

RESULTS

The phytochemical screening of the AS plant extracts consisted of a series of chemical tests, based on colorimetry, which yielded the total concentration of each of the secondary metabolites in each solvent extraction. We measured these using Dragendorff's test for alkaloids, vanillin-sulphuric acid for saponins, aluminium chloride colorimetric assay for flavonoids, Folin-Ciocalteu's (FC) reagent for phenolic content, and the FC method for tannins. We prepared extracts of the individual parts of the plant using a range of solvents and phytochemically analysed them to determine the total content of the secondary metabolite groups of interest. We then prepared a formulation by combining the extracts with the highest concentration of anti-oxidants. A DPPH assay was then carried out on this formulation to quantify the amount of antioxidants present in the extract.

Solvent	Sample	Saponin test	Polyphenol test	Flavonoid test	Alkaloid test	Tannin test
Water Extract	Root	+++	+	+	++	+
	Inflorescence	+++	++	+	++	-
	Stem	+++	+	+	++	-
	Leaf	+++	+++	++	+++	-
Methanol Extract	Root	+++	+	-	-	-
	Inflorescence	+++	++	-	++	+
	Stem	+++	+	-	-	-
	Leaf	+++	+++	-	+++	-
Ethanol Extract	Root	+	-	+	-	-
	Inflorescence	+	+	-	++	+
	Stem	+	+	+	-	-
	Leaf	+	-	-	++	+
Chloroform Extract	Root	-	+	-	-	-
	Inflorescence	+	+	-	++	+
	Stem	-	-	-	++	+
	Leaf	-	-	-	-	-
Acetone Extract	Root	-	-	+	-	-
	Inflorescence	-	-	+++	-	-
	Stem	+	-	+	-	-
	Leaf	-	-	+	++	+

Table 1: The qualitative analysiswere tabulated using +++ ,++,+ for presence of phytochemicals and – for absence of phytochemicals and quantitative ranges of concentration were tabulated using the following notation. +++ for 1001-2000µg/ml, ++ for 501-1000 µg/ml,+ for 0-500 µg/ml.

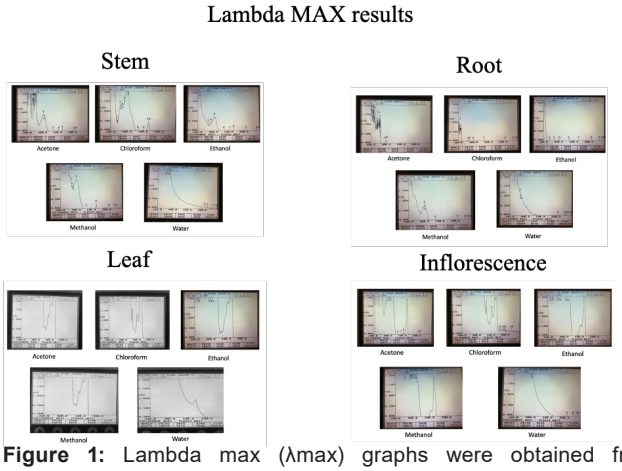

Figure 1: Lambda max (λmax) graphs were obtained from the spectrophotometer. The peaks represent the presence of phytocomponents. Spectra were measured at a wavelength range from 200-1000 nm to validate the presence of phytocomponents, prior to the screening of the different plant parts.

From the lambda max readings **(Figure 1)** and the phytochemical screening results **(Table 2)**, it was evident that certain solvent extracts of particular parts of the plant contained high amounts of all the phytocomponents **(Figure 2)**. The primary aim of the phytochemical screening was to determine the parts of the plant which contained the highest content of specific desired phytochemicals. Therefore, AS20 was prepared according to the following formulation, which was representative of the maximum potency of the entire plant:

AS20 = Inflorescence Acetonic extract + Leaf Methanolic extract

The methanolic extract of the leaves displayed a substantially high presence (+++) of nearly all the phytochemical groups, apart from flavonoids and tannins **(Table 2)**. Another group of interest was the inflorescence, which was the only group which displayed high presence (+++) of flavonoids (which are known to possess antioxidant properties) (22). As a result, the acetonic extract of the inflorescence and the methanolic extract of the leaves of the AS plant were combined to produce a drug (AS20) which had a high presence (+++) for all the phytochemical groups considered **(Table 2)**. Furthermore, AS20 displayed free radical scavenging property, as indicated by the DPPH assay results **(Figure 3)**. The % inhibition of free radicals increased linearly with concentration of the formulation, represented by the equation y=0.5281x+4.9671 (R2 ~ 0.98). From the equation obtained, the IC50 value (concentration of the drug at which 50% of free radical inhibition occurs) was calculated as below:

$$(50) = 0.521x + 4.9671 \rightarrow \therefore x = \frac{50 - 4.9671}{0.521} = 85.27\mu g\ mL^{-1}$$

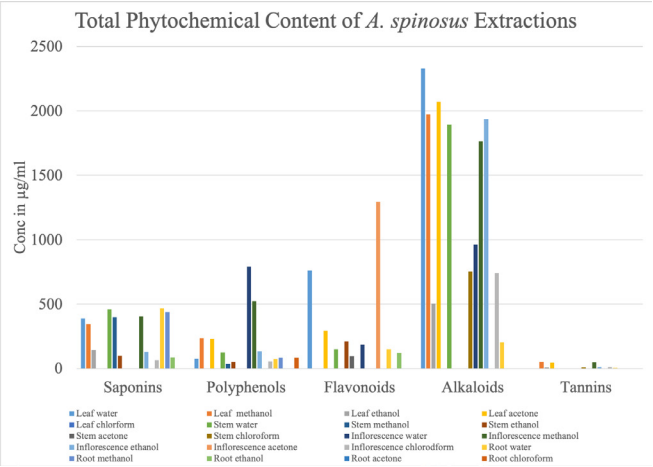

Figure 2: Bar graphs displaying total content of each phytochemical for all extractions (water, methanol, ethanol, acetone, and chloroform) of A. spinosus leaf, stem, inflorescence, and root. The concentration readings were measured in µg/mL. The quantitative phytochemical studies were based on the data in Table 2.

DISCUSSION

The rationale behind the preparation of AS20 was to combine specific solvent extracts from various parts of the AS Linn. plant with the greatest concentrations of all the phytochemical groups (alkaloids, saponins, tannins, flavonoids, and polyphenols). The result was the herbal combination AS20, which contained all the studied phytochemicals in high concentrations. Prior studies of the entire plant have assessed the antioxidant properties of the entire plant in hydroalcoholic extracts, wherein the IC50 value obtained by the DPPH method was 525.593 µg/mL (23). Moreover, the IC50 value for the DPPH assay of the methanolic extract of the leaves of AS as determined by Kumar et al. (24) was 87.527 µg/mL. Having obtained a marginally lower IC50 value of 85.27 µg/mL in this study, we have shown that AS20 also may have a mildly higher antioxidant capacity than both its individual constituents as well as the generic extract of the entire plant. The AS20 formulation is thus one which is representative of a higher antioxidant potency of the AS plant relative to its individual constituents. The antioxidant property of the formulation thus has implications for usage as a complementary dosage during cancer treatment to assist in averting damage to healthy somatic cells due to harmful free radicals produced during treatment.

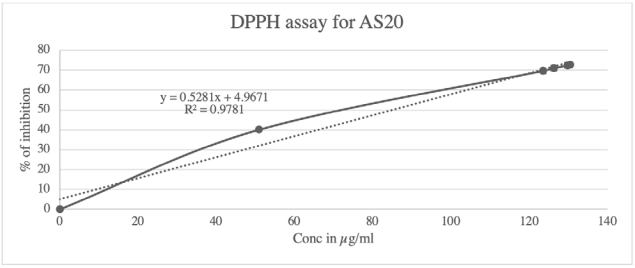

Figure 3: Line graph for DPPH assay results. The graph depicts the % inhibition of free radicals with increase in concentration of AS20 in µg/mL. This graph is representative of the antioxidant property of the formulation in terms of free-radical scavenging capacity. The IC50 value was determined using the graph.

Due to the many steps involved, we had potential for experimental errors, such as pipetting errors. Specifically, we assumed that for steps performed at room temperature, it stayed constant over the course of the experiment. We did not thermostatically monitor the laboratory temperature. We assumed the start time for incubation of all the concentrations to be the same for the DPPH assay, whereas we added the reagent sequentially into each of the five test tubes.

A limitation of our study is that we assessed the free radical scavenging ability of the formulation but not that of the extracts of the different parts of the plant, for which we relied on literature. Furthermore, we conducted the qualitative and quantitative phytochemical studies once for each extract. Future studies could 1) compare the antioxidant properties of the formulation with those of its individual components to confirm that it has a higher overall antioxidant potential than each of its components, 2) increase the number of trials and calculate the average phytochemical content of each extract to improve the reliability of the results, and 3) explore employing other antioxidant assays, such as the Total Antioxidant Capacity (TAC) Assay.

Future explorations could include expanding the scope of investigation to include examining this formulation for its other pharmacological activities, such as anticancer, antimicrobial, and antifungal activities. This will permit the assessment of other properties which may be beneficial in treatment of various ailments, such as cancer. In addition, other species of the Amaranth genus could be assessed. The efficacy of crude extracts from other species can be compared to the AS20 formulation. Furthermore, inter-species combinations

may also be explored for enhanced biological activities.

MATERIALS AND METHODS

Extract preparation

A. spinosus plants were obtained from a local nursery in Bengaluru. The leaves, stem, and inflorescence of the plant, as shown in **Figure 4**, were separated using scissors and cleaned by hand to remove insects. Subsequently, they were spread out over a large cloth and air-dried for a period of five days, to ensure complete removal of moisture content. After drying, the samples were ground separately in a grinding mixer and sieved into separate centrifuge tubes. The solvents used for extraction (water, methanol, ethanol, chloroform, and acetone) were selected to have a range of polarities.

The process of ground-drying using a grinding mixer was not feasible for the AS roots due to their fibrous nature. Hence, the process of maceration was employed wherein 1 g of roots were soaked in 20 mL of each solvent at room temperature for 24 hours. For each plant part, 1 g of ground powder was measured using a weighing balance and was dissolved in 10 mL of each of the five solvents [1 g/10 mL]. The contents were then decanted out of the conical flasks into centrifuge tubes. The tubes were centrifuged for 15 minutes at 3000 rpm to remove undissolved debris. Subsequently, the supernatants were collected into clean test tubes labelled according to plant part and solvent. A 1:2 dilution of crude sample volume to solvent volume ratio was then carried out in these tubes using the respective solvents. The centrifuge tubes containing leaf, stem, inflorescence, and root extract were then stored at 5°C.

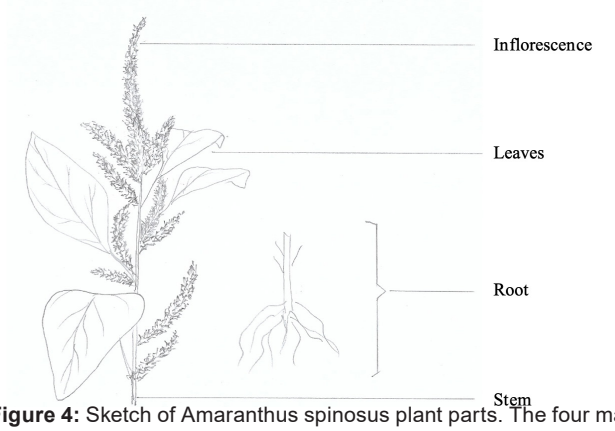

Figure 4: Sketch of Amaranthus spinosus plant parts. The four main parts of the plant are labelled as inflorescence, leaves, root, and stem. These parts were separated by hand prior to extraction.

Phytochemical Screening

Lambda max (λ_{max}) is the wavelength at which a compound displays its highest absorption in the spectrophotometer. The lambda max value represents a peak, which indicates the presence of phytocomponents **(Figure 1)**. Phytochemical screening involved the analysis of the total content (concentration) of alkaloids, saponins, flavonoids, polyphenols, and tannins.

Preliminary Qualitative Analysis:

Qualitative analyses were carried out according to the methods used by Kokate (25) and Rahman Gul et al. (26) **(Table 2)**. In the Dragendorff's test for alkaloids, 0.2 mL of diluted extract was added to 0.5 mL of each extract and 1 mL of Dragendorff's reagent was then added to this solution. An orange-brown precipitate was formed if alkaloids were present. In the olive oil test for saponins, 0.5 mL of each extract was added to 0.2 mL of olive oil, shaken vigorously, and left standing for 5 minutes. A soluble emulsion was formed if saponins were present. In the alkaline reagent test for flavonoids, five drops of 5% NaOH were added to 0.5 mL of extract, which yielded a yellow colour, then a few drops of 2 molar HCl were added to the solution. The solution became colourless if flavonoids were present. For polyphenols, the Folin-Ciocalteu's (FC) reagent test was carried out. Four drops of FC reagent and Na2Co3 were added to 0.5 mL of the sample, which was incubated at room temperature in the dark for 20 minutes. A blue colour was formed if polyphenols were present. For tannins, a ferric chloride test was carried out. A few drops of 5% FeCl3were added to 0.5 mL of extract and a blue-green colour formed if tannins were present.

Quantitative Analysis:

Quantitative analysis was performed as follows **(Table 2)**:

Phytocomponent	Qualitative Test	Quantitative Analysis	Standards used for Quantitative Analysis
Alkaloid	Dragendorff'sTest	Total Alkaloids	Bismuth Nitrate
Saponin	Olive Oil Test	Total Saponins	Diosgenin
Flavonoid	Alkaline Reagent Test	Total Flavonoids	Quercetin
Polyphenol	Folin-Ciocalteu's Test	Total Polyphenols	Gallic Acid
Tannin	Ferric Chloride Test	Total Tannins	Tannic Acid

Table 2: Phytochemical tests and standards. The qualitative and quantitative tests for alkaloids, saponins, flavonoids, polyphenols, and tannins were tabulated, along with the respective standard solutions used for quantitative analysis.

Total Alkaloid Content

To determine the total alkaloid content, the procedure used was adapted from that followed by Ellul (27). The chemicals used were 50 mg/L bismuth nitrate, 1 M thiourea, 1 M diluted hydrochloric acid, and 5% disodium sulphide. The standard curve was obtained with bismuth nitrate pentahydrate stock solution. Serial dilutions of standard stock was made by pipetting out 0, 0.2, 0.4, 0.6, 0.8 and 1 mL respectively. Standard stock of 50 mg/L Bismath nitrate pentahydrate was taken in the test tubes with 0.2 mL of test samples. Five millilitres of thiourea solution was added, and water was used to make up the volume to 10 mL. Absorbance was read at 435 nm. For the herbal sample, the samples were maintained at pH 2-2.5 with 1 M hydrochloric acid. Subsequently, 2 mL of Dragendorff's solution was added, and the solution was centrifuged for 10 minutes at 1500 rpm for precipitation. After centrifugation, 2 mL of disodium sulphide solution was added, and a brown-black precipitate was formed. Two millilitres of concentrated nitric acid was then added, and the volume was made up to 10 mL with water. One millilitre of solution was

discarded, and 5 mL of thiourea was added. The absorbance was read, and the concentration was determined on the basis of the standard curve.

Total Saponin Content

To determine the total saponin content, the vanillin-sulphuric acid method (28) was used. The chemicals used were 8% (w/v) vanillin, 72% (v/v) sulphuric acid, and 0.5 mg/mL diosgenin. A quantity of 0.25 mL of sample was added to 0.25 mL of 8% vanillin in ethanol and 2.5 mL of 72% sulphuric acid. The solutions were incubated for 15 minutes at 60°C. The absorbance of the standards were measured at 765 nm. A standard curve was plotted against diosgenin, and the concentration was hence determined by extrapolation.

Total Flavonoid Content

To determine the total flavonoid content (29), the aluminium chloride colorimetric assay was carried out, and the chemicals used were 10% aluminium chloride, 5% sodium nitrite, 10 mg of Quercetin and 1 M sodium hydroxide. One millilitre of test sample and 1 mL of standard Quercetin solution were aliquoted into test tubes, and 4 mL of distilled water and 0.3 mL of 5% sodium nitrite solution were added into each tube. After 5 minutes, 0.3 mL of 10% aluminium chloride was added. At the sixth minute, 2 mL of 1 M sodium hydroxide was added, and the volume was made up to 10 mL with distilled water and mixed well. An orange colour appeared, and the absorbance at 630 nm was measured for each sample. The concentration was determined by using the standard curve against Quercetin.

Total Phenolic Content

To determine the total phenolic content (30), the chemicals used were Folin-Ciocalteu's (FC) reagent, 8% saturated sodium carbonate solution, and 25 mg/50 mL gallic acid. The total phenolics of the extract were determined using FC reagent. Standard readings were made using a spectrophotometer at 765 nm against a black reagent. A quantity of 0.2 mL of the test sample was mixed with 0.6 mL of water and 0.2 mL of FC reagent. After 5 minutes, 1 mL of sodium carbonate was added to the solution and the volume was made up to 3 mL with distilled water. The solutions were incubated for 30 minutes at room temperature and then centrifuged. The absorbance of each sample was measured. The phenol concentration was calculated as gallic acid equivalent on the basis of a standard curve.

Total Tannin Content

For determination of the total tannin content (31), the chemicals used were FC reagent, saturated sodium carbonate solution (8% w/v), and 6.25 mg/50 mL tannic acid. The total tannin content of the extract was determined using FC method. Subsequently, 0.2 mL of the test sample was mixed with 7.5 mL of distilled water and 0.5 mL of FC reagent. A quantity of 1 mL of 35% sodium carbonate was then added, and the volume was made up to 10 mL with distilled water. The mixture was shaken and incubated at room temperature for 30 minutes. A set of reference standard solutions of tannic acid were prepared using the same method (20, 40, 60, 80, and 100 µg/mL). Absorbance was measured at 700 nm. The sample concentrations were calculated using the tannic acid standard curve.

Preparation of AS20

The AS20 formulation was prepared according to the data obtained from the qualitative and quantitative analyses of different solvent extracts of each of the parts of the plant. A combination of different extracts with high overall content of the phytocomponents was formulated. A significant challenge in creating such a combination is mixing solvents of varying polarities. Solvent extracts created by dissolving 1 g of powder in 10 mL of solvent were added in petri dishes. The mass of empty petri dish was recorded before adding the solvent. The petri dishes were air dried. After drying, the petri dish was weighed once again to determine the dry weight. Subsequently, 0.01 g/mL of dimethyl sulfoxide (DMSO) was added. After dissolution in DMSO, the desired extracts were mixed to form a polyherbal solution, AS20. DMSO was chosen due to its ability to act as a solvent for polar and non-polar compounds and its relative miscibility in a wide range of solutions.

DPPH Assay for AS20

The DPPH (2,2-diphenyl-1-picrylhydrazyl) assay (32) is a colorimetric assay which is used to determine the free radical scavenging activity of a substance. The principle behind the DPPH assay is the reduction of DPPH (a free radical) which results in a purple solution being formed in the presence of an antioxidant (33). In our study, we assessed this property in the AS20 formulation. 1.0, 50, 100, 150 and 200 µL volumes of the AS20 formulation were added into five glass test tubes. Appropriate volumes of methanol were added to these to make the volume up to 1 mL. Subsequently, 3 mL of DPPH solution was added quickly into the five test tubes, which were immediately incubated in the dark at room temperature for 15 minutes. The absorbance values were measured using the spectrophotometer at a wavelength of 517 nm, and a graph was plotted against the standard. The percentage inhibition (inhibition of reactive oxygen species, such as the superoxide radical) was calculated according to the formula:

$$\%\ \text{inhibition} = \frac{\text{OD control} - \text{OD sample}}{\text{OD control}} \times 100$$

A graph of concentration (µg/mL) on the x-axis against % inhibition along the y-axis was plotted for the AS20 DPPH assay. The IC50 value was found after fitting the data to a linear equation (y=mx+c). The point at which 50% inhibition of the reactive oxygen species had occurred was hence determined (see results):

$$(50) = mx + c \rightarrow \therefore x = \frac{50 - c}{m}$$

Received: June 10, 2020
Acccepted: October 12, 2020
Published: March 20, 2021

REFERENCES

1. Complementary Therapies. *Cancer Council*, 2020, www.cancer.org.au/cancer-information/treatment/complementary-therapies.
2. "Antioxidants and Cancer Prevention." Federal Occuptional Health, foh.psc.gov/NYCU/antioxidents.asp.
3. "*Amaranthus Spinosus*." Plants Profile for *Amaranthus Spinosus* (Spiny Amaranth), plants.usda.gov/core/profile?symbol=AMSP.
4. A Practical Field Guide to Weeds of Rice in Asia, by B. P. Caton et al., *International Rice Research Institute*, 2004, pp. 20–21.
5. Pal, Vipin Chandra, et al. "Pharmacognostical Studies of *Amaranthus Spinosus* Linn." *UK Journal of Pharmaceutical Biosciences*, vol. 1, no. 1, 2013, p. 32., doi:10.20510/ukjpb/1/i1/91112.
6. Tewari, Devesh, et al. "Ethnopharmacological Approaches for Therapy of Jaundice: Part I." *Frontiers in Pharmacology,* vol. 8, 2017, doi:10.3389/fphar.2017.00518.
7. Olajide, Olumayokun A., et al. "Anti-Inflammatory Properties Of *Amaranthus Spinosus* Leaf Extract." *Pharmaceutical Biology*, vol. 42, no. 7, 2004, pp. 521–525., doi:10.3109/13880200490893285.
8. Ahamath, J.M., et al. "Phytochemical studies and antibacterial activities of *Amaranthus spinosus* L." World Journal of. Pharmacy and Pharmaceutical Sciences, vol. 3, no. 12, 2014, pp. 1692-1697.
9. Hussain, Zeashan, et al. "Antidiarrheal and Antiulcer Activity Of *Amaranthus Spinosus* in Experimental Animals." *Pharmaceutical Biology*, vol. 47, no. 10, 2009, pp. 932–939., doi:10.1080/13880200902950769.
10. S, Harsha Vardhana. "*In Vitro* Antibacterial activity of *Amaranthus spinosus* root extracts," *Pharmacophore*, vol. 2 , no. 5, 2011, pp. 266-270.
11. ZC, Maiyo. "Antimicrobial activity of *Amaranthus spinosus* Linn." *African Journal of Biotechnology,* vol 9 (21), 2010, pp. 3178- 3182.
12. Hilou, A., et al. "In Vivo Antimalarial Activities of Extracts from *Amaranthus Spinosus* L. and Boerhaavia Erecta L. in Mice." *Journal of Ethnopharmacology,* vol. 103, no. 2, 2006, pp. 236–240., doi:10.1016/j.jep.2005.08.006.
13. Menon, Venugopal P., and Adluri Ram Sudheer. "Antioxidant And Anti-Inflammatory Properties Of Curcumin." *Advances in experimental medicine and biology,* The Molecular Targets and Therapeutic Uses of Curcumin in Health and Disease, pp. 105–125., doi:10.1007/978-0-387-46401-5_3.
14. Wink, Michael. "Modes of Action of Herbal Medicines and Plant Secondary Metabolites." *Medicines*, vol. 2, no. 3, 2015, pp. 251–286., doi:10.3390/medicines2030251.
15. Kittakoop, Prasat, et al. "Alkaloids as Important Scaffolds in Therapeutic Drugs for the Treatments of Cancer, Tuberculosis, and Smoking Cessation." *Current Topics in Medicinal Chemistry*, vol. 14, no. 2, 2013, pp. 239–252., doi:10.2174/1568026613666131216105049.
16. Tiong, Soon, et al. "Antidiabetic and Antioxidant Properties of Alkaloids from Catharanthus Roseus (L.) G. Don." *Molecules,* vol. 18, no. 8, 2013, pp. 9770–9784., doi:10.3390/molecules18089770.
17. Gülçin, Ilhami, et al. "Antioxidant Activity of Saponins Isolated from Ivy: α-Hederin, Hederasaponin-C, Hederacolchiside-E and Hederacolchiside-F." *Planta Medica*, vol. 70, no. 6, 2004, pp. 561–563., doi:10.1055/s-2004-827158.
18. Scalbert, Augustin, et al. "Polyphenols: Antioxidants and Beyond." *The American Journal of Clinical Nutrition*, vol. 81, no. 1, 2005, doi:10.1093/ajcn/81.1.215s.
19. Wink, Michael. "Modes of Action of Herbal Medicines and Plant Secondary Metabolites." *Medicines*, vol. 2, no. 3, 2015, pp. 251–286., doi:10.3390/medicines2030251.
20. Pietta, Pier-Giorgio. "Flavonoids as Antioxidants." *Journal of Natural Products*, vol. 63, no. 7, 2000, pp. 1035–1042., doi:10.1021/np9904509.
21. Amarowicz, Ryszard. "Tannins: the New Natural Antioxidants?" *European Journal of Lipid Science and Technology,* vol. 109, no. 6, 2007, pp. 549–551., doi:10.1002/ejlt.200700145.
22. Baral, Manik. "*In vitro* antioxidant activity of the whole plant of *Amaranthus spinosus*. Linn." *International journal of Biomedical and Pharmaceutical Sciences*, vol. 5, 2010, pp. 75-78.
23. Kumar, Bagepalli Srinivas Ashok, et al. "Antioxidant and Antipyretic Properties of Methanolic Extract of *Amaranthus Spinosus* Leaves." Asian Pacific Journal of Tropical Medicine, vol. 3, no. 9, 2010, pp. 702–706., doi:10.1016/s1995-7645(10)60169-1.
24. Practical Pharmacognosy, by C. K. Kokate, Vallabh Prakashan, 1994, pp. 107–113.
25. Gul, Rahman, et al. "Preliminary Phytochemical Screening, Quantitative Analysis of Alkaloids, and Antioxidant Activity of Crude Plant Extracts from Ephedra Intermedia Indigenous to Balochistan." *The Scientific World Journal*, vol. 2017, 2017, pp. 1–7., doi:10.1155/2017/5873648.
26. Ellul Micallef, Roger, and Rita Darmanin Ellul. "Determination of the Phytochemical, Antioxidant and Anti-Inflammatory Properties of Selected Maltese Medicinal Plants." *L-Università Ta' Malta*, University of Malta, 1 Jan. 2013, www.um.edu.mt/library/oar/handle/123456789/31934.
27. Le, Anh V., et al. "Improving the Vanillin-Sulphuric Acid Method for Quantifying Total Saponins." *Technologies*, vol. 6, no. 3, 2018, p. 84., doi:10.3390/technologies6030084.
28. Chang, C. "Estimation of total flavonoid content in propolis by two complementary colorimetric methods." J. *Food Drug Anal.*, vol. 10, 2002, pp. 178-182.
29. Mcdonald, Suzy, et al. "Phenolic Content and Antioxidant

Activity of Olive Extracts." *Food Chemistry,* vol. 73, no. 1, 2001, pp. 73–84., doi:10.1016/s0308-8146(00)00288-0.
30. CI, Kavitha Chandran, et al. "Quantitative estimation of total phenolic, flavonoids, tannin and chlorophyll content of leaves of Strobilanthes Kunthiana (Neelakurinji)." J*ournal of Medicinal Plants Studies*, vol. 4, no. 4, 2016, pp. 282-286.
31. Liyana-Pathirana, C.m., et al. "Antioxidant Activity of Cherry Laurel Fruit (Laurocerasus Officinalis Roem.) and Its Concentrated Juice." *Food Chemistry,* vol. 99, no. 1, 2006, pp. 121–128., doi:10.1016/j.foodchem.2005.06.046.
32. Huang, Dejian, et al. "The Chemistry behind Antioxidant Capacity Assays." *Journal of Agricultural and Food Chemistry*, vol. 53, no. 6, 2005, pp. 1841–1856. doi:10.1021/jf030723c.

JOURNAL OF
EMERGING INVESTIGATORS

Article

Comparison of the ease of use and accuracy of two machine learning algorithms – forestry case study

Bhavya Bhatia[1*], Jakub Michalski[2*], Jegath Shebin[3]
[1]Nord Anglia International School, Dubai, United Arab Emirates
[2]Dubai College, Dubai, United Arab Emirates
[3]NTT Data Services Chennai
*these authors contributed equally to this work

SUMMARY

With the availability of massive amounts of data and cheap computing, machine learning has become increasingly viable to create extensive multivariate mathematical models of natural phenomena to help predict accurate future trends that would have been impossible for humans to accomplish by themselves. There is a wide variety of different machine learning algorithms available, and it is not always known which one will perform best for a given dataset. This can be determined after training and evaluating the different models and comparing them. In this case study, logistic regression and random forest models were compared in terms of accuracy and ease of use. We hypothesized that logistic regression would yield a higher accuracy and be easier to set up in a comparable scenario for a given dataset compared to random forest. Both algorithms used the same forestry dataset to see which one would outperform the other. Initially, logistic regression looked like the better choice, however, after a variety of comparisons, random forest yielded higher performance in both accuracy measurements (accuracy=0.9722, Fβ=0.9722 for random forest vs. accuracy=0.7141, Fβ=0.6990 for logistic regression) and did not require as much detailed tuning as logistic regression did.

INTRODUCTION

Machine learning can be defined in many different ways. Arthur Samuel defined it as an ability of a computer to learn without telling it precisely what to do (1). However, a more modern definition can be that of Tom Mitchell. He defined it as "the study of computer algorithms that allow computer programs to automatically improve through experience" (2). Machine learning algorithms look for patterns and correlations between different independent variables and how they affect the dependent variable. The resulting trained model will then attempt to predict the outcome of a dependent variable in a new scenario based on independent variables put into it. Machine learning promises to analyze large quantities of data in an exponentially shorter time than a human would while finding patterns that may not have been obvious to any human operator. This is the main reason for the rapid interest in and growth of machine learning, demonstrated by the spending increase from $1.58 billion in 2017 to a predicted $20.83 billion in 2024 (3).

Data scientists must choose a suitable model from a variety of available methods, which is not always an easy choice to make. The advances made in machine learning in recent years have made it easier for the average user to try out different machine learning models. Currently, one of the most popular and easy-to-use frameworks for machine learning is scikit-learn, which is based on the Python programming language (4). It offers a variety of models ready to be used and trained, including logistic regression and random forest. Its high customizability proved to be useful in this investigation, as it allows for exploratory hyperparameter tuning. This pair of models were selected for this investigation in particular as these two methods have fundamentally different approaches to predicting the values of the dependent variables. Logistic regression tries to fit a straight-line separating data points in a dataset and minimizes the cost of the function by reducing incorrect predictions (5). Random forest makes predictions based on multiple decision trees, so the method is not limited by the constraints of a straight line and can be more versatile (6). Clearly, a random forest model is completely different from logistic regression. Furthermore, logistic regression is one of the oldest and simplest machine learning algorithms. Other models were also considered, such as support vector machines, but they do not differ from logistic regression as greatly as random forests do.

This presents the question of which of the two is easier to use and more accurate. We defined ease of use as to how time-consuming and work-intensive it was to set the model up. Based on our previous knowledge, the hypothesis was that logistic regression would be easier to use than the random forest model because random forest would take too long to develop for a similar accuracy. However, this hypothesis was rejected based on a variety of measures, including accuracy and Fβ scores. Accuracy is the proportion of accurate predictions, while the Fβ score is the harmonic mean of precision (false positive rate) and recall (false negative rate), with a beta parameter specifying the weight of precision or recall. For this investigation, the beta parameter is set to give more weight to precision, which should minimize the rate of false positives.

The dataset is forestry-based, containing numerous environmental variables (7). It was chosen arbitrarily as the focus of this investigation is on the models, not the dataset. The two models will be used to predict cover types for forests based on elevation, aspect, slope, and others.

Solver (no normalization)	Accuracy	Time needed (s)
newton-cg	0.7096	628
sag	0.6959	45
saga	0.6931	58
lbfgs	0.6223	28
Solver (normalization)	**Accuracy**	**Time needed (s)**
newton-cg	0.7141	635
sag	0.7140	40
saga	0.7139	62
lbfgs	0.7003	27

Table 1. Accuracy table for an equal number of iterations for different solvers. Separate results for solvers with and without normalization of data applied.

Solver	max_iter	Accuracy	Time needed (s)
newton-cg	34	0.7141	132
sag	400	0.7141	128
saga	250	0.7141	126
lbfgs	500	0.7115	127

Table 2. Accuracy results for an equal amount of time for different solvers. The max_iter parameter controlled how long each solver took

RESULTS

The first model tested was logistic regression. The different solvers for it were compared with and without normalization (**Table 1**). Normalization improved the performance of the sag and saga solvers, taking roughly the same physical time (within random variation) for the same accuracy (about 0.71). Normalization also minimally improved the accuracy for the newton-cg solver. Surprisingly, lbfgs benefited the most from normalization. Normalization was kept for the rest of the measurements due to improvements across all solvers.

However, we kept the time supplied to each solver constant, making the results easier to compare as ease of use is one of the criteria. Newton-cg, sag, and saga offer the same accuracy (0.7141) in a very similar time frame (**Table 2**), with lbfgs giving the lowest accuracy (0.7115) for the given time. Thus, it is hard to select the best solver due to the similarity in the accuracies and time needed.

With the solver selected and normalization applied, the number of iterations was increased to see what the highest accuracy that can be obtained is. However, there were no observable improvements in accuracy in the training set after 400 iterations, and the time needed increased rapidly. Other optimizations for logistic regression will be explored depending on the results obtained by the random forest classifier.

The model does not seem to improve with more training examples (**Figure 1**), and the cross-validation score even seems to decrease at some stages. The decrease in accuracy is quite unexpected for the same data set as in general the accuracy should increase with more training examples. This points to the limitations of the model itself, not the number of training examples. After the main parameters were selected, the final accuracy achieved was 0.7141, and the Fβ score was 0.6990. We next investigated random forest in order to compare the results to this model.

Criterion	Time needed (s)	Accuracy
Gini	102	0.9598
entropy	102	0.9625

Table 3: Accuracy results for the different criteria for the same amount of time for a fair comparison.

Cover	Accuracy	Number of samples
1	0.9696	211840
2	0.9808	283301
3	0.9740	35754
4	0.8998	2747
5	0.8750	9493
6	0.9317	17367
7	0.9667	20510

Table 4: Accuracy results for each cover type as well as the number of samples for each cover type. The table presents a clear relationship between the accuracy and number of samples

The first decision for creating a model was the selection of the random forest criterion. The accuracies obtained only differ by 0.025 between the two criteria, Gini and entropy, (**Table 3**). So, the entropy criterion was used for the final model as even such a small change may result in a higher final accuracy for the model.

The learning curves show that when more data is supplied, the accuracy is increased (**Figure 2**). The training score was compared to the cross-validation score. As expected, the cross-validation scores were lower than the training scores. Hence, using more data points would increase accuracy, but it is not a valuable use of time because it could be used for other purposes (e.g., exploring alternative models or more hyperparameter tuning).

The accuracy consistently increased with more decision trees (**Figure 3**) up until about 50 trees, where it leveled off. Using more than a hundred decision trees provides negligible improvements, with no improvements observed after 400 decision trees.

Next, hyperparameter tuning was performed to see its benefits. This was done as random forest already had better baseline results than logistic regression, so, a decision was made to try and improve it with hyperparameter tuning. As a baseline, a RandomForestClassifier was run several times

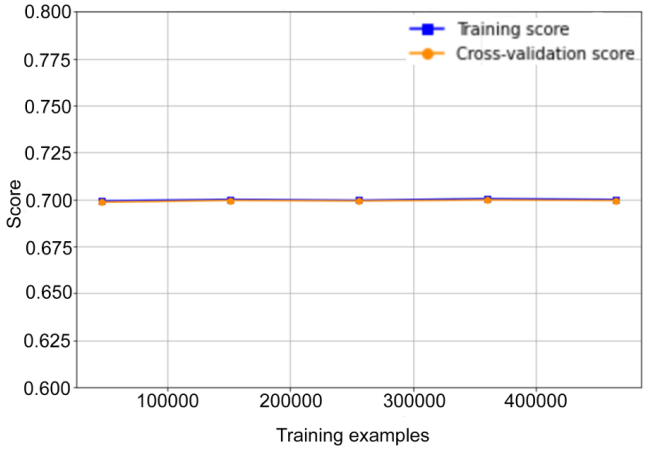

Figure 1: Learning curve for the sag solver (logistic regression). Accuracy plotted against the number of training examples supplied, which shows how the model can become more accurate with more data provided to it.

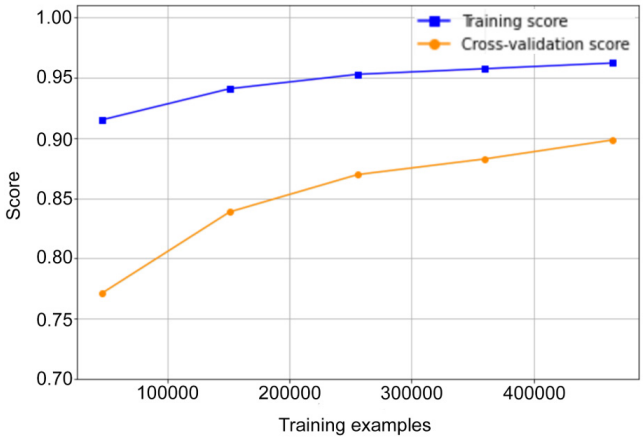

Figure 2: Learning curve for random forest. Accuracy plotted against the number of training examples supplied, which shows how the model can become more accurate with more data provided to it.

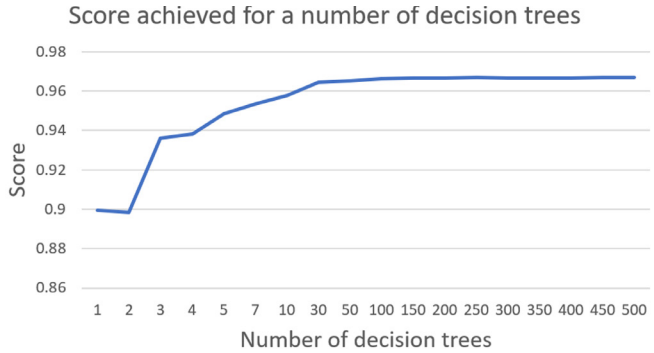

Figure 3: Accuracy plotted against a given number of decision trees. More decision trees should result in a higher accuracy as it reduces the variance by averaging the results from several trees, preventing overfitting.

with only the random state set to 0 and no other parameters set, and its accuracy was on average 0.9635. This result was then compared to the results from the hyperparameter tuning.

The final accuracy was on average 0.9720, which is only a marginal improvement over the baseline; however, it is still an improvement as all of the final accuracy tests yielded higher results than any of the baseline tests. For a more objective measure of accuracy, the Fβ score was used to assess the final model, as it accounts for any imbalances in the dataset, which is the case in this investigation. An accuracy value of 0.97217 was achieved. This means that random forest was more accurate than logistic regression in both measures.

When compared to the distribution of the cover types in the dataset (**Table 4**), a clear trend can be seen: the more training examples there were for a cover type, the higher the accuracy for that cover type was.

Overall, the baseline random forest model (0.9635) had significantly greater accuracy than the logistic regression model (0.7141) even with the solvers investigated. Furthermore, hyperparameter tuning provided a significant increase in accuracy from the baseline model (0.97217). To increase the performance of logistic regression, significantly more effort would have to be put into the model and the data itself, which goes against the ease of use criterion set out in this investigation while comparing the two models. The results lead to the rejection of the hypothesis.

DISCUSSION

When faced with a new dataset, such as the forestry one in this investigation, it is often difficult to decide which model to use. Although each dataset is unique, the basic use of models for multivariate classification is roughly the same for each case. The aim of this investigation was to determine which method would be easier to use while also yielding high accuracy. In the beginning, higher accuracy results were expected from logistic regression, however, it massively underperformed in comparison to random forest in both of the criteria that were set (accuracy and ease of use).

In our investigation, random forest needed less pre-processing of the data for it to yield high accuracy. A logistic regression model would need much more manual data pre-processing, such as feature selection including multicollinearity analysis to reach comparable accuracy levels (8). As a random forest uses a subset of the available features for each tree, it may remove features that are highly correlated to each other, increasing the overall accuracy. For a logistic regression model, this correlation analysis would have to be done manually and before the training. Not doing that may make the learning of the model slower or introduce harmful bias. Using a random forest prevents these issues. Furthermore, logistic regression attempts to fit a linear model to the data. A model may perform better if it is a polynomial model, which can be done by squaring one of the features, for instance. All these issues must be resolved manually for logistic regression and they do not concern random forest.

The dataset used in this investigation was relatively large with a small number of features. The accuracies for the different solvers (**Table 1**), considering the number of iterations, accuracy, and time needed, can then easily be explained for this dataset. In the case of newton-cg, it uses an exact Hessian matrix to optimize the model, which explains

	Elevation	Aspect	Slope	Horizontal hydrology	Vertical hydrology	Horizontal roadway	Hillshade 9am	Hillshade noon	Hillshade 3pm	Horizontal fire	Cover	Soil Type	Area
Elevation	1.000000	0.015735	-0.242697	0.306229	0.093306	0.365559	0.112179	0.205887	0.059148	0.148022	-0.269554	0.689848	-0.315590
Aspect	0.015735	1.000000	0.078728	0.017376	0.070305	0.025121	-0.579273	0.336103	0.646944	-0.109172	0.017080	0.007149	0.138703
Slope	-0.242697	0.078728	1.000000	-0.010607	0.274976	-0.215914	-0.327199	-0.526911	-0.175854	-0.185662	0.148285	-0.105571	0.286178
Horizontal hydrology	0.306229	0.017376	-0.010607	1.000000	0.606236	0.072030	-0.027088	0.046790	0.052330	0.051874	-0.020317	0.194685	0.056339
Vertical hydrology	0.093306	0.070305	0.274976	0.606236	1.000000	-0.046372	-0.166333	-0.110957	0.034902	-0.069913	0.081664	0.071313	0.189085
Horizontal roadway	0.365559	0.025121	-0.215914	0.072030	-0.046372	1.000000	0.034349	0.189461	0.106119	0.331580	-0.153450	0.240829	-0.445922
Hillshade 9am	0.112179	-0.579273	-0.327199	-0.027088	-0.166333	0.034349	1.000000	0.010037	-0.780296	0.132669	-0.035415	0.040877	-0.233455
Hillshade noon	0.205887	0.336103	-0.526911	0.046790	-0.110957	0.189461	0.010037	1.000000	0.594274	0.057329	-0.096426	0.013662	-0.080767
Hillshade 3pm	0.059148	0.646944	-0.175854	0.052330	0.034902	0.106119	-0.780296	0.594274	1.000000	-0.047981	-0.048290	-0.001122	0.105050
Horizontal fire	0.148022	-0.109172	-0.185662	0.051874	-0.069913	0.331580	0.132669	0.057329	-0.047981	1.000000	-0.108936	0.100952	-0.416830
Cover	-0.269554	0.017080	0.148285	-0.020317	0.081664	-0.153450	-0.035415	-0.096426	-0.048290	-0.108936	1.000000	-0.164337	0.275464
Soil Type	0.689848	0.007149	-0.105571	0.194685	0.071313	0.240829	0.040877	0.013662	-0.001122	0.100952	-0.164337	1.000000	-0.271883
Area	-0.315590	0.138703	0.286178	0.056339	0.189085	-0.445922	-0.233455	-0.080767	0.105050	-0.416830	0.275464	-0.271883	1.000000

Figure 4: Correlation table for the variables included in the dataset. The correlation between any two variables was calculated to determine which variables contribute the most towards the dependent variable and which variables are collinear.

the small number of iterations needed to converge as well as the high accuracy; however, it also makes the calculations more computationally expensive. The key difference between newton-cg and lbfgs is that lbfgs uses an approximate Hessian matrix, making it less computationally expensive. However, this explains the need for more iterations. It does not generally perform well on larger datasets.

Sag works differently to newton-cg and lbfgs. It minimizes finite sums of convex functions and it is one of the fastest solvers for large datasets (number of data points and the number of features is both large). As our dataset does not have many features, this might be the reason for the lower-than-expected performance. However, the dataset had many data points, meaning it performed better than lbfgs. Saga works similarly to sag: it is a variation of sag which supports L1 regularization. It supports sparse datasets (the one in the case study was not), as well as very large data sets (the one in the case study was not). Although secondary sources seem to suggest that saga should, in general, be faster than sag, the empirical evidence does not support such a conclusion for the case study, which may be due to the reasons outlined.

A random forest without any hyperparameter tuning was already much more accurate than any of the above solvers, and so that was the model with more tuning put into it. This is why random forest was focused on more during the end of the investigation.

The models tested in this investigation were chosen because they are fundamentally different. However, a similar investigation can be carried out on any two other models, such as support vector machines and neural networks, which are also two very different approaches. Neural networks promise to increase the accuracy obtained, as they can combine many features to produce more features by themselves, which also means that they can be easy to use. However, this discussion is beyond the scope of this investigation.

METHODS

Dataset

For this investigation, we used a forestry dataset (7). This dataset was used to predict cover types for forests using cartographical variables. 30x30 meter blocks of these forests are used for these cover types as this can be more easily controlled. These 30x30 meter areas also represent forests with minimal human-caused disturbances, so that existing forest cover types are more a result of ecological processes rather than forest management practices. The independent variables were derived from data originally obtained from the US Geological Survey (USGS) and US Forest Service (USFS) data. Data is not scaled and contains binary columns for qualitative independent variables (e.g., wilderness areas and soil types).

The variables included in the dataset included information such as: Elevation, Aspect, Slope, Horizontal and vertical distance to hydrology, Horizontal distance to roadways, Hillshade indexes at different times of the day, Horizontal distance to fire points, Wilderness area (4 binary columns), Soil type (40 binary columns), Cover type (7 types). More detailed descriptions of each variable are included in the dataset (9).

Data pre-processing and pre-analysis

The data was supplied in a comma-delimited data format. Columns were labeled with their corresponding names, and

values were identified as either continuous or discrete. The file was then exported into a .csv format to conform with Pandas (Python data framework library).

Soil type columns were merged into a single column with 40 different categories possible, labeled from 0 to 39. This was done via a short script which first detected the number of the column selected (which indicated which soil type the area has) and then entered that number into a new column. The same process was repeated with the wilderness area: merging 4 binary columns into one label column.

The correlation values between all of the variables in the dataset were calculated (**Figure 4**). This allowed us to determine the variables that most significantly impacted the cover type, which were: elevation, slope, horizontal roadway, horizontal fire, soil type, and area. The highest correlation value was 0.2755 between cover and area, which is not a high value, implying that none of the independent variables are highly correlated to cover. For training, all of the independent variables were used, as there was a small number of them, and none were highly correlated to cover. Reducing the number of independent variables could affect the methodology due to underfitting or having a lower accuracy in general.

The data is not equally distributed between the cover types, with type 2 being the most common and type 1 being slightly behind. The frequency of type 1 is two orders of magnitude larger than of type 4 (211840 vs 2747 data points), which skewed the results. So, this needed to be accounted for in the models to get the fairest and most accurate results as possible.

The data was randomly split into training and test data sets in a ratio of 70:30. This ratio was decided based on the size of the dataset (m=581013), which allowed for a large proportion of the examples to be left for testing purposes. Both models used the same sets of data to ensure that the variance was low, and any anomalies were shared across both, so neither would have an advantage over the other during testing. Using training data to assess the performance of the algorithms would not yield reliable results as it would not provide an accurate assessment of performance on unseen data.

Multivariate logistic regression

To test our hypothesis, we need to determine both how accurate and easy to use each model is for predicting the cover type in the forestry dataset. The first model tested was logistic regression and how different solvers for it performed. The tests were implemented to find the accuracy of each solver, while also noting the time taken for the accuracy to reach a certain threshold for a fair comparison. This was done by first inputting the train and test data to find the respective accuracies with a limited number of iterations (7). Then the accuracies were measured after a certain time to determine which solver yielded better accuracies given the time constraints. These limitations were set to keep variables constant and to check for the efficiency of each solver with the data set, which ultimately concluded which would be more accurate and easier to use.

Each model in scikit-learn has a random state parameter that is used as the seed for the random number generator. Throughout the whole investigation, it was set to the same value. This ensures that any improvements observed are not due to random variation, but only due to the changes made to the model.

Python's sklearn logistic regression model has a variety of different algorithms for gradient descent. In the documentation, it is recommended to use newton-cg, sag, saga, or lbfgs (liblinear is possible, however, limited to one-versus-rest models). The different solvers were benchmarked against each other to compare their performance in terms of speed and accuracy. To provide reliable results, the number of iterations was limited to a fixed number of 100 epochs. The measurements were then repeated after normalizing the data, as sag and saga require normalization for optimal performance (5). The results for each solver are summarized in **Table 1**.

For the same number of iterations, the time taken for the optimization to complete varied greatly, and even though these results give some insight as to which solver is the most appropriate one for this case study, the control variable chosen was not giving comparable results because more time (and so computational power) to optimize the data naturally results in higher accuracy. This is why the control variable was switched to the time needed (around 127 seconds given for each solver, chosen arbitrarily) as it would give a better measure to compare the solvers.

No solver had an obvious advantage over the others in terms of accuracy, so sag was used as the solver for the final model due to the scalability for large datasets that it promises. There is no need to use saga in this investigation due to the limited number of features and no missing data points.

The train and test scores for a different number of training examples were very close to each other or even the same in some cases (**Figure 1**). Cross-validation was performed over 10 different splits of the part of the dataset under consideration (dependent on the number of training examples for each point), with 80% of the dataset going towards training and 20% towards testing for each split, in contrast to the training-testing split. As the dataset is large, more data points can be used for training in this case, and less for testing. This smoothed out any variation in the data supplied to the model and provided a more reliable method of assessing the accuracy of the model. The cross-validation score was calculated from the data that the model had not seen before, which better reflects a real-life scenario.

Random forest classifier

A random forest classifier is a collection of decision trees that are fit on sub-samples of the whole dataset and averages their results to improve accuracy. Each tree continuously splits its data into smaller and smaller groups according to the values of their parameters, until a result is obtained from

a leaf node. A random forest was used instead of a decision tree due to how easily a decision tree can overfit the data (high variance), yielding a higher accuracy while training but a lower accuracy in test data. A random forest negates this tendency by training a specified number of decision trees, which 'spreads out' the results to several different trees. Like logistic regression, the random forest model was created using sklearn's ensemble package.

The Gini coefficient measures the inequality among values of a frequency distribution. It can also be replaced by an entropy measure, which is the information gain. So, the impact of the criterion on the given accuracy for a set time was measured.

The accuracy for a different number of training examples was then investigated (**Figure 2**), which showed promising results. Cross-validation scores were calculated in the same way as in the learning curves for logistic regression.

As a random forest consists of several decision trees, the relationship of the number of trees to the accuracy was graphed (**Figure 3**), which showed an increase in accuracy up to a certain number of trees. This helped determine the value of the number of estimators parameter in hyperparameter tuning.

Hyperparameter tuning

As random forest was used for the final model, the values of the parameters available were tweaked (6):

- n_estimators – It is the number of decision trees that need to be trained. The more, the better; however, it is also more computationally expensive. The selected value was 400, as values above this one gave negligible improvements to the accuracy of the model.
- criterion – It is the function measuring the quality of the split. The data gathered (Table 3) about the performance of each criterion suggests a higher accuracy while using this entropy criterion.
- max_depth – It is the measure of how deep a tree can go before a leaf node is reached. A value of 'None' means the tree will be expanded until the leaves are pure (or have fewer than min_samples_split samples, if specified). This was the optimal value found as it did not produce overfitting in the testing set while giving the model a large depth, preventing underfitting.
- min_samples_split – It is the minimum number of samples needed to split a node. A value of 2 was chosen as this is a good in-between value (and recommended by scikit-learn as the default value). This value lies in the ideal range of 1 to 40, as found by empirical methods (10).
- min_samples_leaf – This is the minimum number of samples needed to be a leaf node. The value of 1 was chosen because a split must result in at least one sample being left. Using any higher values may decrease the accuracy. This is also the value recommended by scikit-learn.
- min_weight_fraction_leaf – This is only applied if the samples are given weights. It comes from the sum of weights of samples at a leaf node and is the minimum weighted fraction of those. For our model, this value was kept at 0.0, as each class has an equal weight.
- max_features – This is the measure of how many features can be considered for a split. It is made to be 'auto' as this value makes the max_features equal to the square root of the number of features as this is a good in-between value.
- max_leaf_nodes – This is the maximum number of leaf nodes a tree can have, which reduces impurity. The value of 'None' has been kept, as this won't limit the number of leaf nodes; it is recommended by scikit-learn.
- min_impurity_decrease – a node can only be split if the split decreases the impurity of a node by that amount or more. It is kept at 0.0 (recommended value), as specifying a minimum decrease in impurity may increase the accuracy; however, it may also cause overfitting.
- bootstrap – This is used in order to determine whether the bootstrap samples need to be used when training a tree. The final model kept this value as 'False', as doing so may increase overall accuracy at the cost of an increase in time needed for training.
- oob_score – This determines whether out-of-bag samples are used to estimate the accuracy. The final model kept this value as 'False', as the final model does not need to estimate the generalization accuracy
- n_jobs – This is the number of jobs that need to run in parallel. A value of -1 was used as this causes all processes to be used, optimizing the model faster.
- random_state – This is used in order to control the randomness when training a tree (keeps random choices of e.g., sampling of features) the same for each optimization of the tree. The final model kept this value as at '0' for a fair comparison between the models.
- verbose – This controls verbosity, The final model kept this value as at the recommended value of 0.
- warm_start – This is used to determine whether to reuse the model from the previous call of the model and add to it. This was not used for the final model, so a value of 'False' was specified.
- class_weight – This is the weight associated with the classes in the data. The final model kept this as not specified, as all our classes have equal weight.
- ccp_alpha – this is used for Minimal Cost-Complexity Pruning, it is the complexity parameter. This value was kept at 0.0 as the final model will not perform pruning.
- max_samples – (if bootstrap is 'True') This is how many samples to get from the training dataset for each estimator. As the bootstrap is kept at 'False', it is not needed.

Final model

The final model included all the parameter values decided in hyperparameter turning. A detailed breakdown of the accuracies obtained is presented in **Table 4**.

ACKNOWLEDGMENTS

We would like to thank the NTT Data Chennai IT team for teaching us machine learning as well as for helping us write the paper.

Received: August 24, 2020
Accepted: February 6, 2021
Published: March 21, 2021

REFERENCES

1. Samuel, A. L. “Some Studies in Machine Learning Using the Game of Checkers.” *IBM Journal of Research and Development*, vol. 3, July 1959, pp. 210–229.
2. Mitchel, T. M. Machine Learning. Vol. 1, *McGraw-Hill*, 1997.
3. Desmond07/23/2019, Michael. “Machine Learning Market to Grow to Nearly $21 Billion by 2024.” Pure AI, 23 July 2019, pureai.com/articles/2019/07/23/nwsdes-machine-learningmarket-growth.aspx, Accessed 16 December 2019.
4. Pedregosa, F. *et al.* "Scikit-learn: Machine Learning in Python". *Journal of Machine Learning Research* 12. (2011): 2825–2830.
5. Documentation of logistic regression: F, Pedregosa. “Sklearn.linear_model.LogisticRegression.” Scikit, *Journal of Machine Learning Research*, Dec. 2011, scikit-learn.org/stable/modules/generated/sklearn.linear_model.LogisticRegression.html, Accessed 4 January 2020.
6. Pedregosa, F. “Sklearn.ensemble.RandomForestClassifier.” Scikit, Dec. 2011, scikit-learn.org/stable/modules/generated/sklearn.ensemble.RandomForestClassifier.html, Accessed 4 January 2020.
7. Dua, D. "UCI Machine Learning Repository [http://archive.ics.uci.edu/ml]." *Irvine, CA: University of California, School of Information and Computer Science*. n.p.: n.p., 12 . 22 Jan. 2021, Accessed 17 January 2020.
8. Midi, Habshah, et al. “Collinearity Diagnostics of Binary Logistic Regression Model.” *Journal of Interdisciplinary Mathematics*, vol. 13, no. 3, 2010, pp. 253–267., doi:10.1080/09720502.2010.10700699.
9. Descriptions and types of variables included in the dataset: “Https://Archive.ics.uci.edu/Ml/Machine-LearningDatabases/Covtype/Covtype.info.” Index of /Ml/MachineLearning-Databases/Covtype, archive.ics.uci.edu/ml/ machine-learning-databases/covtype/, Accessed 17 January 2020.
10. Mantovani, Rafael Gomes Mantovani Gome, et al. “An Empirical Study on Hyperparameter Tuning of Decision Trees". 5th *Brazilian Conference on Intelligent System - BRACIS 2016*.”

JOURNAL OF
EMERGING INVESTIGATORS

Article

High-throughput virtual screening of novel rilpivirine analogs as next-generation antiretroviral therapeutics

Jeslyn Wu[1,2], Charissa Luk[1,3], Catherine Zhou[1,4], Aashi Shah[1,5], Aishwarya Yuvaraj[1,6], Edward Njoo[1]

[1] Aspiring Scholars Directed Research Program, Fremont, CA
[2] Mission San Jose High School, Fremont, CA
[3] Bishop O'Dowd High School, Oakland, CA
[4] Lynbrook High School, San Jose, CA
[5] Amador Valley High School, Pleasanton, CA
[6] American High School, Fremont, CA

SUMMARY

Part of the retroviral genus, the human immunodeficiency virus (HIV) relies on the host's cellular machinery for replication. The viral genetic material is composed of ribonucleic acid (RNA) which, upon delivery into the host's cells, is reverse transcribed into deoxyribonucleic acid (DNA) by the viral enzyme reverse transcriptase (RT). This is then used for the production of new viral components, thus allowing for further replication and spread of HIV. Because this virus selectively targets CD4+ T cells, the infection inevitably leads to weakening of the host's immune system, which can then lead to acquired immunodeficiency syndrome (AIDS). One treatment for HIV is non-nucleoside reverse transcriptase inhibitors (NNRTIs), which are allosteric inhibitors of RT that disable the enzyme's activity and thus viral replication. Previous NNRTIs approved for clinical use by the United States Food and Drug Association (FDA) include etravirine, doravirine, and rilpivirine. However, resistance to these drugs through mutations in RT necessitates the continued development of NNRTIs. Here, the structure of rilpivirine, a relatively recently FDA approved NNRTI, was used to design a library of analogs that were then evaluated in silico via high-throughput virtual screening (HTVS). From this, several structures were identified as potential next-generation NNRTIs with comparable predicted binding affinities to the allosteric binding pocket in RT as rilpivirine.

INTRODUCTION

As of 2019, approximately 38 million people across the globe have human immunodeficiency virus/acquired immunodeficiency syndrome (HIV/AIDS) (1). Without any treatment, the retrovirus can replicate billions of times a day to quickly weaken the immune system of the host and eventually cause AIDS. The virus weakens a system by selective targeting the CD4+ T cells of the host. A person is considered to have progressed to AIDS when their CD4+ T cell count is lower than 200 cells per cubic millimeter of blood (cells/mm^3). For reference, the CD4+ T cell count ranges from 500 to 1,600 cells/mm^3 in a person with a healthy immune system. This loss of the host's CD4+ T helper cells results in the destruction and functional impairment of the immune system. HIV/AIDS often prove fatal for patients because opportunistic illnesses (OIs) and cancers that are usually controlled in immunocompetent people can become serious fatal threats to those with a weakened immune system. Enabling accessible HIV treatment for all is the key to ending AIDS as a public health threat as well as the only viable way infected individuals can live longer and healthier lives (2).

Current treatments are called antiretroviral therapy (ART), combination therapy, and highly active antiretroviral therapy (HAART) because of the utilization of at least two HIV drugs meant to treat the infection (3). With treatment, people are able to live normally and avoid AIDS. One class of drugs used is non-nucleoside reverse transcriptase inhibitors (NNRTIs), which are allosteric inhibitors of the reverse transcriptase (RT) enzyme in HIV. The process of viral replication and spread relies on the transformation of viral RNA into DNA that then allows viral reproduction within host cells. The RT enzyme is vital to the viral reproduction system. As allosteric inhibitors, NNRTIs effectively block the enzyme from converting viral RNA into DNA by binding at a region of RT that configures the enzyme to perform worse. In RT, this then prevents HIV from further replication (4).

The first generation NNRTIs are nevirapine, delavirdine, and efavirenz (5, 6, 7) (**Figure 1**). This generation proved to have decent efficacy relative to preceding treatments; however, errors like delavirdine's ineffectiveness on its own proved to be setbacks as it required the usage of multiple drugs combined. These compounds all have a low genetic barrier to resistance, meaning a single mutation in the RT sequence can lead to effective drug resistance (8, 9). Consequently, the second generation of NNRTIs, etravirine and rilpivirine, were designed to better combat RT mutations. Compared to the first generation of NNRTIs, these drugs showed stronger inhibitory activity, especially against the HIV mutations that caused first generation NNRTIs to be less successful (10). Additionally, doravirine, a part of the newest generation, has also been recently FDA approved (11, 12).

Currently, only the six aforementioned NNRTIs shown in **Figure 1** (nevirapine, delavirdine, efavirenz, etravirine, rilpivirine, and doravirine) have been approved by the FDA. The development of these drugs has evolved greatly over the past 30 years and further investigation into synthesis will be essential to the discovery of the next generation of cost-effective NNRTIs (13).

The rapid drug-resistant mutations in HIV-1 RT, dose-limiting toxicity, and unfavorable pharmacokinetic properties

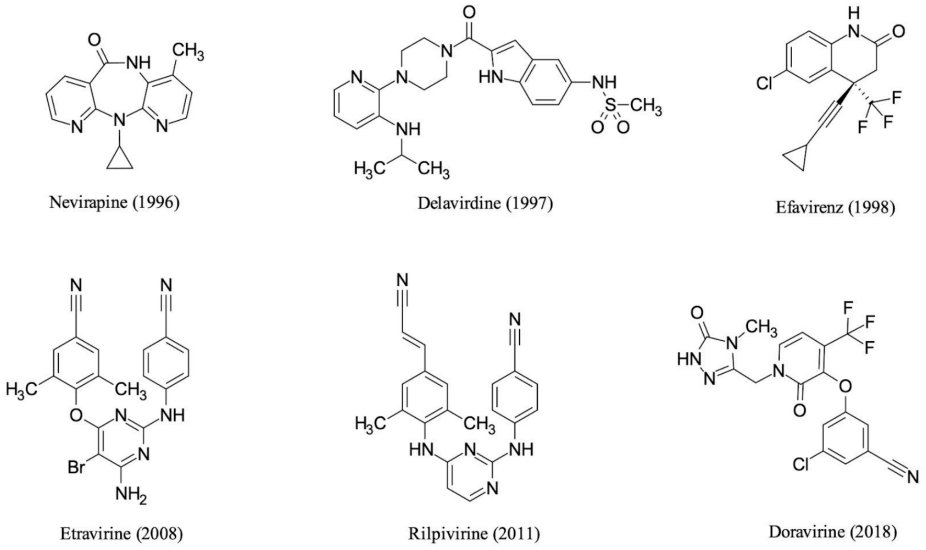

Figure 1: Chemical structures of FDA-approved NNRTIs. The six NNRTIs currently approved by the FDA are nevirapine, delavirdine, efavirenz, etravirine, rilpivirine, and doravirine.

should be considered and avoided for effective anti-HIV therapy. In order to account for these problems, structural mimics of a range of scaffolds or peripheral substituents are possibilities of promising inhibitors for HIV-1 RT; however, these methods are still not fully effective. Structure-based bioisosterism was also previously attempted in NNRTI development (14). Such NNRTIs include piperidine-substituted thiophene[2,3-d]pyrimidine derivatives, which were shown to have high resistance profiles, improved solubilities, lower cytochrome liabilities, and human ether-a-go-go gene inhibition, making them potent inhibitors in the MT-4 cells line (15). These studies determined that the effective properties mainly include structural flexibility and numerous hydrophobic interactions to form a H-bond (hydrogen bond) network with the NNRTI binding pocket. Overall, these properties account for increased activity against cross resistance-associated mutations.

Specifically, rilpivirine, a second-generation NNRTI, has higher potency, a longer half-life, and relatively fewer side effects compared to other NNRTIs. Rilpivirine is a diaryl pyrimidine (DAPY) compound with a butterfly conformation (16). DAPY analogues, with a characteristic "horseshoe" or "U-shape" structure, have been studied extensively over the past two decades for their high potency and relatively low cytotoxicity (17). Furthermore, they are active against wild-type viruses and retain activity against previous NNRTI-resistant HIV-1 strains *in vitro*. The internal conformational flexibility of rilpivirine as well as the plasticity of the interaction between rilpivirine and the NNRTI-binding site of HIV RT allows the compound to bind in different modes, giving it greater tolerance to binding pocket mutations in RT (18), which contains lysine, phenylalanine, tryptophan, and tyrosine. The tryptophan, phenylalanine, and tyrosine residues in the NNRTI binding pocket are able to form aromatic-aromatic interactions that are no more than 7 Å in distance with an inter-plane angle between 30° to 90° (19). Three types of interactions can be found with aromatic systems: π-π, cation-π, and X-H-π, where X is carbon, oxygen, nitrogen, boron, or a halogen like fluorine, chlorine, or bromine. There are four general types of aromatic π-π interaction geometries: face-to-face (sandwich), parallel-displacement, T-shaped, and edge-to-face; however, face-to-face is not favorable and thus is rarely observed. Lysine and arginine are generally able to form polar cationic-π interactions within 6 Å.

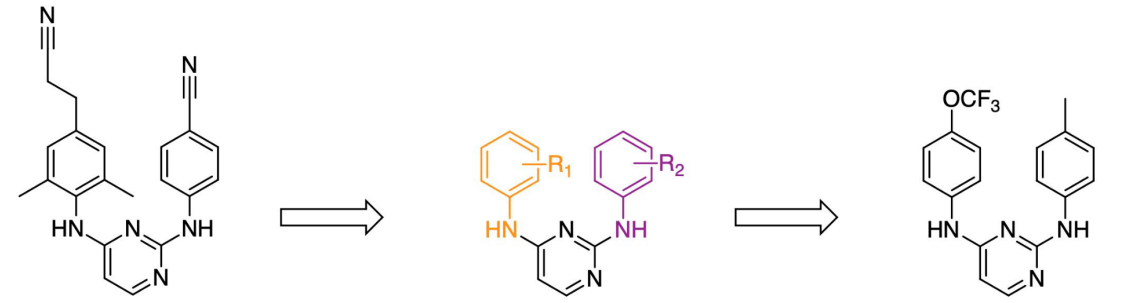

Figure 2: Design and core scaffold of the library of our structural analogs of rilpivirine. Starting from rilpivirine (left), the base structure of all analogs is created. Screening then identifies analogs with the best activity, one of which is drawn (right).

Modern advances in computational modeling have allowed for high-throughput virtual screening (HTVS) of vast compound libraries much more rapidly than can be synthesized and evaluated for potential biological activity in a laboratory. We proposed that this approach could be used to develop structural analogs to rilpivirine as potential next-generation NNRTIs. Here, we report the *in silico* design and HTVS of a library of 196 N,N-diarylpyrimidine-2,4-diamines as structural analogs of rilpivirine, which could conceivably be synthesized from a library of fragments and 2,4-dichloropyrimidine (**Figure 2**). Moreover, identified top analogs allowed us to hypothesize that analogs with better electron-withdrawing functionalities at the substituted positions (R1 and R2 in **Figure** 2) would return the highest predicted binding affinities due to their structural similarity to rilpivirine.

RESULTS

Substitutions at the 2 and 4 positions of the designed base analog allowed for 196 rilpivirine analogs to be computationally screened in a HTVS to simulate biological activity (**Figure 3**). Fragments chosen for the substitutions included various varieties differing in their electron withdrawing capabilities to potentially lead towards a conclusion on the most effective. Compounds 4G, 7D, 10D, 4E, and 7B produced the most favorable binding affinities. Compared to rilpivirine, which returned a predicted binding affinity of -12.7 kcal/mol by the same docking parameters, compounds with comparable and even better binding affinities were identified (**Figure 4**). These compounds further advance the research done on developing novel NNRTIs.

3MEE

The docking of our rilpivirine analogs to HIV-1 reverse transcriptase [PDB: 3MEE] (20) indicate that 4G, 7D, 10D, 4E, and 7B (12.8, 12.5, 12.5, 12.4, and 12.4 kcal/mol, respectively) have the highest binding affinities. These analogs bound with the known NNRTI binding pocket are visualized in **Figure 4** using Chimera (21).

4G: 4-trifluoromethoxy aniline fragment as R1 and 4-amino toluene fragment as R2

The binding affinity of rilpivirine to 3MEE is -12.7 kcal/mol, and 4G has a greater binding affinity of -12.8 kcal/mol. The methyl end of the R1 group, 4-amino toluene, forms a hydrophobic interaction with the aromatic ring of phenylalanine 227 at a distance of 4.30 Å. Glutamic acid 138 and lysine 103 are able to form relatively weak H-bond interactions with NH on R2 and R1 at distances of 4.39 Å and 3.84 Å, respectively. The trifluoromethoxy end of the R2 group, 4-trifluoromethoxy aniline, forms a halogen-π interaction with tyrosine 188 at a distance of 3.5 Å, and another halogen-π interaction with tryptophan 229 at a distance of 4.1 Å. The fluorine also forms an OH-F interaction, where OH, the hydroxyl end of tyrosine 188, is 3.75 Å away. The ring of the 4-trifluoromethoxy aniline fragment forms a π-π interaction with the aromatic ring of tyrosine 181 at a measured distance of 4.3 Å. Overall, these

R2 \ R1	1	2	3	4	5	6	7	8	9	10	11	12	13	14
A	-10	-11	-10.6	-11.2	-10.9	-10.5	-10.7	-10.4	-9.4	-10	-10.1	-4.8	-7.6	-4.8
B	-11.2	-10.5	-11.5	-11.9	-11.6	-9.6	-12.4	-10.4	-10.6	-11.8	-11.2	-7.2	-10.3	-8.9
C	-11.1	-11.6	-9.9	-11.7	-10.8	-11	-11.1	-11	-10.8	-10.3	-11.1	-9	-9.2	-7.9
D	-11.7	-11.5	-11.8	-11.5	-12.1	-11.6	-12.5	-11	-11.3	-12.5	-7.5	-4.1	-12	-7.9
E	-10.3	-11.6	-10.5	-12.4	-9.6	-10.4	-11.9	-10.6	-10.9	-10.8	-11.1	-8.3	-9.2	-8.1
F	-11.3	-10.9	-9.7	-11.6	-9.9	-9.9	-11.2	-10.9	-10.5	-10.3	-10.8	-9	-8.8	-7.8
G	-12	-12	-11.6	-12.8	-11.6	-11.3	-12.3	-10.9	-11.3	-11.9	-11.3	-10.8	-10.9	-9
H	-10.5	-10.2	-10.6	-10.9	-10.5	-10.8	-10.8	-10	-10.2	-10.6	-10.4	-10	-10	-9.8
I	-10.3	-10.4	-10.6	-11.2	-10.8	-10.4	-11.1	-10.1	-10.3	-10.9	-10.5	-9.9	-9.6	-9.4
J	-11.2	-11.3	-10.3	-10.3	-10.2	-10.2	-10.5	-10.7	-11	-10.4	-11.1	-9.1	-9	-8.4
K	-11	-10.9	-10.5	-11.5	-10.8	-9.7	-11.1	-10.3	-10.7	-10.9	-10.6	-8.7	-9.5	-8
L	-9.4	-9.6	-8.8	-9.7	-8.5	-8.6	-10.6	-9.9	-9.7	-8.9	-9.4	-7.4	-5.7	-5.4
M	-9.7	-9.9	-8.9	-10.4	-8.5	-8.6	-10.6	-10.1	-9.4	-9	-9.2	-5.9	-9.4	-5.6
N	-9	-9.5	-7.2	-8.3	-8.3	-8.1	-9.1	-9.8	-8.9	-7.5	-8.4	-5	-5.2	-5.5

Docking Key	≤ -12	-11.99 to -11	-10.99 to -10	-9.99 to -9	-8.99 to -8	≥ -7.99

Figure 3: Computational screening results as a table. Heat map of structure-activity relationship (SAR) of predicted binding affinities in kcal/mol generated from molecular docking simulations of targeted rilpivirine analogs to reverse transcriptase (PDB:3MEE). Lower binding affinities signify higher biological activity. Calculated binding affinities are reported in kcal/mol for each aryl substitution pattern (R1, x-axis; R2; y-axis) on the core analog scaffold and are color coded according to the key shown. Under the same docking parameters, rilpivirine returned a binding affinity of -12.7 kcal/mol.

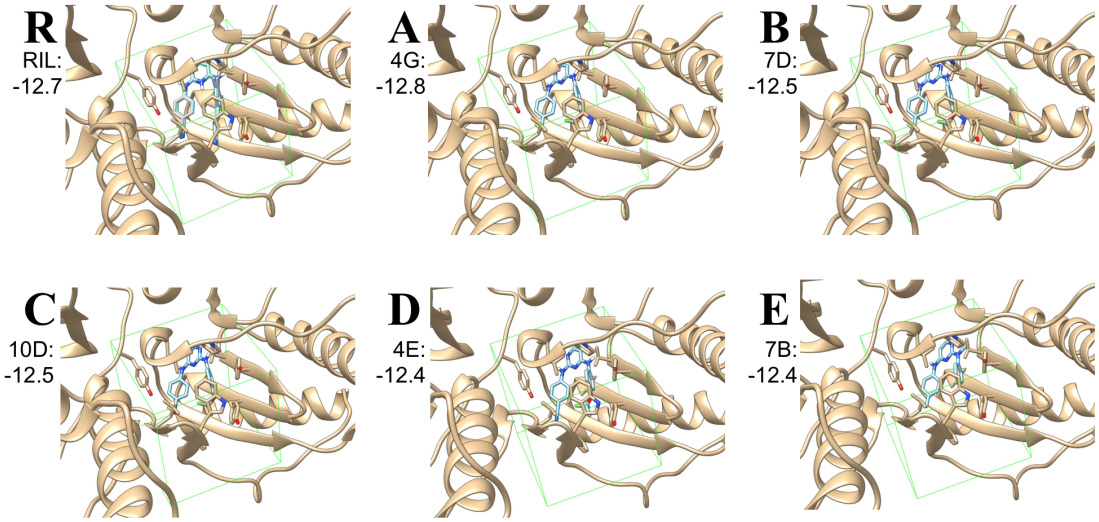

Figure 4: Identified hit analogs. The top five docked analogs as compared to rilpivirine docked to the same PDB with the same parameters. The shown analogs are labeled as follows: R: Rilpivirine layered with the original PDB, A: 4G. B: 7D, C: 10D, D: 4E, E: 7B.

extensive aromatic and hydrophobic interactions contribute to the high binding affinity of 4G.

7D: 4-amino toluene fragment as R1 and 4-trifluoro-methoxy aniline fragment as R2

The methyl end of the R1 group, 4-amino toluene, interacts in a hydrophobic interaction with the aromatic ring of phenylalanine 227 with a distance of 4.25 Å. Again, the R1 and R2 NH form weak electrophilic hydrogen interactions with glutamic acid 138 and lysine 103 at distances of 4.60 Å and 3.95 Å, respectively. These distances are farther than those seen in 4G, which has the same fragments in opposite positions but a higher binding affinity; therefore, this decrease in H-bonds is a probable cause for 7D's lower binding affinity compared to 4G. Additionally, a π-π interaction occurs between the R2 group, 4-trifluoromethoxy aniline, and tyrosine 183 at a distance of 4.3 Å. The trifluoro end forms the same interactions as those in 4G at relatively similar distances. Likewise, aromatic and hydrophobic interactions improve binding score like in 4G; however, weaker H-bonds contribute to 7D's relatively lower binding affinity compared to 4G.

10D: 4-bromoaniline fragment as R1 and 4-trifluoro-methoxy aniline fragment as R2

The brominated end of the R1 group, 4-bromoaniline, forms a halogen-π interaction with the aromatic phenylalanine 227, with a distance of 4.01 Å. The bromine also forms a halogen-hydroxyl interaction with the OH end of tyrosine 318 at a distance of 4.43 Å. Glutamic acid 138 and lysine 103 are able to form relatively weak H-bond interactions with NH on R1 and R2 at distances of 4.34 Å and 3.79 Å, respectively. The trifluoromethoxy end of the R1 group, 4-trifluoromethoxy aniline, forms one halogen-π interaction with tyrosine 188 at a distance of 3.6 Å and another halogen-π interaction with tryptophan 229 at a distance of 4.0 Å. The fluorine also forms an OH-X (where X is a halogen, in this case fluorine) interaction, where OH, the hydroxyl end of tyrosine 188 is 3.72 Å away. The ring of 4-trifluoromethoxy aniline forms a π-π interaction with the aromatic ring of tyrosine 181 at a distance of 4.3 Å. Overall, 10D has two halogenated fragments, which contributes to its high binding affinity. Despite these two fragments, weaker interactions likely caused a lower score as compared to the previous two identified analogs.

4E: 4-amino benzonitrile fragment as R1 and 4-trifluoro-methoxy aniline fragment as R2

The R1 group, 4-aminobenzonitrile, interacts with phenylalanine 227 in the phenylalanine-proline part of the binding pocket 3.54 Å away. The 4-aminobenzonitrile ring forms a π-π interaction with the aromatic ring of tyrosine 318 at an angle of 48.8° and a distance of 5.1 Å. Glutamic acid 138 is able to form a relatively weak H-bond interaction with NH on R2 at a distance of 4.92 Å. The trifluoromethoxy end of the R2 group, 4-trifluoromethoxy aniline, forms a halogen-π interaction with tyrosine 188, at a distance of 3.5 Å, and another halogen-π interaction with tryptophan 229 at a distance of 4.2 Å. The fluorine also forms an OH-X (where X is a halogen, in this case fluorine) interaction, where OH, the hydroxyl end of tyrosine 188, is 3.72 Å away. The ring of 4-trifluoromethoxy aniline forms a π-π interaction with the aromatic ring of tyrosine 181 at a distance of 4.3 Å and an angle of 30.0°. 4E contains a fluorinated group which contributes to its high binding affinity and also a benzonitrile similar to that found in rilpivirine. Similar to 4E, weaker interactions likely caused a lower score.

7B: 4-amino toluene fragment as R1 and N-methylaniline fragment as R2

The R2 group N-methylaniline and aromatic tyrosine 181 forms a π-π interaction 4.3 Å away and at a 18.9° angle. The NH on R2 is able to form a NH-OH bond with the OH on glutamic acid 138 at a distance of 4.78 Å. The NH on R1 is able to form a relatively weak H-bond interaction with lysine 103 at a distance of 4.27 Å. The ring on R1, 4-amino toluene, forms a π-π interaction with the aromatic ring on tyrosine 318 at a distance of 5.5 Å and a dihedral angle of 45.8°.

DISCUSSION

Of the 196 rilpivirine analogs that were computationally

screened, we observed that analogs with a trifluoromethoxy group had a higher predicted binding affinity. This is in line with our original hypothesis relating higher binding affinities with better electron-withdrawing fragments. This activity can be rationalized with its high electron density and polarizability of the trifluoromethoxy fragment as well as fluorine's high electronegativity, high stability of the C-F bond in comparison to a C-H bond, and high lipophilicity. Additionally, trifluoromethoxy forms a halogen-π interaction with nearby tryptophan 229 and tyrosine 188, therefore improving binding affinity. This trend is supported by previous literature showing that the activity of other small molecule targets benefits from the addition of a halogen in the molecule (22). In this case, the fluorination of our analogs proved beneficial. The aniline ring also forms an aromatic π-stacking interaction with the aromatic amino acid tyrosine 181. The relatively low electron density pyrimidine ring forms strong electrostatic and H-bond interactions with glutamic acid 138 and lysine 103, both of which are charged residues at physiological pH. The methyl end of the ligand can also form CH-π interactions with aromatic phenylalanine 227. The docked position of each rilpivirine analog in the same allosteric binding site is visually shown (**Figure 4**).

Mutations in RT can arise from prolonged usage of NNRTIs. Thus, it is crucial to create analogs with improved potency against HIV-1 wild type and NNRTI-resistant strains. We plan to further study the binding affinity of our analogs compared to rilpivirine against clinically relevant mutant strains that confer NNRTI resistance, such as K101N, E138K, V179L, Y181C, Y188L and common double and triple mutants L100I/K103N, L100I/K103R/V179D, K103N/Y181C, V106A/Y181C through homology modeling (23).

This study's screening of analogs shows promising analogs for future NNRTIs compared to current NNRTIs, especially rilpivirine. The five top analogs from the docked library show similar trends in which attached R groups perform best. Either 4-trifluoromethoxy aniline and 4-amino toluene are present in all of the identified top analogs; the top two compounds, 4G and 7D, contain both of these fragments.

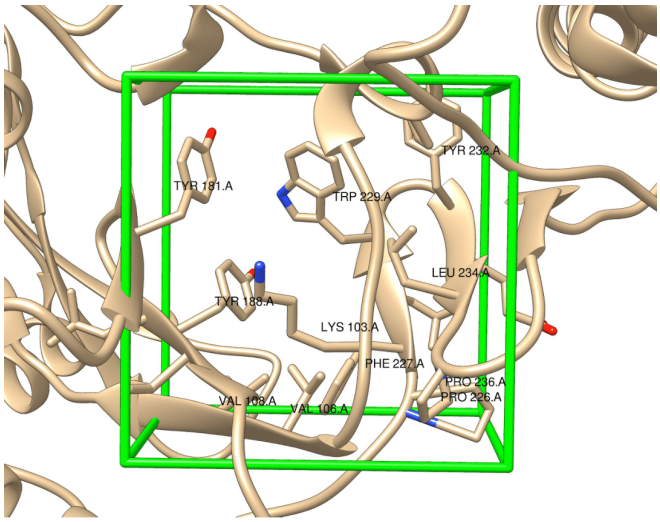

Figure 5: Computational parameters. Reverse transcriptase (PDB: 3MEE) with the docking parameters, a 16 by 16 by 16 Å box centered at the center atom of rilpivirine (9.200, 13.002, 20.250) visualized in green.

We hypothesize that the halogen in the trifluoromethyl group and the hydrophobic interactions caused by the toluene group account for their success. Further computational studies will focus on the nitrile group present in rilpivirine, which can be reproduced through usage of various benzonitriles. Efforts towards the chemical synthesis and *in vitro* evaluation of hit compounds from this screen on HIV-RT are additionally currently underway. Physical synthesis and biological assays will then test the efficacy of the analogs computationally predicted to have biological activity.

METHODS

Modeling, Design, and Molecular Mechanics Preoptimization

The library of rilpivirine analogs was systematically created and modeled using Avogadro (24), an open-source molecular modeling software package, through 2,4 substitution of a 2,4-dichlorinated pyrimidine with a selection of 14 anilines, whose structures are listed and pictured in **Figure 4**. These substitutions then allowed for the design of 196 analogs. All chemical entities screened in this study were initially optimized by molecular mechanics using the UFF94 force field at 10,000 steps.

Density Functional Theory (DFT)

Input files for rigorous quantum-mechanical optimization were created through Avogadro. The geometries of each structure were thermodynamically minimized via density functional theory (DFT) through ORCA (25), an *ab initio* quantum molecular modeling software, using a B3LYP functional and def2-SVP basis set with a continuum solvation model (CPCM) in water. All DFT calculations were performed on a Dell PowerEdge 710 server with a 24 core Intel Xeon X5660 processor at 2.80 GHz and 32 GB RAM.

Molecular Docking

With a batch script (26) submission to AutoDock Vina (27), optimized structures were docked to the allosteric binding pocket of RT to predict binding affinities of our designed analogs. The unliganded structure of rilpivirine bound to a representative reverse transcriptase of HIV [PDB:3MEE (20)] was used as the receptors and internal standard for comparison. The center atom of rilpivirine (9.200, 13.002, 20.250) was set as the center of a 16 by 16 by 16 Å grid box (**Figure 5**). Predicted binding modes were preliminarily judged through the value of free energy of binding (ΔG) in kcal/mol. The final binding poses were visualized through Chimera (21) before the final docking positions and protein-ligand interactions were analyzed to extract both predicted binding thermodynamics and the structural basis for such results (**Figure 3**).

ACKNOWLEDGEMENTS

We would like to thank the lab technicians for ensuring our safety and helping us resolve technical issues in the lab. We gratefully acknowledge the Olive Children's Foundation and its community of corporate sponsors and supporters for funding our research. Finally, we thank the Aspiring Scholars Directed Research Program for providing us with lab space to conduct research.

Received: October 31, 2020
Accepted: January 14, 2021
Published: March 22, 2021

REFERENCES

1. "The Global HIV/AIDS Epidemic." *HIV.gov*, 7 July 2020, www.hiv.gov/hiv-basics/overview/data-and-trends/global-statistics.
2. "What Are HIV and AIDS?" *HIV.gov*, 18 June 2020, www.hiv.gov/hiv-basics/overview/about-hiv-and-aids/what-are-hiv-and-aids.
3. "HIV Treatment: The Basics." (n.d.). 7 January 2021, https://hivinfo.nih.gov/understanding-hiv/fact-sheets/hiv-treatment-basics
4. Sharp, Paul M., and Beatrice H. Hahn. "The evolution of HIV-1 and the origin of AIDS." *Philosophical transactions of the Royal Society of London. Series B, Biological sciences*, vol. 365, no. 1552, 2010, pp. 2487-94. doi:10.1098/rstb.2010.0031
5. Usach, Iris *et al*. "Non-nucleoside reverse transcriptase inhibitors: a review on pharmacokinetics, pharmacodynamics, safety and tolerability." *Journal of the International AIDS Society*, vol. 16, no. 1, 4 Sep. 2013, pp 1-14. doi:10.7448/IAS.16.1.18567
6. Behja, W., and M. Jemal. "Anti-HIV Drug Discovery, Development and Synthesis of Delavirdine: Review Article". *International Research Journal of Pure and Applied Chemistry*, vol. 20, no. 3, 2019, pp. 1-16. doi:10.9734/irjpac/2019/v20i330137.
7. Mbuagbaw, Lawrence *et al*. "Efavirenz or nevirapine in three-drug combination therapy with two nucleoside or nucleotide-reverse transcriptase inhibitors for initial treatment of HIV infection in antiretroviral-naïve individuals." *The Cochrane database of systematic reviews*, vol. 12, no. 12, 2016, doi:10.1002/14651858.CD004246.pub4
8. Azijn, Hilde *et al*. "TMC278, a next-generation nonnucleoside reverse transcriptase inhibitor (NNRTI), active against wild-type and NNRTI-resistant HIV-1." *Antimicrobial agents and chemotherapy*, vol. 54, no. 2, 2010, pp. 718-27. doi:10.1128/AAC.00986-09
9. Buscher, A *et al*. "Impact of antiretroviral dosing frequency and pill burden on adherence among newly diagnosed, antiretroviral-naive HIV patients." *International journal of STD & AIDS* vol. 23, no. 5, 2012, pp. 351-5. doi:10.1258/ijsa.2011.011292
10. Minuto, Joshua J, and Richard Haubrich. "Etravirine: a second-generation NNRTI for treatment-experienced adults with resistant HIV-1 infection." *Future HIV therapy*, vol. 2, no. 6, 2008, pp. 525-537. doi:10.2217/17469600.2.6.525
11. Ludovici, D W *et al*. "Evolution of anti-HIV drug candidates. Part 1: From alpha-anilinophenylacetamide (alpha-APA) to imidoyl thiourea (ITU)." *Bioorganic & medicinal chemistry letters*, vol. 11, no. 17, 2001, pp. 2225-8. doi:10.1016/s0960-894x(01)00410-3
12. Hwang, Carey *et al*. "Rational Design of Doravirine: From Bench to Patients." *ACS infectious diseases*, vol. 6, no. 1, 2020, pp. 64-73. doi:10.1021/acsinfecdis.9b00178
13. Wang, Yali *et al*. "Current and emerging non-nucleoside reverse transcriptase inhibitors (NNRTIs) for HIV-1 treatment." *Expert opinion on drug metabolism & toxicology*, vol. 15, no. 10, 2019, pp. 813-829. doi:10.1080/17425255.2019.1673367
14. Kang, Dongwei *et al*. "Structure-Based Bioisosterism Yields HIV-1 NNRTIs with Improved Drug-Resistance Profiles and Favorable Pharmacokinetic Properties." *Journal of medicinal chemistry*, vol. 63, no. 9, 2020, pp. 4837-4848. doi:10.1021/acs.jmedchem.0c00117
15. Kang, D., Zhao, T., Wang, Z. *et al*. "Discovery of piperidine-substituted thiazolo[5,4-*d*]pyrimidine derivatives as potent and orally bioavailable HIV-1 non-nucleoside reverse transcriptase inhibitors." *Commun Chem*, vol. 2, no. 74, 2019, https://doi.org/10.1038/s42004-019-0174-8
16. Janssen, P. J. *et al*. "In search of a novel anti-HIV drug: multidisciplinary coordination in the discovery of 4-[[4-[[4-[(1E)-2-cyanoethenyl]-2,6-dimethylphenyl]amino]-2- pyrimidinyl]amino]benzonitrile (R278474, rilpivirine)." *Journal of medicinal chemistry*, vol. 48, no. 6, 2005, pp 1901-9. doi:10.1021/jm040840e
17. Chen, Xuwang *et al*. "Recent advances in DAPYs and related analogues as HIV-1 NNRTIs." *Current medicinal chemistry*, vol. 18, no. 3, 2011, pp. 359-76. doi:10.2174/092986711794839142
18. Goebel, Frank *et al*. "Short-term antiviral activity of TMC278--a novel NNRTI--in treatment-naive HIV-1-infected subjects." *AIDS (London, England)*, vol. 20, no. 13, 2006, pp. 1721-6. doi:10.1097/01.aids.0000242818.65215.bd
19. Smith, Steven J *et al*. "Rilpivirine analogs potently inhibit drug-resistant HIV-1 mutants." *Retrovirology*, vol. 13, no. 11, 2016, doi:10.1186/s12977-016-0244-2
20. Lansdon, Eric B *et al*. "Crystal structures of HIV-1 reverse transcriptase with etravirine (TMC125) and rilpivirine (TMC278): implications for drug design." *Journal of medicinal chemistry*, vol. 53, no. 10, 2010, pp. 4295-9. doi:10.1021/jm1002233
21. Pettersen, Eric F *et al*. "UCSF Chimera--a visualization system for exploratory research and analysis." *Journal of computational chemistry*, vol. 25, no. 13, 2004, pp. 1605-12. doi:10.1002/jcc.20084
22. Anjana, Ramnath *et al*. "Aromatic-aromatic interactions in structures of proteins and protein-DNA complexes: a study based on orientation and distance." *Bioinformation*, vol. 8, no. 24, 2012, pp. 1220-4. doi:10.6026/97320630081220
23. Wensing, Annemarie M *et al*. "2019 update of the drug resistance mutations in HIV-1." *Topics in antiviral medicine*, vol. 27, no. 3, 2019, pp 111-121.
24. Hanwell, Marcus D., *et al*. *Journal of Cheminformatics*, vol. 4, no. 17, 2012, doi:10.1186/1758-2946-4-17.
25. Neese, Frank. "The ORCA Program System." *WIREs Computational Molecular Science*, vol. 2, no. 1, 2011, pp. 73–78. doi:10.1002/wcms.81.
26. Ashok, Bhavesh. "Bhaveshashok/AutoDockVina-BatchSubmission." *GitHub*, 2020, github.com/bhaveshashok/AutoDockVina-BatchSubmission.
27. Trott, Oleg, and Arthur J Olson. "AutoDock Vina: improving the speed and accuracy of docking with a new scoring function, efficient optimization, and multithreading." *Journal of computational chemistry*, vol. 31, no. 2, 2010, pp. 455-61. doi:10.1002/jcc.21334

Sponsorship

Editor's Circle $10,000+

ALLOY THERAPEUTICS

Patron $5,000+

NEW ENGLAND BioLabs® Inc.
enabling technologies in the life sciences

PORTFOLIOS WITH PURPOSE®

Institutional Supporters

HARVARD UNIVERSITY

HARVARD MEDICAL SCHOOL

Tufts UNIVERSITY

Charitable Contributions

We need your help to provide mentorship to young scientists everywhere.

JEI is supported by an entirely volunteer staff, and over 90% of our funds go towards providing educational experiences for students. Our costs include manuscript management fees, web hosting, creation of STEM education resources for teachers, and local outreach programs at our affiliate universities. We provide these services to students and teachers entirely free of any cost, and rely on generous benefactors to support our programs.

A donation of $30 will sponsor one student's scientific mentorship, peer review and publication, a six month scientific experience that in one student's words, 're-energized my curiosity towards science', and 'gave me confidence that I could take an idea I had and turn it into something that I could put out into the world'. **If you would like to donate to JEI, please visit https://emerginginvestigators.org/support, or contact us at questions@emerginginvestigators.org.** Thank you for supporting the next generation of scientists!

'Journal of Emerging Investigators, Inc. is a Section 501(c)(3) public charity organization (EIN: 45-2206379). Your donation to JEI is tax-deductible. '

emerginginvestigators.org